The Application and Limitations of PECVD for Silicon-based Photonics

Marc Spooner

A thesis submitted for the Degree of

Doctor of Philosophy

of

THE AUSTRALIAN NATIONAL UNIVERSITY

November 2005

Declaration

This thesis does not incorporate any material submitted for a degree or diploma at any university and to the best of my knowledge and belief, does not contain any material previously published or written by another person except where due reference is made in the text.

Marc Spooner

Acknowledgements

First of all, I would like to thank my supervisor, Rob Elliman for his help and guidance during the course of this project. This project would not have been completed without his encouragement.

Tessica Dall has helped considerably with experimental design as well as providing feedback on my writing. Nat Smith, Andrew Wilkinson and Taehyun Kim, the fellow Ph.D. students with whom I have worked closely with have been a source of invaluable discussion. For that I thank you.

Tim Walsh, Shannon Orbons and Wilson Pok are the honour students that I have had a pleasure to work with. Tim started the work on the SiO_2/Si_3N_4 microcavities, while Shannon has helped with the study concerning the microcavity effects in single layers of SiO_x.

I would also like to thank David Llewellyn for his help with TEM imaging and who, along with Harri Kokkonen has helped prepare the cross sectional SEM samples. I have appreciated the help provided by Damien McGrouther of the University of New South Wales regarding the images obtained with the Focused Ion Beam.

I would also like to thank Katie Pilypas, the love of my life, for her patience and understanding these last few months as well as the time she spent providing feedback on this thesis.

Abstract

This thesis presents results on the applications and limitations of plasma enhanced chemical vapour deposition for silicon-based photonics, with an emphasis on optical microcavities for the control of light emission from silicon nanocrystals.

Silicon nanocrystals were formed by precipitation and growth within Si-rich oxide layers (SiO_x) deposited by plasma enhanced chemical vapour deposition. The films were found to exhibit strong room temperature photoluminescence, with the optimum emission depending on the composition and processing of the films. The strongest emission was achieved for films with a silicon content of ~40%, following hydrogen passivation. Hydrogen was introduced into the samples by two different methods: by annealing in forming gas (95% N_2: 5% H_2) or by annealing with a hydrogenated silicon nitride capping layer. Both methods caused an increase in photoluminescence intensity due to the passivation of defects. In contrast, the presence of low levels of iron and gold were shown to reduce the concentration of luminescent nanocrystals due to the creation of non-radiative centres.

Optical microcavity structures containing silicon nanocrystals were also fabricated by Plasma enhanced chemical vapour deposition, using silicon dioxide, silicon nitride and silicon-rich oxide layers. The microcavities consisted of a silicon-rich oxide layer between two distributed Bragg reflectors formed of alternating silicon dioxide/nitride layers. The optical emission from these and related structures were examined and compared with that from individual layers in the structure. This revealed a complex interplay between defect and nanocrystal luminescence, hydrogen passivation and materials structure. The resulting

microcavity structures were shown to be suitable for producing a stop-band over the wavelength range of interest for nanocrystal emission, 500-1000nm, and to produce significant intensity enhancement and spectral narrowing. Quality factors of 50-200 were demonstrated.

The application of plasma deposited films was shown to be limited by stress-induced failure that resulted in cracking and delamination of the films during annealing. The SiO_x films thicker than about 600nm failed predominantly by cracking. This was shown to be caused by tensile stress in the film caused by hydrogen desorption during high temperature annealing. The resulting cracks showed preferred alignment depending on the crystallographic orientation of the silicon substrate. For films deposited on (100) silicon, two modes of crack propagation were observed, straight cracks aligned along <100> directions, and wavy cracks aligned along <110> directions. For films deposited on (110) silicon, straight cracks were observed along $[1\bar{1}0]$ directions, with a lesser number aligned along [001] directions. Cracks were also observed for films on (111) silicon. These showed 3-fold symmetry consistent with crack propagation along <211> directions due to plastic deformation. Details of these crack geometries and their dependencies are discussed.

Table of contents

Declaration ... **ii**

Acknowledgements ... **iii**

Abstract ... **iv**

Table of contents ... **vi**

Chapter 1 Introduction ... **1**

1.1 Motivation ... 1

1.2 Thesis organisation ... 2

1.3 Literature review ... 3

1.3.a Bandgap of bulk silicon ... 3

1.3.b Porous silicon ... 4

1.3.c Silicon nanocrystals in SiO_2 ... 5

1.3.d Passivation of nanocrystals ... 6

1.3.e Microcavities and silicon nanocrystals ... 7

1.4 Summary ... 8

Chapter 2 Theoretical Considerations ... **9**

2.1 Modelling of PL spectra ... 9

2.1.a The reflectivity of an interface ... 10

2.1.b The reflectivity of a stack of layers ... 10

2.1.c Electric field distribution ... 14

2.1.d Extraction efficiency of a microcavity ... 15

2.1.e Modelling of PL ... 17

2.2 Summary ... 18

Chapter 3 Experimental 19
3.1 Sample Preparation 19
3.1.a PECVD and RIE 19
3.1.b Annealing 20
3.2 Spectroscopy 21
3.2.a PL Spectroscopy 21
3.2.b PL Lifetime 23
3.2.c Reflectivity 24
3.2.d Index of Refraction and Thickness Measurements 25
3.3 Sample Imaging 27
3.3.a Optical Microscopy 27
3.3.b PL Imaging and PL Profiling 27
3.3.c Scanning Electron Microscopy (SEM) 29
3.3.d Focused Ion Beam 29
3.3.e Transmission Electron Microscopy 30
3.4 Ion Beam Equipment 31
3.4.a Ion Implantation 31
3.4.b Rutherford Backscattering Spectroscopy (RBS) 33
3.4.c Elastic Recoil Detection (ERD) 34
3.5 Stress measurements 34
Chapter 4 Components & their Properties 38
4.1 Thickness & index 38
4.1.a M-line 38
4.1.b Film-tek 39
4.2 Composition 41

4.2.a RBS results 41
4.2.b ERD results 42
4.3 Structural properties of nanocrystals 45
4.4 Photoluminescence 46
4.4.a Effect of sample composition 46
4.4.b Effect of anneal time 47
4.4.c Effect of anneal temperature 48
4.4.d Effect of passivation 50
4.4.e Effect of impurities 55
4.5 Summary & Conclusions 58
Chapter 5 Microcavities 60
5.1 Single layers 60
5.1.a Single layers of PECVD SiO_x 60
5.1.b Ion implanted samples 62
5.2 Silicon Dioxide / Silicon Nitride cavities 65
5.2.a PL from cavity 65
5.2.b Angular dependence of emission 68
5.2.c Effect of layer thickness 70
5.2.d Effect of number of layers 71
5.3 Effect of annealing microcavities 73
5.3.b Anomalously strong PL 76
5.4 Passivation of microcavities 78
5.4.a Hydrogenated silicon nitride passivation 78
5.5 SiO_2/SiO_x structures 80
5.6 Summary & Conclusions 83

Chapter 6 Mechanical Properties **84**

6.1 Nature of cracks 84

6.1.a SiO_x films on (100) silicon 84

6.1.b SiO_x films on (110) silicon 90

6.1.c SiO_x films on (111) silicon 91

6.2 Cause of cracks 92

6.2.a Stress 92

6.2.b The Elastic Modulus 95

6.2.c Lomer dislocations 96

6.3 Effect of cracks on the microcavities 97

6.4 Delamination 100

6.5 Methods to minimise defects 101

6.5.a Thermal treatment 101

6.5.b Patterning 101

6.5.c Layer order 103

6.6 Summary and Conclusions 104

Chapter 7 Conclusions **106**

7.1 Future work 108

References **110**

Chapter 1 Introduction

1.1 Motivation

For many decades, silicon has been the preferred material for digital microelectronics. However its optical properties leave much to be desired, particularly in relation to devices that emit light. This is largely due to the fact that it has an indirect bandgap, resulting in long radiative lifetimes and low emission efficiency. As a consequence, other, direct band-gap semiconductors, such as GaN, GaAs, InP, are used to produce optical sources. However, these materials are not compatible with current silicon manufacturing techniques and cannot be readily integrated with silicon-based digital electronics. The development of a silicon based light source would overcome such limitations[1].

The discovery of strong photoluminescence (PL)[2, 3] from nanocrystalline silicon in 1990 highlighted how the properties of nano-scale materials can differ from those of their bulk counterparts and opened the possibility of using silicon as a light source for integrated optoelectronics. This work led to a world-wide interest in porous and nanocrystalline silicon. As a result much has been learnt about the structure and properties of these materials over the past 15 years and several novel device structures have been explored[4].

Although nanocrystalline silicon is a more efficient light emitter than bulk silicon, further enhancement of the PL intensity as well as a narrower emission spectrum are desirable. Optical microcavities have been shown to be capable of achieving such performance enhancement[5].

The primary aims of this project were

- To investigate the role of material structure on the luminescence emission from Si nanocrystals
- To investigate the use and limitations of plasma-enhanced chemical vapour deposition (PECVD) for the fabrication of optical microcavities based on SiO_2 and Si_3N_4 dielectric thin films

1.2 Thesis organisation

The thesis begins with this introductory chapter which includes a brief overview of the status of research on nanocrystalline silicon and microcavities. This is then followed, in chapter 2, by an overview of the theoretical framework used to model the microcavities. The experimental details are then outlined in chapter 3 and experimental results presented in chapters 4-6.

Chapter 4 concentrates on the synthesis and properties of silicon nanocrystals. The various parameters affecting the PL of the nanocrystals are investigated to provide a baseline with which to compare the PL of the microcavity structures, which are examined in chapter 5. The limitations of PECVD for the growth of optical microcavities are also explored, with particular emphasis on stress-induced failure of thin films. The study of these processes is the subject of chapter 6. Finally, chapter 7 summarizes the conclusions of this work and outlines possible future extensions of this study.

1.3 Literature review

1.3.a Bandgap of bulk silicon

The bandgap of silicon is approximately 1.1eV and is indirect (see Figure 1.1). Electrons at the minimum of the conduction band do not have the same momentum as holes at the maximum of the valence band. The electrons and holes cannot recombine without absorbing or creating a phonon to conserve momentum. This slows down the radiative recombination of the electron and holes and leads to inefficient light emission due to competing non-radiative recombination, which is generally much faster than radiative recombination[6].

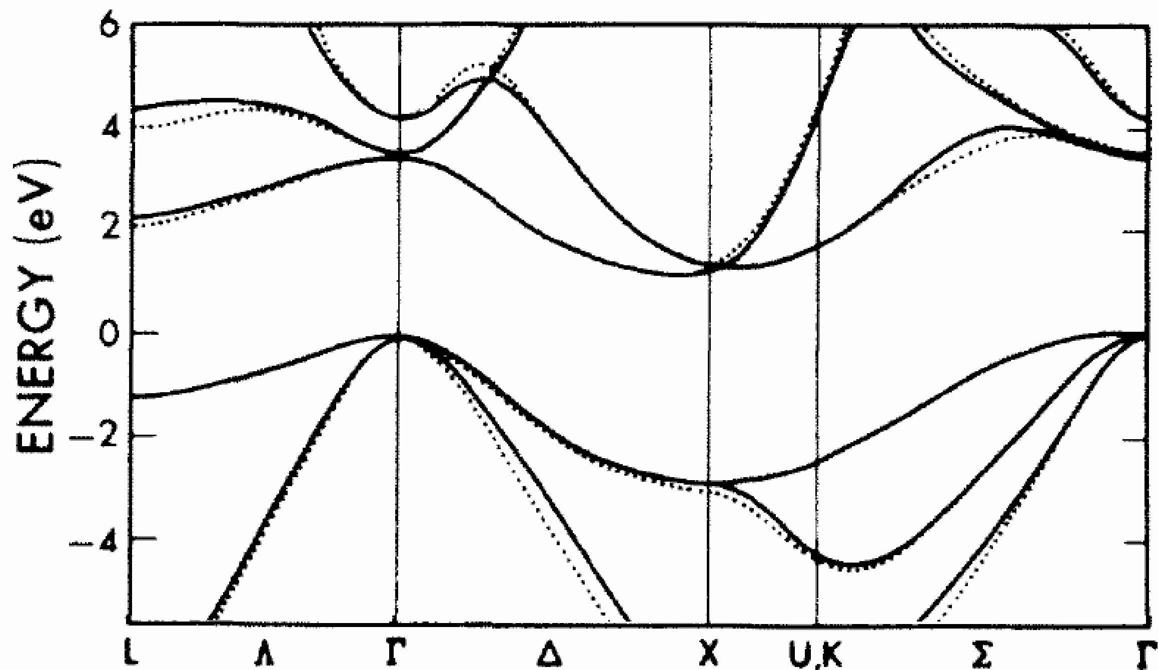

Figure 1.1 The calculated bangap of silicon[7] showing an indirect bandgap of 1.1 eV between the points the bottom of the conduction band (near X) and the top of the valence band (at Γ) .

1.3.b Porous silicon

The first measurement of strong PL from silicon was made in 1990 by Canham[3]. He measured strong PL from porous silicon made by electro-chemical etching of silicon. The electrons and holes in porous silicon are confined to the small crystalline silicon regions between the pores, leading to quantum effects. This confinement of the electron's wave function in real space causes its wave function to expand in momentum space, relaxing the conservation of momentum selection rules and increasing the probability for electron-hole recombination. The confinement also increases the energy gap for carriers. Therefore the emission from nanostructured silicon is more efficient and at higher energies (or shorter wavelengths) than from bulk silicon.

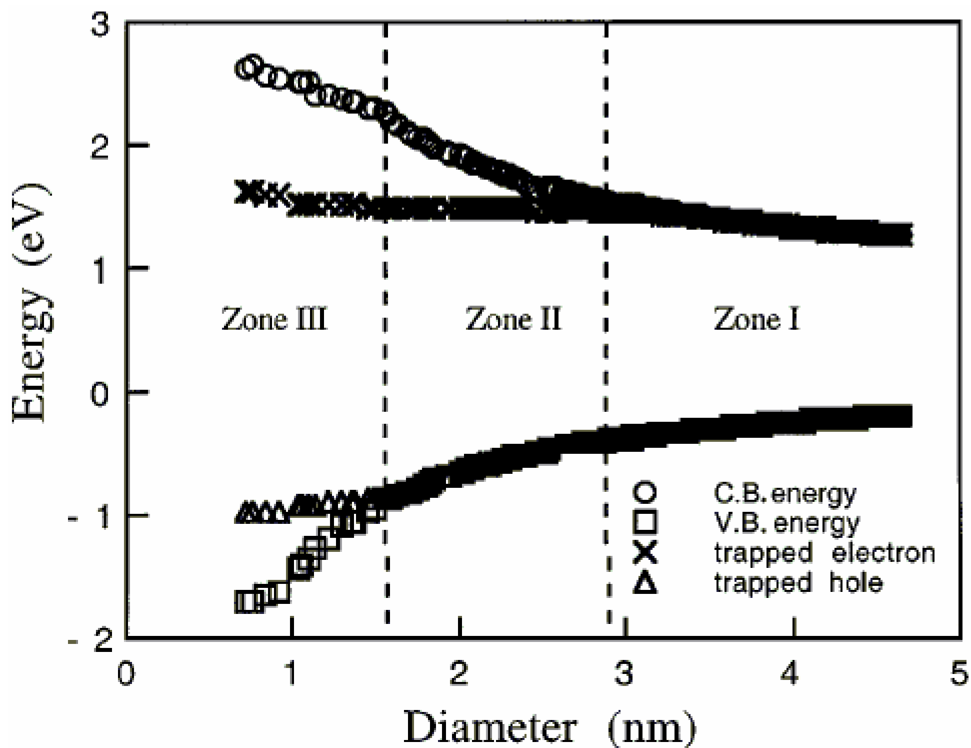

Figure 1.2 The band structure of silicon nanocrystals as a function of nanocrystal size[8]

Wolkin et al.[8] calculated the bandgap of silicon nanocrystals as a function of their size and the resulting bandgap is shown in Figure 1.2. For nanocrystals smaller than 3nm, the widening of the bandgap is limited by localised states associated with Si=O.

Ledoux et al.[9] have proposed the following relation between the peak photon energy (E in eV) and the nanocrystal diameter (d in nm) which gives good agreement with experimental data for nanocrystals with diameters greater than 3nm.

$$E = 0.925 + \frac{3.73}{d^{1.39}} + \frac{0.881}{d} \qquad \textbf{Equation 1.1}$$

The spatial confinement of electrons and holes also increases the PL efficiency of nanocrystalline silicon. Electrons and holes have a long radiative lifetime in bulk silicon and can diffuse large distances and have a high probability of encountering a defect acting as a non-radiative recombination centre. In nanocrystalline silicon, this diffusion is limited by the crystal boundary, increasing the PL efficiency by reducing the probability of electron encountering a defect.

1.3.c Silicon nanocrystals in SiO_2

The high surface area in porous silicon makes it fragile and chemically unstable in air[10]. In 1990, Takagi et al.[2] were the first to measure the PL from silicon nanocrystals in SiO_2. Later in 1993, Shimizu-Iwayama et al.[11] showed that nanocrystalline silicon can be produced in SiO_2 by implantation of silicon ions followed by high temperature annealing. The excess silicon precipitates during high temperature annealing, with the size of the nanocrystals depending on the excess silicon concentration[12, 13]. Optimal PL emission is observed for samples with an excess silicon content of approximately 15% [14-16].

Another method of producing nanocrystals is to deposit silicon-rich layers using PECVD followed by high temperature annealing[17-19]. Although the production of a nanocrystal layer using PECVD is both quicker and easier than using ion implantation, the films generally contain higher concentrations of impurities such as hydrogen and nitrogen [20, 21]. The PL spectra of these films are similar to those produced by ion implantation and show a similar dependence on anneal temperature and excess silicon content[17].

The nanocrystals produced from silicon-rich oxides nucleate and grow through Ostwald ripening[14]. This produces a range of nanocrystal sizes and thus the nanocrystals have a range of bandgaps. The PL spectra of films prepared in this way are broad (FWHM ≈ 200 nm) similar to the spectra from porous silicon. Narrowing the spectral width of the emission is highly desirable and forms part of the motivation for the present study.

1.3.d Passivation of nanocrystals

Charge trapping defects such as dangling bonds at the Si/SiO_2 interface can severely limit the PL efficiency of silicon nanocrystals. Indeed, Lanoo[6] has shown that the PL from a nanocrystal can be effectively quenched by a single dangling bond. Importantly, it has been shown that these defects can be pacified by hydrogen[22, 23]. The most widely used method of introducing the hydrogen is annealing in forming gas which provides enhancements in PL intensity from two to ten times[24-27]. Wilkinson et al.[28] have studied the kinetics of hydrogen passivation of Pb defects for silicon nanocrystals in SiO_2 determining that ~500°C is the optimal temperature for the passivation anneal.

Another passivation techniques used primarily in the solar cell industry is a SiO_2/Si_3N_4 anneal. A SiO_2 layer is grown on the silicon surface followed by a PECVD nitride layer.

The nitride layer contains a significant concentration of hydrogen. Upon annealing, the hydrogen in the nitride layer is released and diffuses through the oxide layer to passivate the Si/SiO_2 interface. Several studies have reported improved passivation compared to a deposition of SiO_2 followed by a forming gas anneal[29, 30].

1.3.e Microcavities and silicon nanocrystals

Planar microcavities have been used to enhance the emission of various light sources including nanocrystalline silicon. The simplest form for an optical microcavity consists of two partially reflecting mirrors placed parallel to each other. When a light source is placed within a microcavity, the light emitted undergoes multiple reflections before emerging from the cavity. The emitted light is the result of interference between these different reflections. Only wavelengths near the cavity resonance are enhanced by constructive interference. In this way, microcavities can take a broad spectrum light source and produce more intense emission with a narrow spectral distribution. This stronger emission in the forward direction comes at the expense of emission at other angles and guided modes[31].

Microcavities can be made from porous silicon[32-34]. During the formation of porous silicon, the porosity which determines the index of refraction varies with the applied current. Etching only occurs at the bottom of the pores therefore varying the current during the course of the etching produces a layered variation in porosity (and index of refraction). This method is capable of producing microcavities with quality factors in excess of 3000 due to the large number of layers that can be produced (over 100)[35]. Such microcavities were successfully used to enhance the PL of porous silicon. Porous silicon microcavities suffer from high chemical sensitivity. However this sensitivity has been exploited for use as a chemical sensor[36].

Another method of fabricating microcavities is to deposit them by PECVD. Many of the PECVD deposited microcavities involve silicon nitrides where the silicon content of the layers is varied to modulate the index of refraction[37-40]. However, few studies have dealt specifically with the possibility of using SiO_2/Si_3N_4 Bragg mirrors to enhance the PL from silicon nanocrystals. Bayindir et al.[41] have used SiO_2/Si_3N_4 distributed Bragg mirrors to create a microcavity and enhance the emission from silicon-rich nitride layers. They have also fabricated and measured the transmission of coupled microcavities based on SiO_2 and Si_3N_4[42] indicating that these structures should be able to effectively enhance the PL from silicon nanocrystals. To date, there has been no detailed study of the advantages and limitation of using PECVD SiO_2/Si_3N_4 distributed Bragg reflectors to define microcavities to enhance the emission from silicon nanocrystals embedded in SiO_2.

1.4 Summary

- Nanocrystalline silicon emits light more efficiently than bulk silicon due to spatial and quantum confinement effects.
- The bandgap of silicon nanocrystals increases with decreasing nanocrystal size leading to a blue-shift in the optical emission.
- Nanocrystals can be formed in SiO_2 by annealing of silicon-rich silicon oxides but this produces nanocrystals with a broad size distribution.
- The optical emission from an ensemble of nanocrystals has a broad spectral range (~200nm) due to inhomogeneous broadening.
- Microcavities can be used to enhance the emission at selected wavelengths.
- The purpose of this work is to determine the advantages and limitations of PECVD deposited microcavities for controlling the PL from silicon nanocrystals.

Chapter 2 Theoretical Considerations

2.1 Modelling of PL spectra

A microcavity structure can significantly modify the emission from silicon nanocrystals. The PL intensity from a particular point in a microcavity structure is proportional to the number of electron-hole pairs produced in the nanocrystals at that position, the spectral distribution of the nanocrystal emission $PL_{nc}(\lambda)$ and the extraction efficiency $\eta(\lambda,z)$. The extraction efficiency is the fraction of light originating in the layer that is emitted by the top surface of the cavity, which depends on the wavelength of the light and its originating position in the cavity. The number of electron-hole pairs in the nanocrystals depends on the amount of energy absorbed by the nanocrystal which is proportional to the square of the amplitude of the electric field produced by the excitation laser. This will also vary with position in the cavity. Integrating over all positions in the cavity will give the measured PL spectrum.

$$PL_{measured}(\lambda) = \int_0^t PL_{nc}(\lambda)\, \eta(\lambda,z)\, \left|E(z)\right|^2 dz \qquad \textbf{Equation 2.1}$$

As will be shown in chapter 5, the reflection at the film/air and the film/substrate interfaces can be sufficient to produce a microcavity structure. Therefore while Equation 2.1 was developed for microcavities it also applies for thin films in general. In order to calculate the extraction efficiency and the electric field, it is necessary to know the reflectivity of the two mirrors. The next two subsections deal with calculating the reflectivity of mirrors forming the microcavities, where these consist of either simple interfaces or distributed Bragg

reflectors. Once the reflectivity of the mirrors is known, properties such as the electric field distribution, transmission of the microcavity structure as well as its extraction efficiency can be calculated[43].

2.1.a The reflectivity of an interface

In the case of a simple interface, the reflectivity depends on the index of refraction of the materials as well as the direction of propagation and polarisation of the light. The TE and TM polarisations need to be considered separately. The reflection coefficient of an interface can be calculated from[43]:

$$r_{\perp} = \frac{n_i \cos(\theta_i) - n_t \sqrt{1 - \frac{n_i}{n_t} \sin^2(\theta_i)}}{n_i \cos(\theta_i) + n_t \sqrt{1 - \frac{n_i}{n_t} \sin^2(\theta_i)}} \qquad \textbf{Equation 2.2}$$

$$r_{\parallel} = \frac{n_t \cos(\theta_i) - n_i \sqrt{1 - \frac{n_i}{n_t} \sin^2(\theta_i)}}{n_t \cos(\theta_i) + n_i \sqrt{1 - \frac{n_i}{n_t} \sin^2(\theta_i)}} \qquad \textbf{Equation 2.3}$$

2.1.b The reflectivity of a stack of layers

i) Distributed Bragg Reflectors

Distributed Bragg reflectors (DBR) can provide a much higher reflectivity at selected wavelengths than a simple interface thereby improving the quality of the cavity. Distributed Bragg reflectors consist of a series of layers with a high and low index of refraction. To produce a reflectivity peak at a particular wavelength, the optical thickness of each layer should be a quarter of this wavelength. The reflectivity of a multilayer film can be calculated using the matrix method[43, 44]. The reflection coefficient (r) is calculated from

matrix (M) using Equations 2.4-2.7. The matrix for a multi-layer structure is the product of the matrices for the individual layers.

$$r = \frac{n_0 (M_{11} + M_{12} n_s) - (M_{21} + M_{22} n_s)}{n_0 (M_{11} + M_{12} n_s) + (M_{21} + M_{22} n_s)} \qquad \textbf{Equation 2.4}$$

where

$$M_a = \begin{pmatrix} M_{11} & M_{12} \\ M_{21} & M_{22} \end{pmatrix} = \prod_{x=1}^{a} \begin{pmatrix} \cos(\phi_x) & \frac{i}{Y_x} \sin(\phi_x) \\ i\, Y_x \sin(\phi_x) & \cos(\phi_x) \end{pmatrix} \qquad \textbf{Equation 2.5}$$

$$\phi_a = \frac{2\pi n_a t_a \cos\theta_a}{\lambda} \qquad \textbf{Equation 2.6}$$

$$Y_a = \begin{cases} n_a \cos\theta_a & \text{for TE polarisation} \\ \dfrac{n_a}{\cos\theta_a} & \text{for TM polarisation} \end{cases} \qquad \textbf{Equation 2.7}$$

with n_a and t_a being the index of refraction and thickness of the individual layers, n_o and n_s being the index of refraction of the air and substrate and $i = \sqrt{-1}$. Snell's law can be used to determine θ_a, the direction of propagation in each layer.

An example of the result of this modelling can be seen in Figure 2.1. The reflectivity as a function of wavelength for distributed Bragg reflectors with various numbers of layers was calculated. In this example, the structure consisted of alternating layers of materials with indices of refraction of 2.0 and 1.45 on a substrate with an index of 3.45 to model a stack of Si_3N_4/SiO_2 layers on a silicon substrate. An optical thickness of 200nm was used for each layer to produce a peak in the reflectivity spectrum at 800 nm.

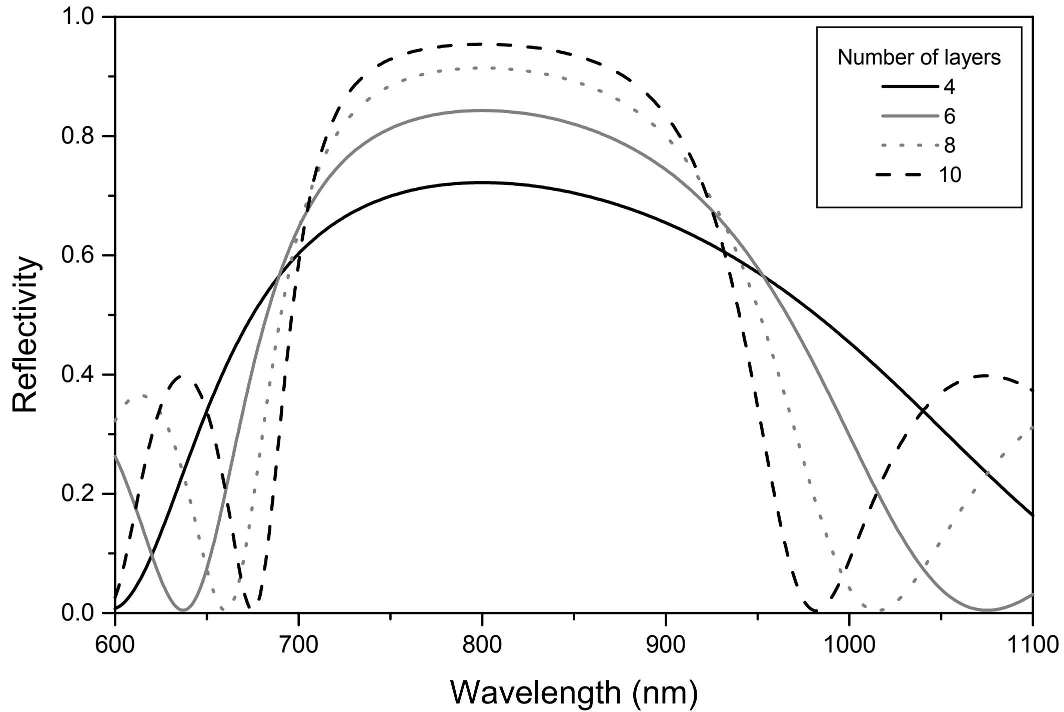

Figure 2.1 The reflectivity of a distributed Bragg mirror as a function of wavelength and number of layers.

To make an adequate microcavity, the stop-band (or wavelength range of the high reflectivity peak) must cover the spectral distribution of the nanocrystal emission (650-950nm). The reflectivity of the peak depends on the number of layers as well as the indices of refraction of the layers. In general, the reflectivity is higher for a greater number of layers. For a stack of layers with indices of refraction of refraction n_1 and n_2 and optical thickness of $\lambda/2$, the peak reflectivity occurs at λ, as given by Equation 2.8, while the width of the reflectivity peak is determined by the contrast in index of refraction as given by Equation 2.9.

$$\lambda = 2(n_1 t_1 + n_2 t_2) \qquad \textbf{Equation 2.8}$$

$$\Delta\lambda = \frac{4\,\lambda_o}{\pi} \arcsin\left(\frac{n_2 - n_1}{n_2 + n_1}\right) \approx \frac{4\,\lambda_o}{\pi}\left(\frac{n_2 - n_1}{n_2 + n_1}\right) \qquad \textbf{Equation 2.9}$$

These simulations shows that a DBR made from SiO_2 and Si_3N_4 can produce a stop-band over the nanocrystal emission spectrum.

ii) Microcavities

For the present study, a suitable microcavity will consist of a λ/2 SiO_x layer with an index of refraction of 1.7. This layer is bound on each side by a SiO_2/nitride DBR. The bottom mirror consists of an 8 layer DBR while the top mirror consists of 5 layers. The reflectivity of this structure can be calculated in the same way as the DBRs and the results are shown in Figure 2.2.

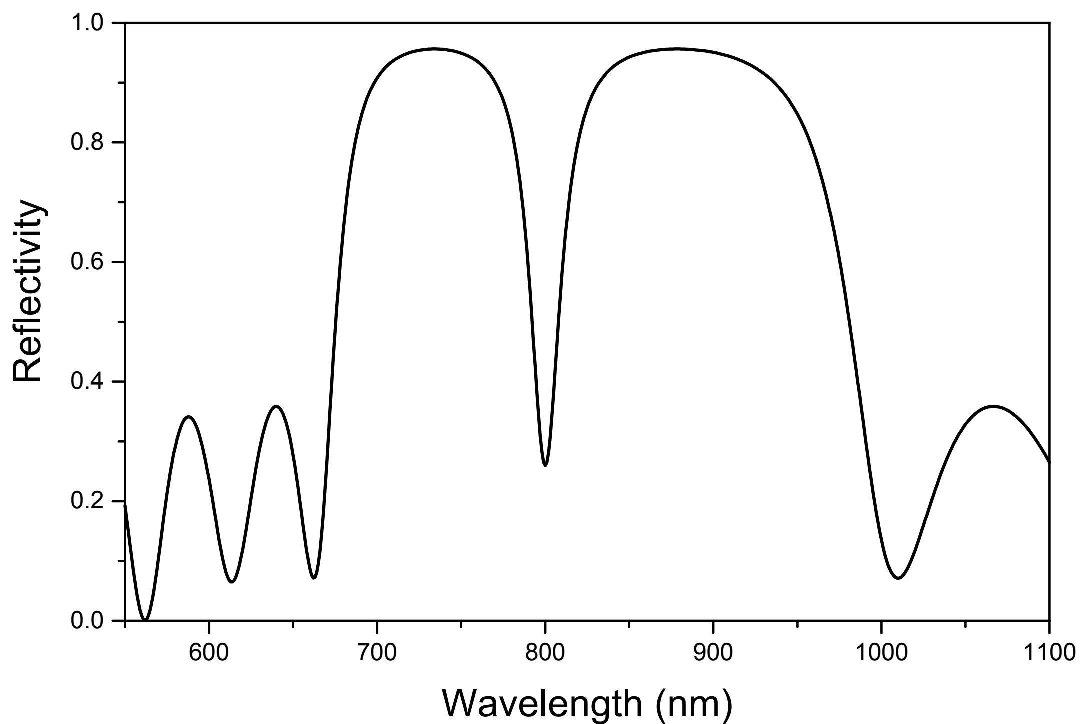

Figure 2.2 Modelled reflectivity spectrum of a microcavity structure with SiO_2/Si_3N_4 DBRs and a SiO_x active layer with an optical thickness of 400nm.

The reflectivity of the microcavity structure resembles that of the DBR except for the dip in the centre of the stop-band. This dip corresponds to the resonant wavelength of the microcavity. Two parameters often used to describe and compare optical cavities are the finesse and quality factor. When the transmittance of a cavity is plotted against frequency,

the finesse ($\mathcal{F}$) is defined as the ratio of the peak width (δν) to the peak spacing (Δν) between subsequent peaks while the quality factor (Q) for a particular peak is the ratio of the peak width (δν) to the wavenumber (ν=1/λ).

$$\mathcal{F} = \frac{\Delta\nu}{\delta\nu} \qquad \textbf{Equation 2.10}$$

$$Q = \frac{\nu}{\delta\nu} \approx \frac{\lambda}{\delta\lambda} \qquad \textbf{Equation 2.11}$$

Both the finesse and the quality factor increase as the peak in the transmittance spectrum becomes sharper. As we shall see in the following section, the PL emitted from a microcavity is related to the transmittance of the cavity therefore cavities with a high finesse or Q-factor should produce a sharp PL spectrum.

2.1.c Electric field distribution

The electric field distribution is of interest because in the case of PL, the amount of energy absorbed by the nanocrystals is proportional to the square of the local electric field amplitude. The electric field can also be calculated using the matrix method[44]. The electric and magnetic fields at the air/first layer interface are given by Equation 2.12 while in general, those at the interface between the (n-1)th layer and nth layers are given by Equation 2.13. A layer can be subdivided to get the field values at any arbitrary positions.

$$\begin{pmatrix} E_1 \\ H_1 \end{pmatrix} = \begin{pmatrix} 1 + r \\ (1-r)Y_0 \end{pmatrix} \qquad \textbf{Equation 2.12}$$

$$\begin{pmatrix} E_n \\ H_n \end{pmatrix} = M_{n-1}^{-1} \begin{pmatrix} E_{n-1} \\ H_{n-1} \end{pmatrix} \qquad \textbf{Equation 2.13}$$

with M_n and Y_0 given by equations 2.5 and 2.7 respectively.

The electric field distribution was calculated for a SiO_x cavity with an optical thickness of 400nm, with a 5 layer SiO_2/Si_3N_4 DBR for the top mirror and an 8 layer bottom mirror. Each layer in the DBRs had an optical thickness of 200nm. The bottom panel of Figure 2.3 shows the resulting electric field distribution from a 532nm laser for a typical microcavity used in this study. The simulated microcavity has the refractive index profile given in the top panel of Figure 2.3.

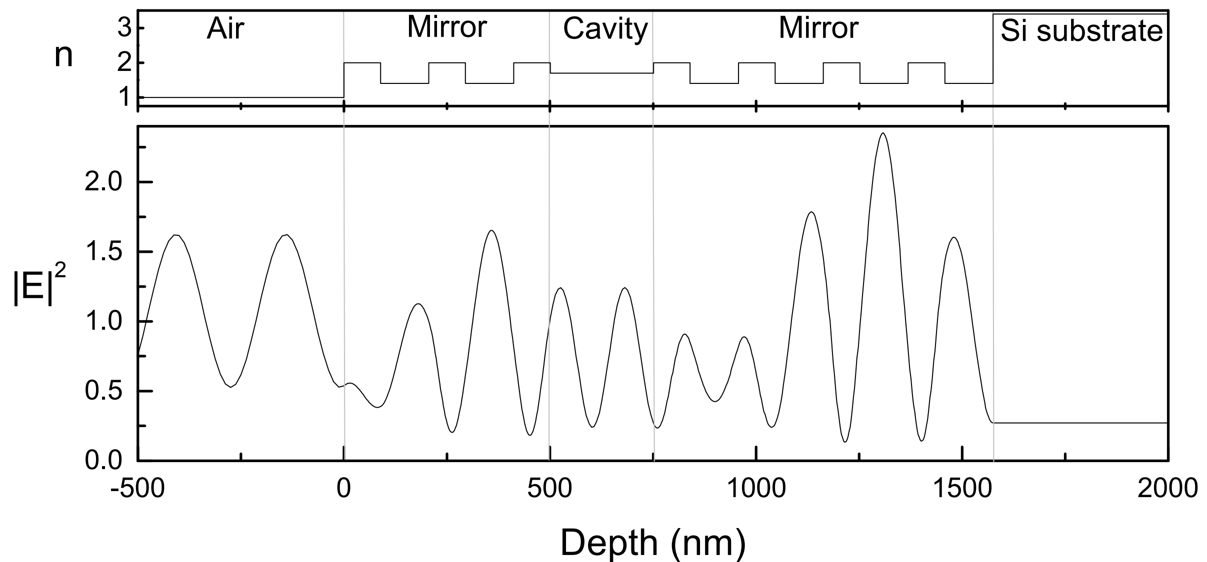

Figure 2.3 The profile of the index of refraction of a microcavity and the profile of the electric field squared resulting from an external 532nm laser incident on this cavity.

2.1.d Extraction efficiency of a microcavity

The extraction efficiency is the ratio between the intensity of the light emerging from the top surface of the sample to the intensity of light emitted by the sample. For a sample in a microcavity, the extraction efficiency will depend on the reflection coefficients of the top and bottom mirrors (r_1 and r_2) and the thickness of the cavity (L) [31].

For an internal source, the light emitted is the result of the interference between the two infinite series of reflections as indicated in see Figure 2.4 (b) resulting in Equation 2.14

$$\eta(\lambda,z)= \frac{T_1\,|1 + r_2 \exp[8\pi i\, nz \cos\theta/ \lambda]|^2}{|1 - r_1 r_2 \exp[4\pi i\, nL \cos\theta/ \lambda]|^2}$$ **Equation 2.14**

Where r_1 and r_2 are the reflection coefficients of the top and bottom mirrors, T_1 is the transmission of the top mirror, z is the distance between the emitter and the bottom mirror

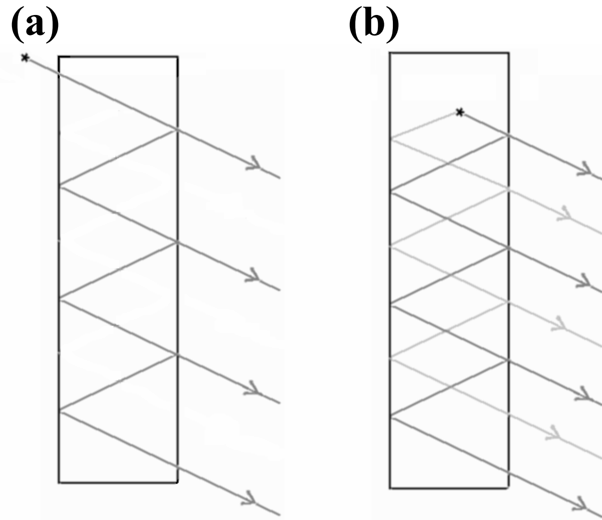

Figure 2.4 Ray diagram of (a) the transmission of light through a microcavity and (b) the extraction of light from the microcavity.

and θ is the angle of propagation of the light within the layer.

For a Fabry-Perot microcavity with distributed Bragg reflectors, the phase change occurring at distributed mirrors is taken into account by the imaginary parts of the reflection coefficients r_1 and r_2 which are, in general, complex numbers.

The enhancement in PL is mainly due to an increase in the extraction efficiency. However, the enhancement depends on the direction θ. If a cavity is designed to enhance a particular wavelength in the forward direction, the emission at that wavelength will be suppressed at larger angles including guided modes.

Similarly, the transmission of the cavity is calculated by summing the contributions of all the possible paths the light can take to emerge from the sample[43] (see Figure 2.4(a)). Although this is an infinite sum, the sum converges to:

$$T = \frac{T_1 T_2}{|1 - r_1 r_2 \exp(4\pi i\, nL \cos\theta / \lambda)|^2} \qquad \textbf{Equation 2.15}$$

where T_1 and T_2 are the transmittance of the two mirrors, n and L are the index of refraction and thickness of the cavity, and θ is the angle of propagation inside the cavity.

The expression for the extraction factor (Equation 2.14) is very similar to the expression for the transmission of the cavity (Equation 2.15). They differ in that the transmittance of the second mirror has been replaced by the term $|1 + r_2 \exp(8\pi i n z \cos(\theta)/ \lambda)|^2$. Both terms are approximately equal to one near the cavity's resonant wavelength. Therefore transmission spectra can be used to predict the positions of the maxima of the PL spectrum. In practice it is easier to measure the reflectivity of the microcavity because they are generally on silicon substrates. Therefore the peak emission wavelength of the PL spectra should correspond to the wavelength of the dip in the reflectivity spectrum.

2.1.e Modelling of PL

In order to model the PL spectrum of a microcavity, we need to combine the concepts in sections 2.1.b to 2.1.d and assume the emission spectrum of the active layer. The emission spectrum was determined by measuring that of a 250nm SiO_x layer and correcting for the extraction efficiency of the layer. Figure 2.5 shows the result of this modelling on the microcavity defined in section 2.1.b. The PL spectrum from a 250nm SiO_x layer, representing the nanocrystal emission spectrum, is included for reference. This simulation shows that the expected enhancement in PL is of the order of 50 times.

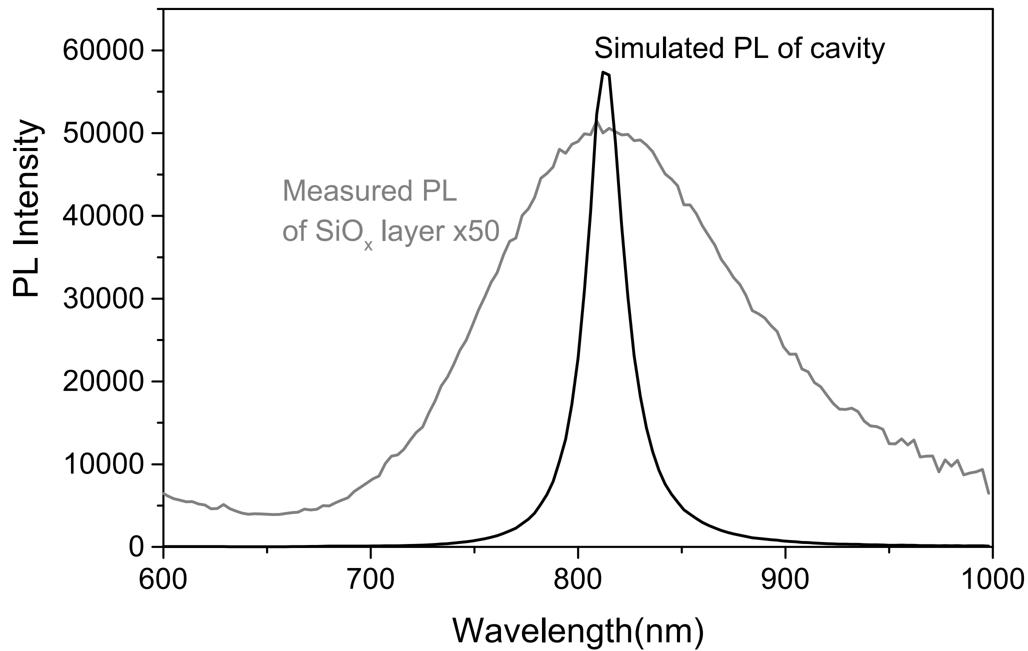

Figure 2.5 Simulation of PL spectrum from a microcavity structure.

2.2 Summary

- A model was presented for the calculation of emission spectra from an optical microcavity containing silicon nanocrystals.
- Distributed Bragg reflectors based on SiO_2/Si_3N_4 multilayers were shown to have a predicted stop-band that covers the spectral emission from silicon nanocrystals.
- The microcavity's peak emission wavelength, corresponding to the cavity's resonant wavelength, was shown to correspond to a minimum sample reflectivity.
- The expected enhancement in PL emission intensity from the microcavity was estimated to be of the order of 50 times that of a single SiO_x layer.

Chapter 3 Experimental

3.1 Sample Preparation

3.1.a PECVD and RIE

A Plasmalab 80Plus system was used to deposit and etch silicon oxide and nitride layers used in this research project. During Plasma Enhanced Chemical Vapour Deposition (PECVD), a mixture of ammonia (NH_3), dilute silane (95% N_2 +5% SiH_4) and nitrous oxide (N_2O) is introduced into the process chamber. A 13.56MHz RF generator ionises the gases in the chamber to form a plasma. The ions in the plasma deposit onto the sample and react with the surface. The composition of the deposited film depends on the composition of the gases forming the plasma as well as the substrate temperature, gas flow rates and plasma power.

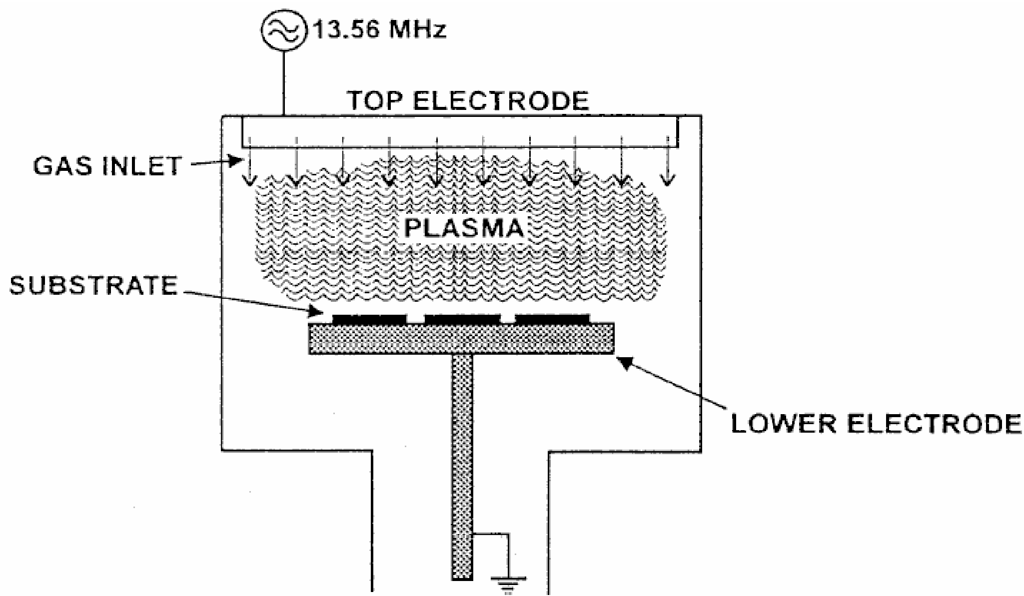

Figure 3.1 Schematic of the PECVD chamber[45].

The recipes used to make silicon-rich oxides were based on the work of Deenapanray[46]. The RF power, pressure and temperature in the reactor during deposition were 20W, 1 Torr and 300°C, respectively, for all films. The flow rates of the various gases are listed in Table 3.1.

Material	**Nominal Si %**	**N_2O flow rate** (sccm)	**SiH_4 flow rate** (sccm)	**NH_3 flow rate** (sccm)
SiO_2	33	700	160	0
SiO_x 36%	37	75	160	0
SiO_x 40%	39	50	160	0
SiO_x 47%	41	35	160	0
SiO_x 52%	43	25	160	0
Si_3N_4	43	0	1000	50

Table 3.1 Flow rates used to produce the various materials in the microcavities.

A separate chamber was used for reactive ion etching (RIE), the removal of material by plasma etching. In this case the substrate temperature was maintained at room temperature and the reactant gases were a combination of oxygen, argon and carbon tetrafloride (CF_4).

3.1.b Annealing

To produce silicon nanocrystals from the silicon-rich oxides, the samples must be annealed at ~1100°C for around one hour. The two types of furnaces illustrated in Figure 3.2 were used in the present work. For anneals of 30min to 16h, a conventional quartz tube furnace was used. The samples were placed in the tube which can be heated to a maximum of 1200°C. Typically the samples were pushed slowly into a pre-heated furnace in a quartz boat using a quartz rod. It is also possible increase the temperature while the sample is in the furnace.

For short anneals (less than 10 minutes), a rapid thermal annealer (RTA) was used. The RTA uses halogen lamps to heat the sample very quickly, taking about five seconds to go from room temperature to 1000°C. For both types of furnace, the annealing ambient was either nitrogen or forming gas (95% N_2 + 5% H_2).

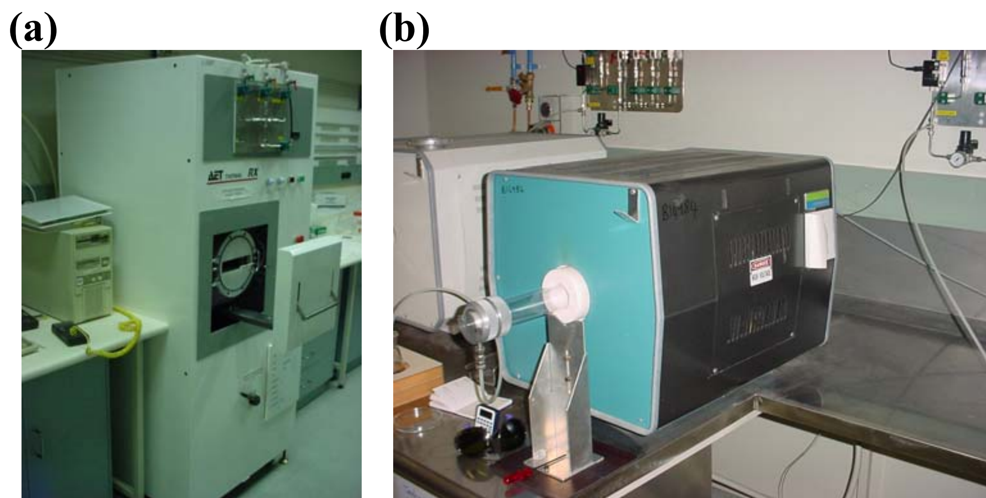

Figure 3.2 (a) The rapid thermal processor and (b) the tube furnace used to anneal the various samples.

3.2 Spectroscopy

3.2.a PL Spectroscopy

The setup used for the PL measurements is shown in Figure 3.3. To excite the nanocrystals, a Rumzing diode pumped solid-state (DPSS) laser with a wavelength of 532nm was used. The light was collected by a pair of fused silica plano-convex lenses, each with focal lengths of 20cm. One was placed 20cm away from the sample while the other was placed 20cm from the entrance slit of the spectrometer so an image of the sample was projected onto the entrance slits.

The spectrometer consisted of a Triax 320 spectrometer with a turret containing three holographic grating to disperse the light coming from the sample. The grating used for the measurements presented herein had 150 groves/mm and a blaze of 500nm. This grating allowed the spectral region of interest, 500-1000nm, to be measured with a single acquisition. Other gratings were used when high resolution scans were required.

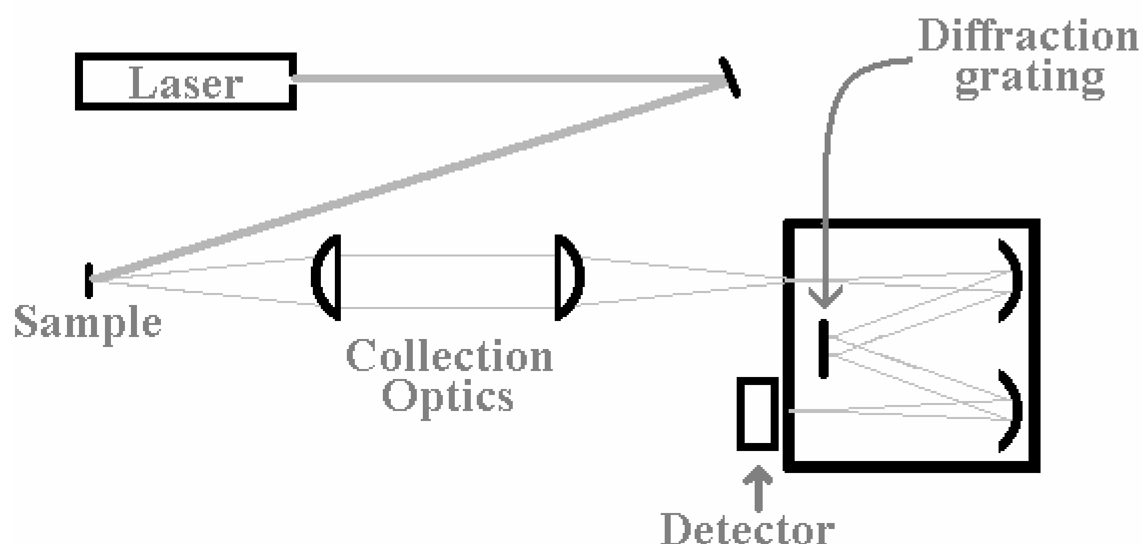

Figure 3.3 PL measurement setup.

A Spectrum One CCD array was used to measure the sample's PL intensity. The 256x1024 array of silicon photodiodes is capable of detecting light with a wavelength between 400nm and 1050nm. For typical measurements, the wavelength resolution of the detection system was 0.5nm/pixel. The correction for the system's response was determined by measuring the emission of a black body source and adjusting the measured spectrum to match that calculated for the black body. The PL intensity was measured in arbitrary units. However each PL spectrum presented was normalised to give the same values for a reference sample.

For certain samples, the PL was also investigated as a function of angle. In this case, the sample was placed on a rotating sample holder that was carefully placed so the axis of rotation coincided with the field of view of the spectrometer. The excitation laser light was brought to the sample using an optical fibre and focused onto the sample using a lens. As shown in Figure 3.4, the end of the optical fibre as well as the lens rotated with the sample to ensure that the illumination conditions did not vary as the sample was rotated. The angle (θ) was measured from the sample normal.

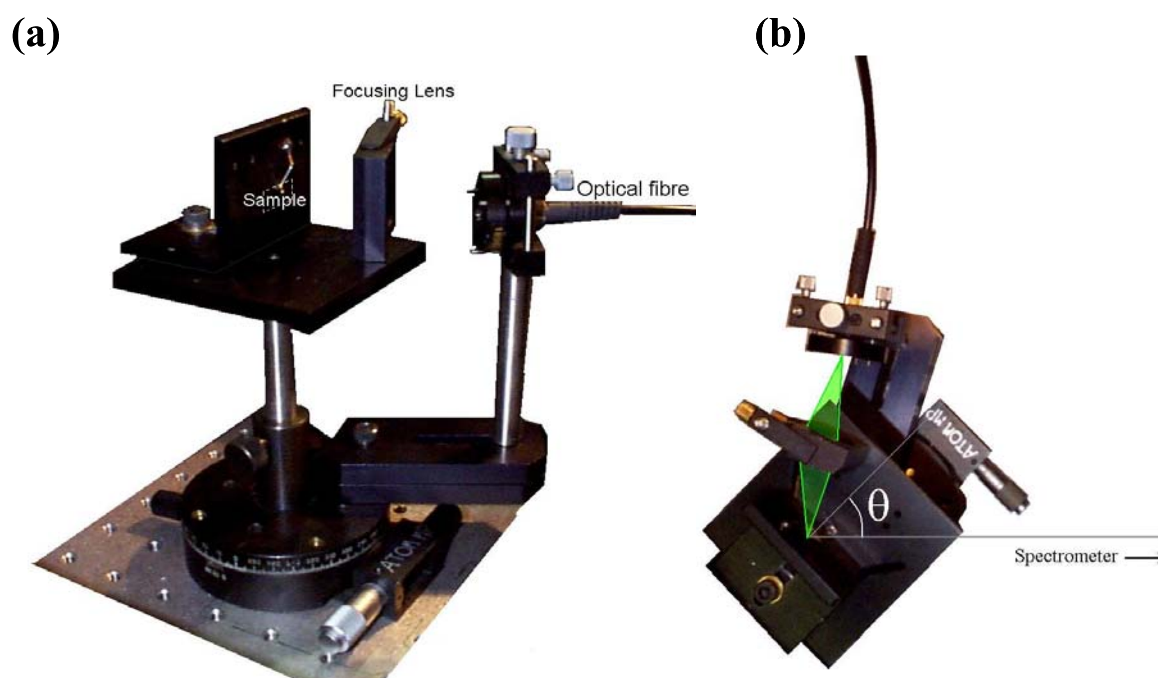

Figure 3.4 Photos of the rotating sample holder used for measurement of PL as a function of angle.

3.2.b PL Lifetime

For PL lifetime measurements, a photomultiplier tube and a digital storage oscilloscope were used. The excitation laser was modulated with an acousto-optic modulator. The signal from the photomultiplier tube was captured by a digital storage oscilloscope and averaged over 128 periods or more to improve the signal to noise ratio. The decay of the

photoluminescent intensity was modelled using a stretched exponential function to determine the average lifetime (τ) and the dispersion factor (β) [47].

$$I(t) = I_o \exp\left[-\left(\frac{t}{\tau}\right)^{\beta}\right]$$ **Equation 3.1**

The accuracy of the measurement was limited by the detector response time which was about 0.5μs but varied depending on the detector sensitivity.

3.2.c Reflectivity

The reflectivity of the sample was measured in order to determine the thickness and index of refraction as well as determine the resonant wavelength of the microcavities. Two different spectrometers were used to measure the reflectivity, a Shimadzu spectrophotometer, and a Carie-5000.

i) Shimadzu system

A Shimadzu UV-3101PC photometer with a specular reflectance attachment was used for most of the measurements because of its ability to measure the reflectivity of small samples. The spectrophotometer's spectral range is from 190nm to 3200nm with a resolution of 0.1nm. There are two light sources: a 50W halogen lamp and a deuterium lamp, and two detectors: a PbS photocell for the near-infrared region and an R-928 photomultiplier for ultra-violet and visible measurements. The reflectivity measurements are taken at an angle of 5° from the sample normal. This system measures the reflectivity relative to an aluminium reference mirror. The results reported in this thesis have been corrected by multiplying by the reflectivity of the aluminium mirror which was measured independently.

ii) Cary 5000 system

The Cary 5000 spectrometer also uses a R928 photomultiplier tube to detect visible and UV light as well as a cooled PbS photocell for near infra-red measurements. With the specular reflection attachment this system is capable of measuring the absolute reflectivity of large samples. It requires the light to reflect off the sample at two different positions. To do so the sample must be about 2cm in length. The system is capable of measuring the reflectivity of a sample relative to a reference at angles between 20° and 70° in increments of 0.5°.

3.2.d Index of Refraction and Thickness Measurements

Accurate measurements of the index of refraction and thicknesses of the films were required to adequately model the reflectivity and PL of the various structures investigated.

i) M-line Spectrometer

A Metricon 2010 prism coupler was used to determine the refractive index and thickness of optical thin films by measuring the coupling angles for wave guiding at wavelengths of 633 and 810nm. The technique works by monitoring the intensity of laser light undergoing total internal reflections at the prism/air interface as the incident beam angle is scanned (see Figure 3.5). For certain angles, light couples into the film, reducing the reflectivity. These angles are given by the following equation:

$$\frac{2\pi n t \cos\theta_2}{\lambda} + \psi_1 + \psi_2 = m\pi \quad \text{with } m = 0, 1, 2...$$ **Equation 3.2**

where n and t are the refraction index and thickness of the film, and ψ_1 and ψ_2 are the phase changes occurring at the film-air and film substrate interfaces. Solutions to this equation can be determined if two or more reflectivity minima are found[48].

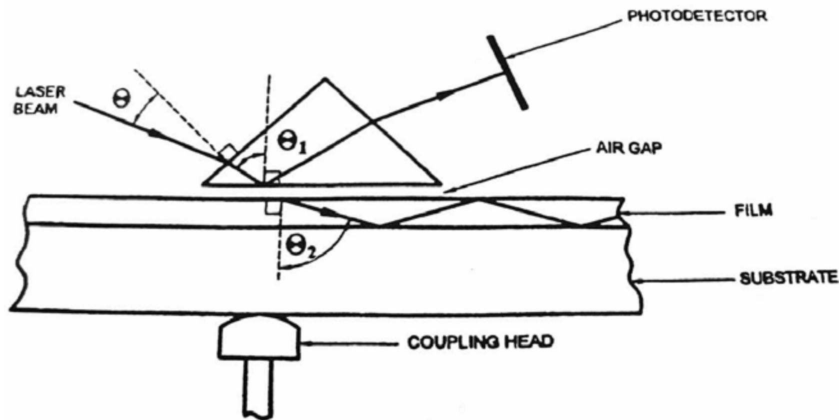

Figure 3.5 Experimental setup of prism coupler system for refraction index and thickness measurement[49].

This method requires that the index of refraction of the prism to be greater than that of the sample. Because of this limitation, it was not possible to measure films with an index of refraction greater than two. Similarly, if the film is too thin to support more than one optical mode a unique solution of equation 2.2 is not possible. For the silicon-rich oxides, the minimum thickness necessary for a unique measurement was about 600nm.

ii) Filmtek system

The SCI Filmtek 4000 was also used to determine the thickness and index of refraction of the selected films. Reflectance spectra were taken at 0 and 70°. The system uses a silicon photodiode array for measurements for wavelengths of 350 to 1000nm with a resolution of 0.2nm and an InGaAs photodiode array for measurements from 900 to 1700nm with a resolution of 2nm. This reflectivity data is used to solve for the thickness and optical constants of the film.

3.3 Sample Imaging

3.3.a Optical Microscopy

Most of the optical microscopy images in this thesis were obtained using a LM/MAC-Zeiss Axioskop microscope with a SPOT CCD camera.

3.3.b PL Imaging and PL Profiling

PL imaging and PL profiling were used to determine the source of the PL and to measure the effect of sample defects on the PL. The PL images are simply infra-red images taken with the spectrometer. The setup is shown in Figure 3.6. The collection optics produce an image of the sample on the entrance slits of the spectrometer. When measuring standard PL spectra, these slits are set to a width of 0.1mm to obtain adequate wavelength resolution. However, in imaging mode, these slits are opened to their maximum extent of 2mm and the grating is positioned so that the 0th order reflection is detected. At this position there is no dispersion of light of different wavelengths. The curved mirrors focus the light onto the detector, where an image of the sample is produced. Optical filters were used at the entrance slits to eliminate scattered laser light.

To magnify the image, the collection optics can be varied. The maximum magnification was obtained using a 40X microscope objective lens placed approximately 1mm from the sample. A lens with a focal length of 50cm was then used to focus the image of the sample onto the detector. This produced an overall magnification of 30X and a resolution of 0.9μm/pixel on the CCD array.

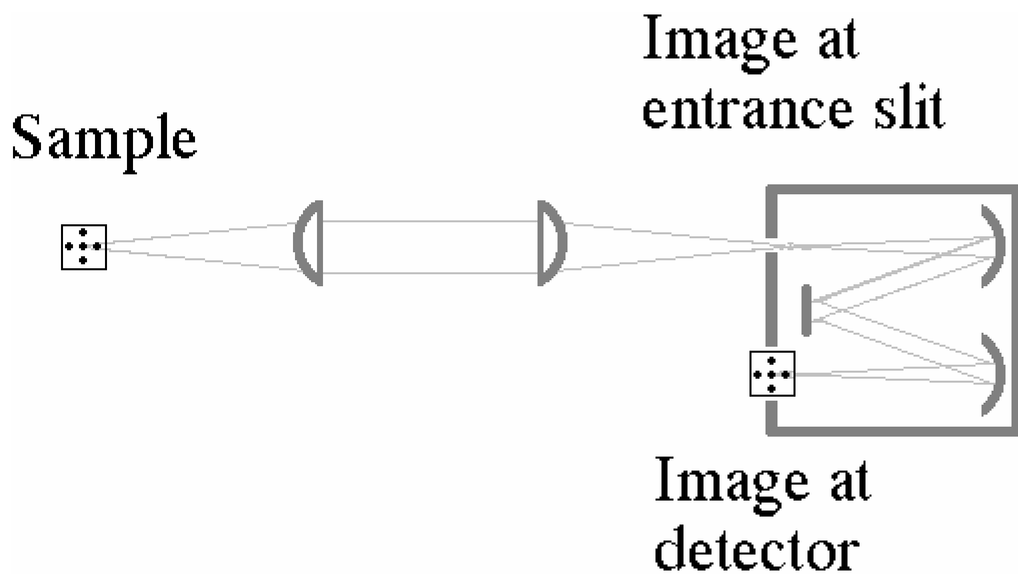

Figure 3.6 Schematic of the setup for PL imaging.

There was a significant amount of chromatic aberration due to the collection optics. This limited the range of wavelengths that could be focussed, restricting images to sources with a narrow spectral distribution. In this thesis, PL imaging was used for qualitative investigations only, since the reliability of the quantitative information contained in the images was limited by the effects of chromatic aberrations, uneven illumination, and variations in detector efficiency with wavelength, and changes in focusing conditions.

PL profiling was also performed with this spectrometer. This method consists of measuring the PL intensity as a function of wavelength and position in one dimension. By narrowing the entrance slit to 0.1mm, only light coming from a narrow region of the sample enters the spectrometer. The grating is rotated so that the 1st order reflection is detected by the CCD. In this configuration, the grating disperses light from different wavelengths at different angles. Therefore, each column of pixels in the CCD array corresponds to a particular wavelength, while each row of pixels corresponds to a particular position along a narrow

strip of the sample. The image produced by the CCD array represents the PL intensity as a function of wavelength and position.

3.3.c Scanning Electron Microscopy (SEM)

Scanning electron microscopy (SEM) was used to analyse sample cross sections in order to extract layer thickness and to examine thin film cracks.

Most of the SEM micrographs were obtained using a Cambridge S360 SEM, with an acceleration voltage of 20kV, a probe current of about 425pA and a working distance of 13mm. The images were produced using either back-scattered electrons or secondary electrons. In backscatter mode, the signal was much weaker but gave greater contrast between silicon and SiO_2. A Hitachi S4500 Field Emission SEM was also used for imaging of selected samples at high-resolution.

Cross-sections of the sample were prepared to examine the microcavity structure and their cracks. To do this, the samples were first embedded in Epotech epoxy to protect the cracked surface during the polishing. Various grades of silicon carbide paper were then used to polish the sample cross-section. The final polish was performed with a suspension of 0.5μm colloidal silica on soft lap. After polishing, a layer of either carbon or gold/palladium alloy was deposited onto the samples to make them conductive.

3.3.d Focused Ion Beam

A focused ion beam (FIB) system provided an alternative method of preparing sample cross sections. In this method, a focused beam of Ga^+ ions was used to mill a trench into the sample. The exposed surface was then imaged using an in-situ SEM. This is illustrated in

Figure 3.7. The focused ion beam system used was an FEI Nova NanoLab 200 Dualbeam FIB/SEM, located at the University of New South Wales.

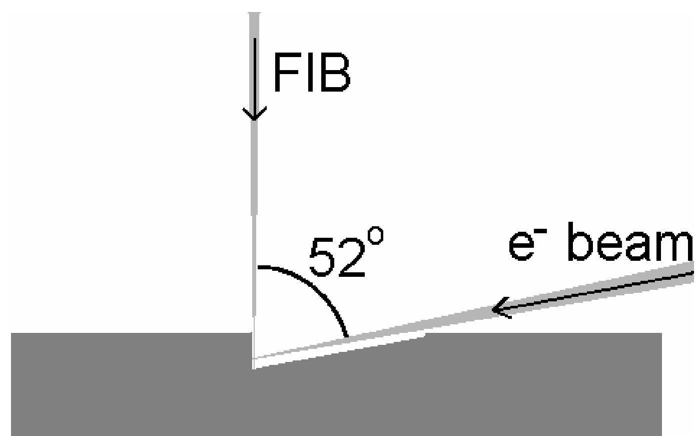

Figure 3.7 Schematic of the geometry of the FIB measurement.

3.3.e Transmission Electron Microscopy

Imaging of the nanocrystals was performed using transmission electron microscopy (TEM) in order to determine the size distribution of the nanocrystals. As samples must be electron transparent, they were thinned in the following manner. First, a 3mm diameter disk was cut from a larger sample using an ultrasonic disc cutter. The back of the sample was then polished with a disc grinder until the sample thickness was reduced to 100μm. A spherical dimple grinder was then used to reduce the thickness at the centre of the sample to about 20 μm. The dimpled sample was then etched in a solution of 5:1 70% HNO_3 and 49% HF for about three minutes until a very small perforation was observed. Because the silicon oxide layers are transparent, it is possible to confuse the point where the acid etches through the substrate only, with a perforation of the sample. However, once the oxide layer is perforated, it is easy to observe the edge of the hole in the transparent oxide. The sample was then ion milled using an argon beam to enlarge the perforation. Images were then taken using a Phillips CM300 TEM. These steps are summarised in Figure 3.8.

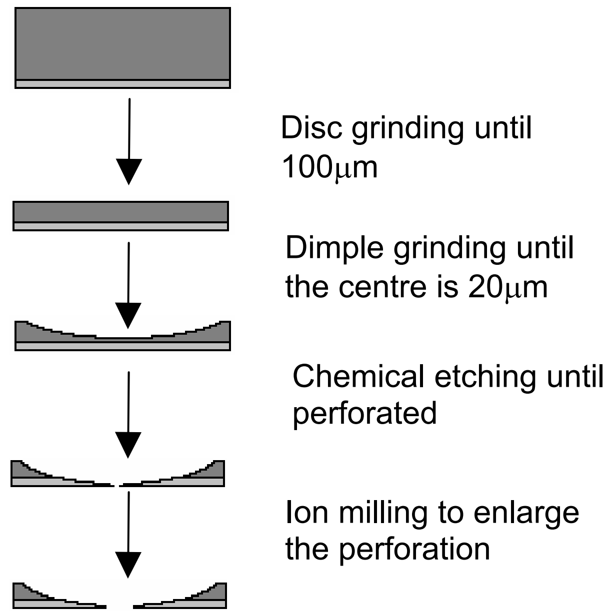

Figure 3.8 The procedure used for TEM sample preparation.

3.4 Ion Beam Equipment

3.4.a Ion Implantation

Impurities were introduced into the silicon-rich oxides using a low energy implanter, a schematic of which is shown in Figure 3.9. This machine uses a Cs sputter source to produce various negative ions. The ions are accelerated using a high voltage supply and then mass analysed using a 90° analysing magnet before impinging on the sample. The ion current on the sample is measured and integrated to determine the ion fluence. The low energy implanter is capable of implanting ions with energies between 20 and 150keV per ion.

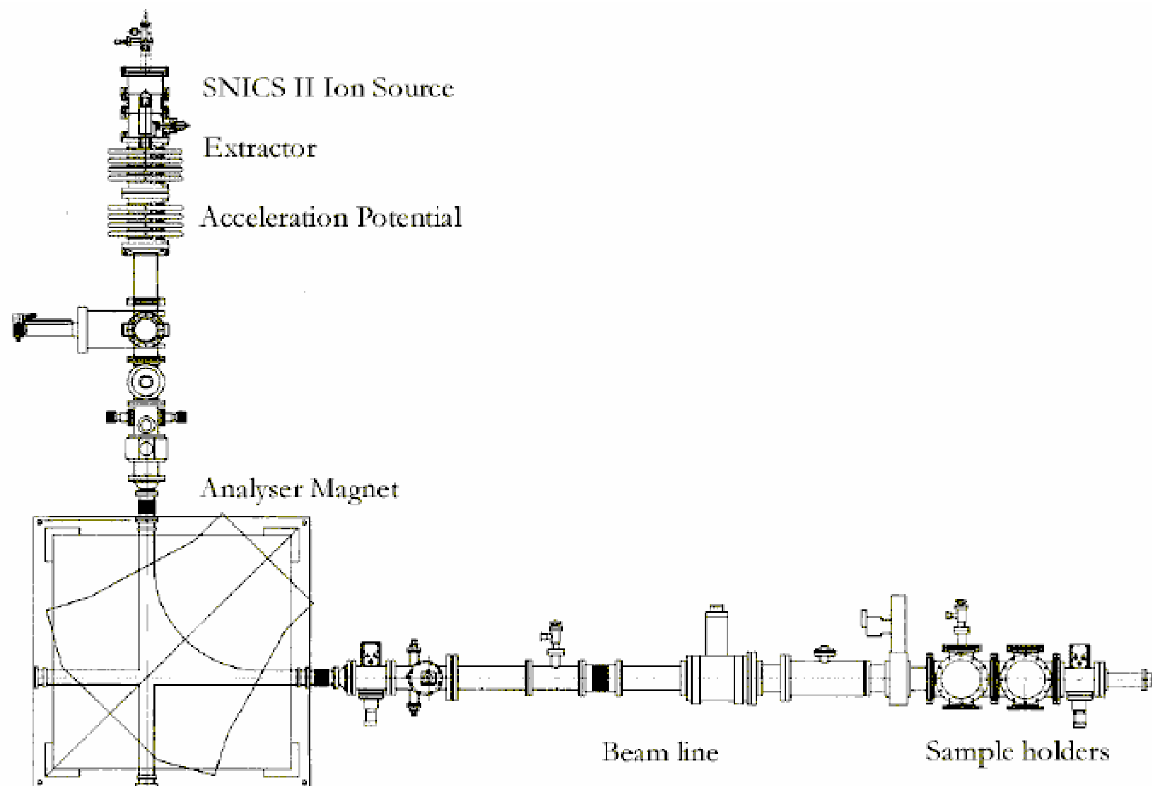

Figure 3.9 Schematic of the low energy implanter at the ANU.

A high energy implanter was used to implant silicon into SiO_2 to produce silicon rich oxides. A schematic of this system is shown in Figure 3.10. This is a tandem accelerator that takes negative ions, produced in a similar manner to that of the low energy implanter described above, and further accelerates them. When the negative ions reach the terminal, which has a maximum voltage of 1.7 MV, they interact with nitrogen gas, causing some ions to lose electrons and become positively charged. These positive ions are then accelerated away from the positively charged terminal, energy analysed and directed towards the sample. The ANU high energy implanter is capable of producing ion beams with energies of up to 3.5MeV for singly charged ions.

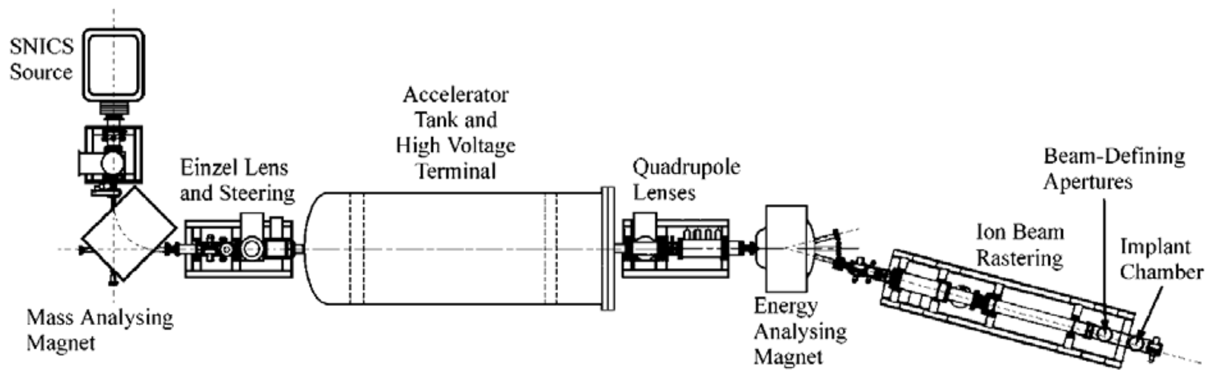

Figure 3.10 Schematic of the high energy implanter.

3.4.b Rutherford Backscattering Spectroscopy (RBS)

Rutherford Backscattering spectroscopy was employed to measure the composition of the PECVD deposited and ion implanted films. The technique is well described in detail in standard textbooks[50]. It consists of measuring the energy distribution of helium ions after being elastically scattered from the sample. When the ions collide with a sample atom, some will be backscattered towards one of the detectors. The energy of the backscattered ion depends on the mass of the scattering atom. In addition, the ions lose energy to electrons on both their inward and outward paths if the scattering atom is below the sample surface. The energy of the backscattered ion therefore depends on the mass of the scattering atom as well as its depth. The energy distribution can be deconvoluted to provide both composition and depth information.

All of the RBS measurements reported in this thesis were performed with an incident beam of 2MeV He ions. Surface barrier detectors at 15° and 67° from the incident beam direction were used to measure energy of the backscattered ions, as depicted in Figure 3.11(a).

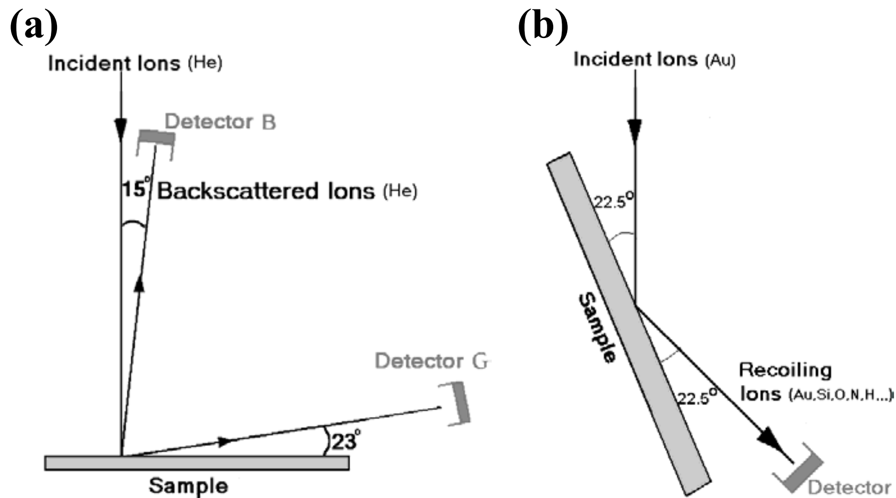

Figure 3.11 Schematics showing the geometry of (a) the RBS measurements and (b) the ERDA measurement.

3.4.c Elastic Recoil Detection (ERD)

Over recent years, a heavy ion elastic recoil detection system has been developed at the National Heavy Ion Facility at the ANU[51]. This system was used to measure the composition of the film used in this present work including the hydrogen contents of these films. For these measurements, high energy (200 MeV) gold ions are used to recoil target atoms into a gas-ionisation detector[52] capable of measuring the energy spectra for each species, see Figure 3.11(b). This technique is more sensitive to elements with a low atomic mass than RBS and is capable of detecting hydrogen[53].

3.5 Stress measurements

In this study the stress in thin films was determined from wafer curvature measurements performed with an optical shear plate. A stressed film on a substrate will tend to cause the substrate to curve. The stress in the film can be determined using the Stoney equation[54]:

$$\sigma = \frac{E_s}{6(1-\nu_s)} \frac{t_s^2}{t_f} \left(\frac{1}{R_1} - \frac{1}{R_0} \right) \qquad \textbf{Equation 3.3}$$

where σ is the stress in the film, E_s and ν_s are the substrates modulus of elasticity and Poisson ratio, t_s and t_f are the thicknesses of the substrate and the film, and R_1 and R_0 are the radius of curvature for the stressed and unstressed wafers.

Shear plates are often employed to test the collimation of laser beams, but can also be used to determine the radius of curvature of reflective surfaces.[55] A shear plate consists of a wedge shaped prism. The laser beam reflects off both the front and rear surfaces of this prism, projecting two overlapping images onto a screen. Where the two images overlap, interference fringes form as shown in figures 3.12 and 3.13. If a set of plane waves is incident on the shear plate, the interference fringes are parallel to a reference line where the fringe spacing (d) is related to the laser wavelength (λ), index of the shear plate (n) and angle of the fringes (α) by:

$$d = \frac{\lambda}{2 n \alpha} \quad \textbf{Equation 3.4}$$

If spherical waves are incident on the shear plate, then the radius of curvature of the wavefront at the screen will be given by:

$$R = \frac{S d}{\lambda \sin(\alpha)} \quad \textbf{Equation 3.5}$$

where S is the ‘shear’ (the distance between the two images) and the fringe spacing is measured perpendicular to the fringe direction.

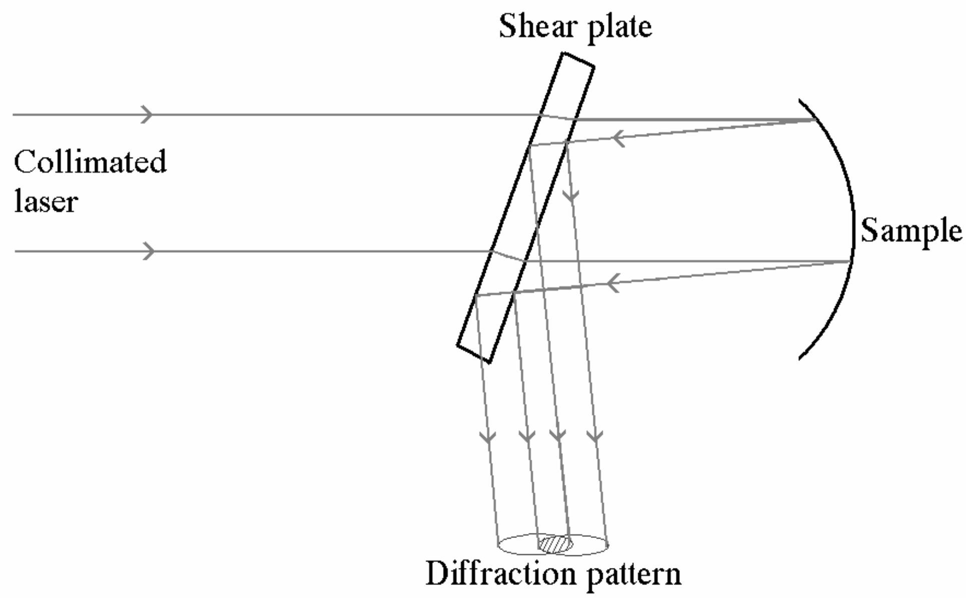

Figure 3.12 Ray diagram of a shear plate.

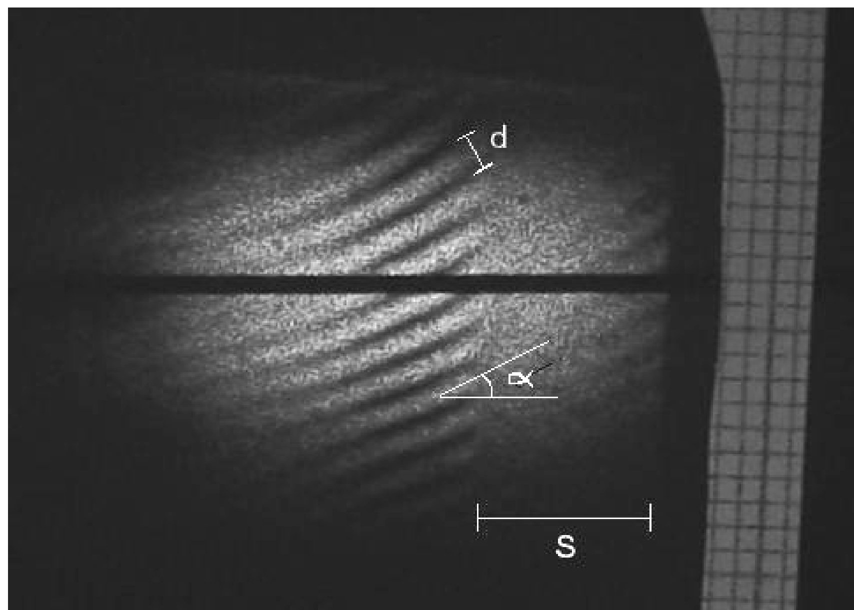

Figure 3.13 Image of a typical diffraction pattern using the shear plate.

To measure the radius of curvature of a sample, a collimated laser beam is reflected off the sample and the shear plate used to monitor the reflected beam. Using the radius of curvature R of the reflected wavefront, the radius of curvature of the sample R_{sample} can then be determined:

$$R_{sample} = 2(R \pm L) \qquad \textbf{Equation 3.6}$$

where L is the distance between the sample and the screen. The positive sign is used for a diverging beam (concave samples) while the negative sign is used for a converging beam (convex samples).

This setup is capable of measuring radii of curvature of 300m or more with an uncertainty of about 20m. For a 1.2μm thin film on a 0.5mm silicon substrate, this corresponds to a stress of 27 ± 2 MPa. Aside from the precision with which the parameters α, d, S and L can be determined, the main limit to this measurement is the uniformity of the curvature across the sample.

Chapter 4 Components & their Properties

This chapter deals with the properties of the different PECVD materials used in this study. Section 4.1 deals with determining the index of refraction and the thicknesses of the deposited materials, which vary as a function of the deposition and annealing conditions. These parameters are required to adequately model the optical properties of the structures discussed in chapter 4. In section 4.2, the RBS and ERD analysis of the elemental composition of the films are presented. In section 4.3, the size distribution of the nanocrystals is determined based on TEM images of the nanocrystals. Section 4.4 deals with the various parameters that may affect the PL of the materials such as composition and annealing conditions. The mechanical properties of these materials are discussed later in chapter 5.

4.1 Thickness & index

For accurate modelling of microcavities it is important to have accurate values for the index of refraction and film thickness. The two principal methods employed in the current study for determining these parameters are the M-line spectrometer and the Film-tek spectrometer (see chapter 2 for details). The indices of refraction and the PECVD deposition rate obtained by the two methods are compared in Table 4.1.

4.1.a M-line

Figure 4.1 shows the effect of annealing temperature on the index of refraction and thickness of PECVD deposited SiO_2, and silicon-rich oxides. All of the samples were annealed for 1 hour in N_2. The properties of the SiO_2 layers do not change significantly during a 1 hour anneal at temperatures up to 1150°C. For the silicon-rich oxides, the index

of refraction increases and the thickness decreases when the sample is annealed. These changes are more significant for the samples with the higher excess silicon content. The M-line spectrometer was not capable of measuring the thickness and refractive index of the silicon nitride layer because of its high index of refraction.

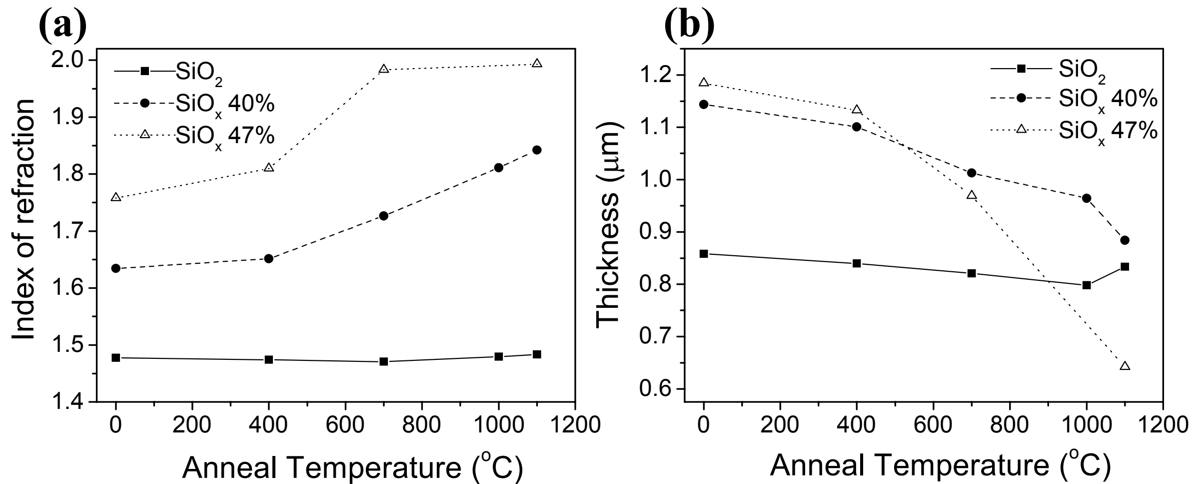

Figure 4.1 (a) Index of refraction at 810 nm of PECVD SiO_2 and silicon-rich oxides as a function of anneal temperature. (b) Sample thickness as a function of anneal temperature. All anneals were for one hour in N_2.

4.1.b Filmtek

For each of the materials used to make the microcavities, the indices of refraction were determined as a function of wavelength and anneal conditions, using a Filmtek spectrometer. This system measures the reflectivity of the sample at 0° and 70°, and then fits a model to the data. The results for SiO_x (40% Si) and silicon nitride are shown in Figure 4.2. The samples were annealed for 1 hour in N_2 at temperatures varying from 400°C to 1150°C. The film-tek results for SiO_2 (not shown) indicate that, as a result of the annealing, the index of refraction and thickness of SiO_2 does not vary more than 1% and 3% respectively. This is within the reproducibility of the PECVD system. The SiO_x and silicon nitride layers varied considerably more. The refractive index of SiO_x increased by

12% while its thickness decreased by 22%. The silicon nitride layer underwent a similar increase in refractive index (16%) and decrease in thickness (20%).

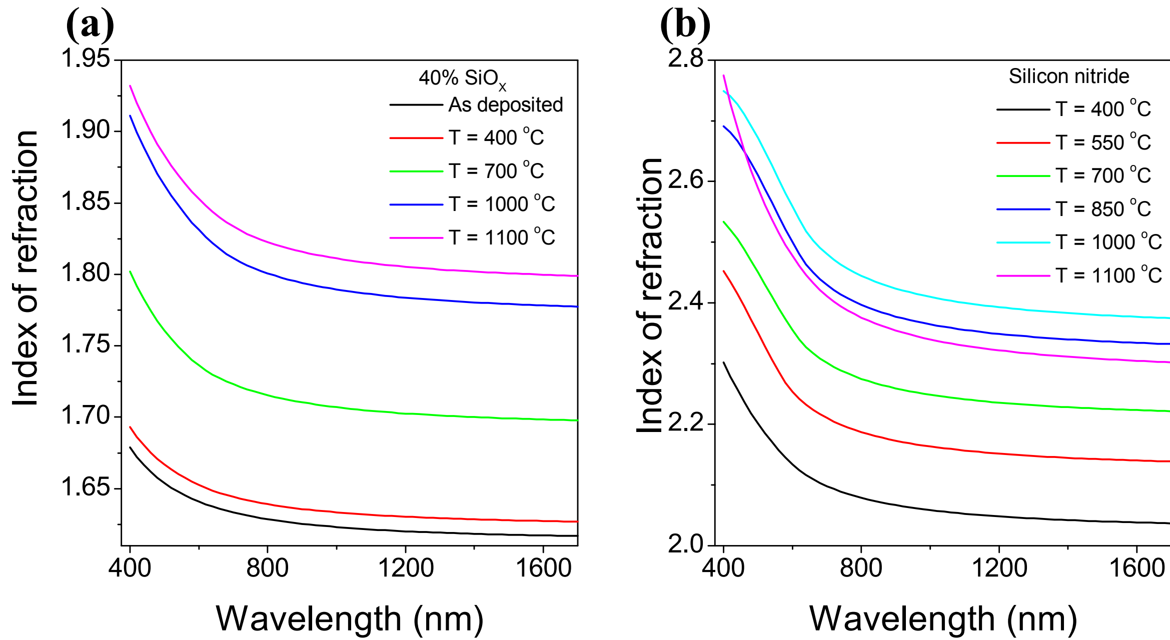

Figure 4.2 Index of refraction as a function of wavelength for (a) the 40% SiO_x and (b) the silicon nitride layer annealed for one hour at various temperatures.

The considerable decrease in thickness of the silicon nitride was confirmed by profilometer measurements. Mesa structures were produced by masking the silicon nitride layer with wax then etching away the uncovered regions with an 8% HF solution. The height of the mesa was measured before and after annealing at 1100°C and shows a decrease in thickness of 23%, consistent with the optical measurements.

The change in refractive index is due to the densification of the film as well as changes in the composition of the film. It will be shown in section 4.2 that hydrogen is released from these films as the samples are annealed.

Material	Index of refraction Film-tek	Index of refraction M-line	Deposition rate (nm/s)
SiO_2	1.47	1.48	0.86 ± 0.04
SiO_x 36%		1.60	0.86 ± 0.04
SiO_x 40%	1.82	1.83	0.74 ± 0.04
SiO_x 47%		1.99	0.68 ± 0.03
Silicon nitride	2.37		0.34 ± 0.02

Table 4.1 Index of refraction at 810nm after an 1100°C anneal for 1 hour and the PECVD deposition rate for the various materials.

4.2 Composition

4.2.a RBS results

In order to determine the amount of excess silicon available to form nanocrystals, RBS analysis was performed. Nitrogen was detected in addition to silicon and oxygen. The relative fractions of each element in the silicon-rich oxides are listed in Table 4.1. It is difficult to make an accurate determination of the concentration of both oxygen and nitrogen because they have a similar atomic mass and their peaks overlap. Figure 4.3 shows a typical RBS spectrum of the PECVD silicon-rich oxides. This particular spectrum corresponds to a 36% SiO_x layer.

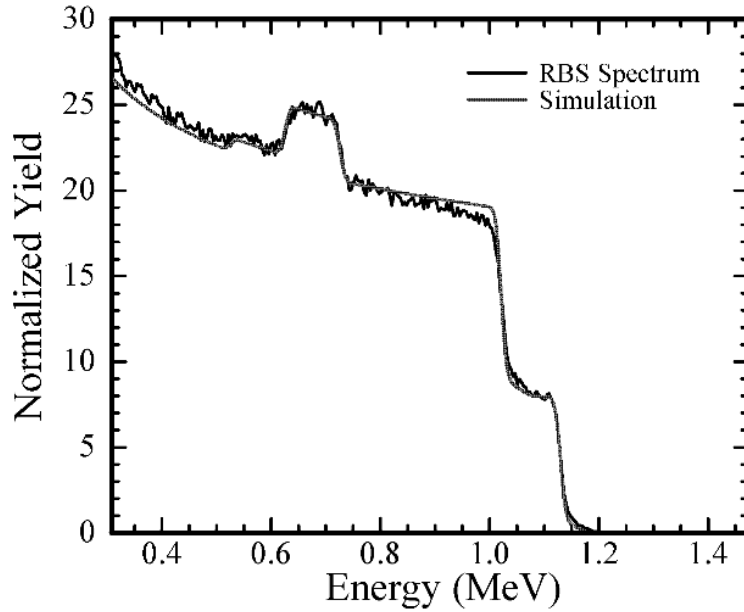

Figure 4.3 RBS spectrum of PECVD (36%) silicon-rich oxide.

Material	[Si]	[O] (± 0.1)	[N] (± 0.05)	
SiO_x 36%	1	1.4	0.4	$SiO_{1.4}N_{0.4}$
SiO_x 40%	1	1.2	0.4	$SiO_{1.2}N_{0.4}$
SiO_x 47%	1	1	0.4	$SiON_{0.4}$
SiO_x 52%	1	0.8	0.4	$SiO_{0.8}N_{0.4}$

Table 4.2 Relative elemental concentrations of silicon-rich oxides as determined by RBS.

4.2.b ERD results

To more accurately determine the concentration of the films, heavy ion elastic recoil detection (ERD) was performed on the different samples. Heavy ion ERD analysis can more easily distinguish between oxygen and nitrogen. It is also sensitive to light atoms such as hydrogen, which are impossible to measure using RBS. In order to get a more accurate measurement of the composition of the sample, silicon-rich oxide layers were deposited onto a germanium substrate. In this way recoils of substrate atoms are easily resolved from

the silicon in the film. The results of the heavy ion ERD analysis give the elemental composition of the samples in Figure 4.4. It shows that the SiO_2 is very close to a stoichiometric oxide with some hydrogen. The silicon-rich oxides have a significant amount of nitrogen and hydrogen in them. A very small amount of carbon was also detected in all of the samples.

Material	[Si]	[O]	[N]	[H]	[C]
SiO_2	1	2.13 ± 0.07	0.05 ± 0.005	0.57 ± 0.008	0.011
SiO_x 36%	1	1.42 ± 0.03	0.36 ± 0.01	0.65 ± 0.007	0.006
SiO_x 40%	1	1.16 ± 0.02	0.37 ± 0.01	0.72 ± 0.007	0.008
SiO_x 47%	1	0.85 ± 0.02	0.30 ± 0.01	0.69 ± 0.006	0.007
SiO_x 52%	1	0.64 ± 0.02	0.28 ± 0.01	0.75 ± 0.005	0.008
Silicon nitride	1	0.04 ± 0.004	0.83 ± 0.02	0.86 ± 0.008	0.012

Figure 4.4 Relative elemental composition of the materials as determined by heavy ion ERD.

The composition of the 36 and 40% silicon-rich oxides determined by ERD agree with the values obtained by RBS. However there are small discrepancies between the compositions determined by the two methods. Since the measurements were not performed on the same samples produced in the same PECVD run, the discrepancy may be due to variation in composition. Particularly with low NO_2 flowrates, small variations in flow in the PECVD chamber have a large effect on the composition of the sample.

The impurities of H, N, and C in the silicon-rich oxides are a consequence of the gases used in the PECVD chamber. SiH_4 and NO_2 are used as source gases for silicon and oxygen, respectively. However, these gases also contribute hydrogen and nitrogen to the plasma and these inevitably get incorporated into the film. The carbon may come from residual CO_2 or organic contamination from the chamber walls.

The percentages used to identify the different silicon rich oxides refer to the concentration of silicon in atomic percent without considering the contribution of hydrogen which is volatile and easily released from the sample. Spectra of the 2D energy loss spectrum of the recoil ions from the 40% silicon-rich sample are shown in Figure 4.5 before and after annealing. The sample was annealed at 1100°C for 1 hour in N_2. In this case, the films were deposited on a silicon substrate, allowing anneal temperatures above the melting point of germanium (938°C). The results indicate that the concentration of hydrogen drops from 20.6 atomic % to 0.2 atomic % during a 1 hour anneal at 1100 °C. Similarly, measurements on the silicon nitride films show a reduction from 27.1% to 1.6%. Weijers et al[21] have shown that a similar decrease in hydrogen content is observed in other silicon-rich oxides.

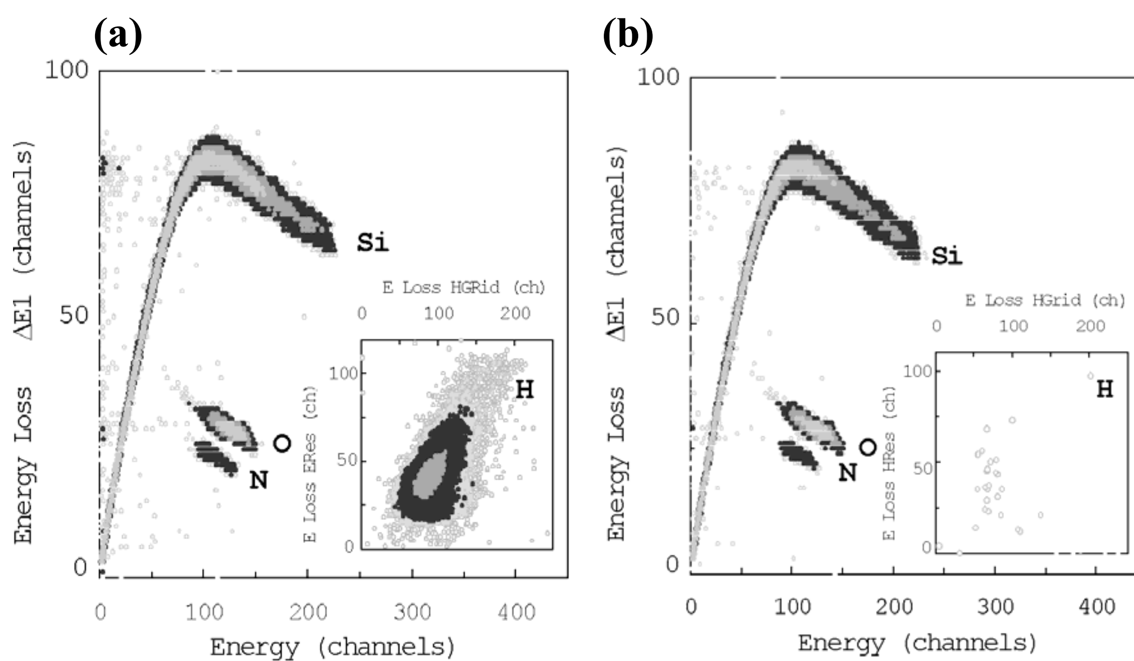

Figure 4.5 (a) 2-D heavy ion ERD spectrum of sample before annealing and (b) 2-D heavy ion ERD spectrum of sample after annealing at 1100 °C for 1h.

4.3 Structural properties of nanocrystals

Figure 4.6 shows TEM images of silicon nanocrystals produced by annealing 40% silicon-rich oxide deposited by PECVD. The histogram in Figure 4.7 shows the distribution of the diameter of the nanocrystals observed in an area of 12 000nm^2. The nanocrystals are approximately spherical with a mean diameter of 4.3nm and a standard deviation of 0.7nm. Similar measurements were performed on the 36% and 47% SiO_x samples.

No nanocrystals were seen in the 36% samples while the nanocrystals observed on the 47% sample were not easily resolved. The measured diameter of the nanocrystals formed from the 47% SiO_x is 4.9nm with a standard deviation of 0.9nm. However this value may be skewed to larger values because contrast in the image was not very high making the nanocrystals difficult to resolve. The probability of observing larger nanocrystals was greater than that for smaller nanocrystals.

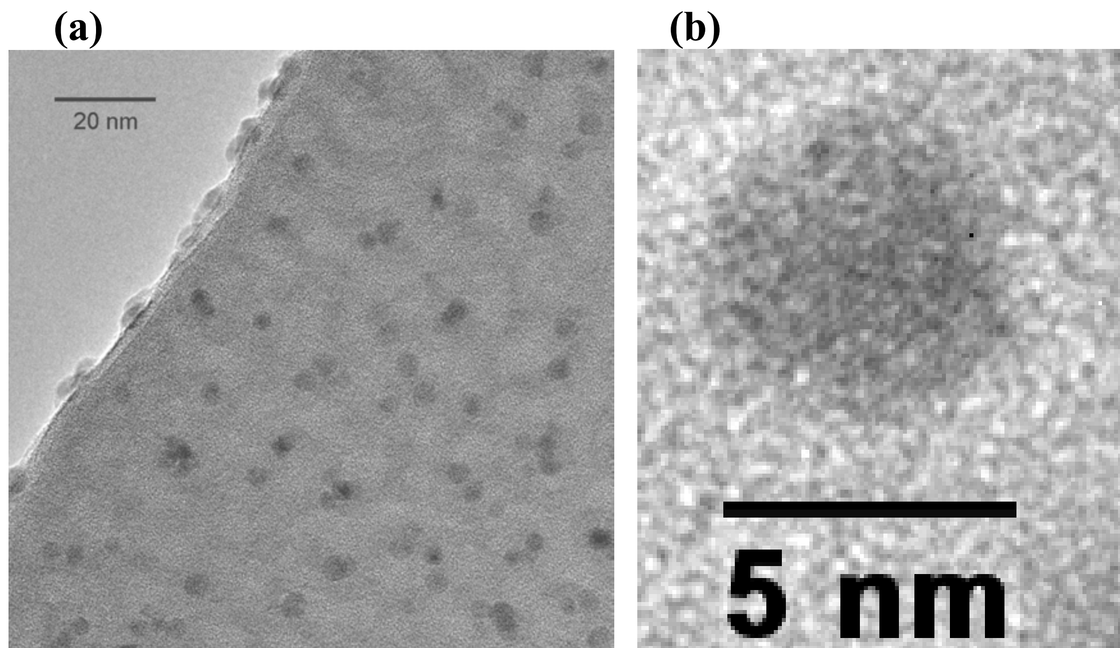

Figure 4.6 TEM images of silicon nanocrystals in 40% SiO_x annealed for 1 hour in N_2.

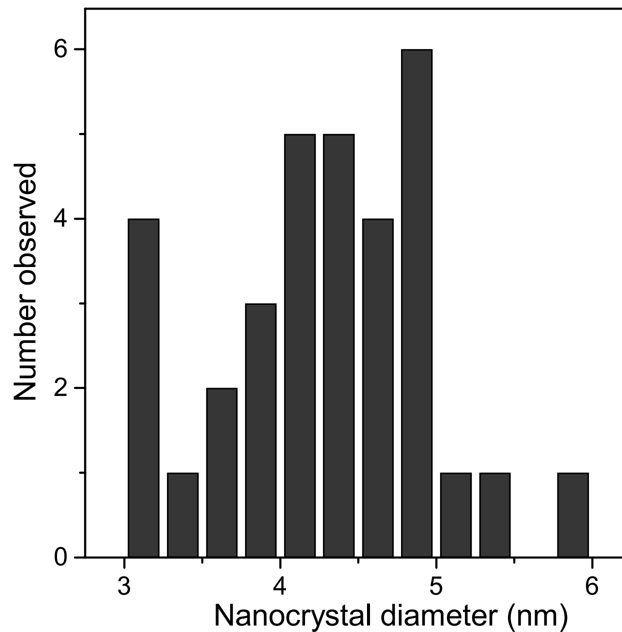

Figure 4.7 Histogram of the size distribution of the silicon nanocrystals in SiO_2.

4.4 Photoluminescence

4.4.a Effect of sample composition

The PL spectra of PECVD deposited silicon-rich layers with different nominal silicon contents after a one hour anneal at 1100ºC are compared in Figure 4.8. Measurements of stoichiometric SiO_2 did not show any measurable PL. As the silicon content is increased, the PL intensity increases until an optimal content of between 40 and 47% silicon in agreement with Garrido et al[14].

As the excess silicon concentration is increased, there is an increase in both the size and the density of nanocrystals. Initially the PL intensity should increase with the amount of excess silicon. However for silicon concentration beyond about 45 atomic percent, the

nanocrystals form close enough to interact[14] increasing the probability that excited carriers find defects and decay non-radiatively

The 40% Si sample was chosen to be the standard composition used in the microcavity experiments. This is because the complete spectrum of this strong PL peak can easily be measured. In the case of the compositions with larger Si content, there is a significant proportion of the spectrum that is emitted at wavelengths above 1000nm, where the signal cannot be reliably measured with the CCD detector employed for PL measurements.

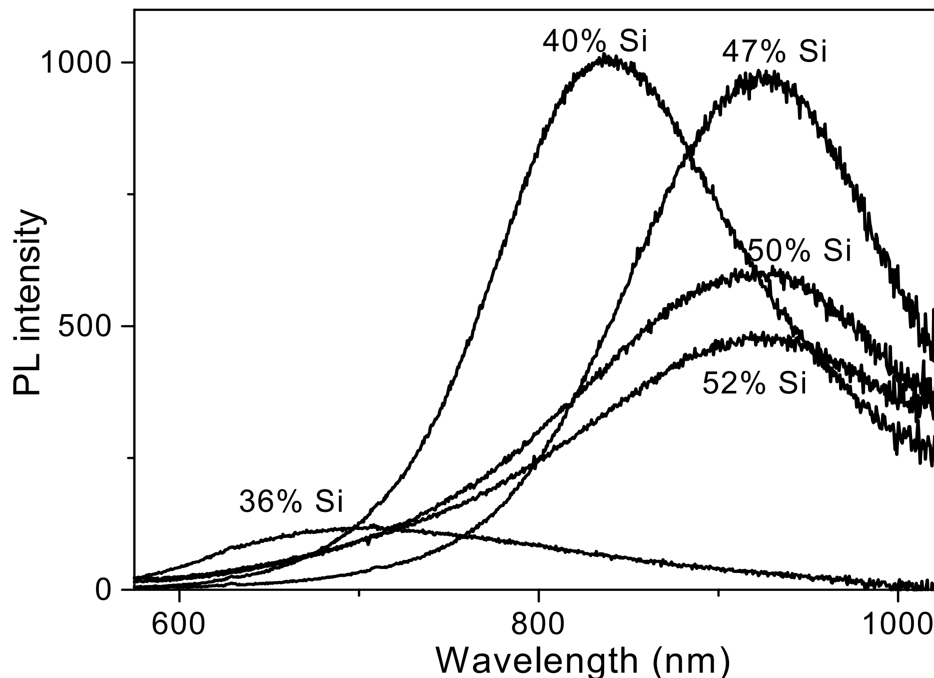

Figure 4.8 PL spectra of 255nm thick silicon-rich layers with various silicon concentrations after annealing at 1100 °C in N_2 for 1 hour.

4.4.b Effect of anneal time

Figure 4.9 shows the PL spectra of silicon-rich oxide layers annealed for different amount of time at 1100°C in N_2. The 40% SiO_x samples shows no measurable PL as-deposited. The majority of the nanocrystal seem to form in the first 30 minutes of annealing. This can be

seen by the shift in peak emission wavelength. After this, increasing the anneal time primarily removes defects from the nanocrystals leading to more efficient emission. It can be seen that the peak emission wavelength shifts to longer wavelengths between the 10 and 30 minute anneal but then does not shift significantly for longer anneal times. This indicates that there is no significant change in the average size of the luminescing nanocrystals after 30 minutes of annealing.

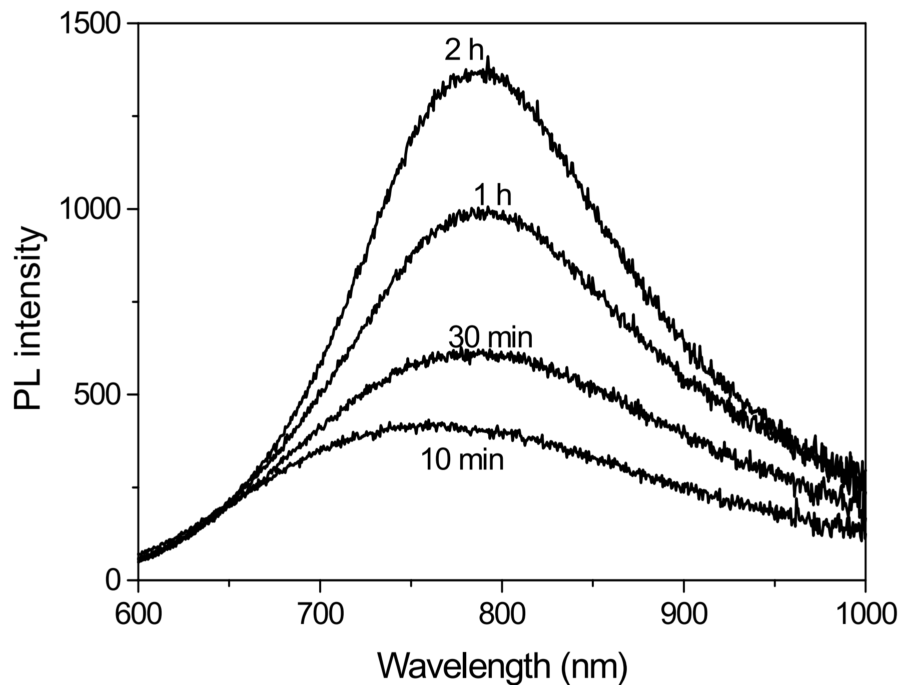

Figure 4.9 PL spectra of a 255 nm thick, 40% Si SiO_x layer annealed for various amounts of time.

4.4.c Effect of anneal temperature

To assess the effect of annealing on the PL of the nanocrystals, a series of isochronal anneals was performed on a 40% SiO_x layer, a SiO_2 layer and a silicon nitride layer. The anneals were performed in N_2 for one hour at temperatures ranging from 400 to 1150°C. The resulting PL spectra are shown in Figure 4.10.

i) Silicon Oxides

There was no measurable PL from the nominally stoichiometric SiO_2 layers under any annealing conditions.

As the anneal temperature is increased, the PL increases and shifts to longer wavelengths. For anneal temperature of 1000°C or less, the PL is weak. After an anneal at 1150 °C, there is a significant increase in PL intensity.

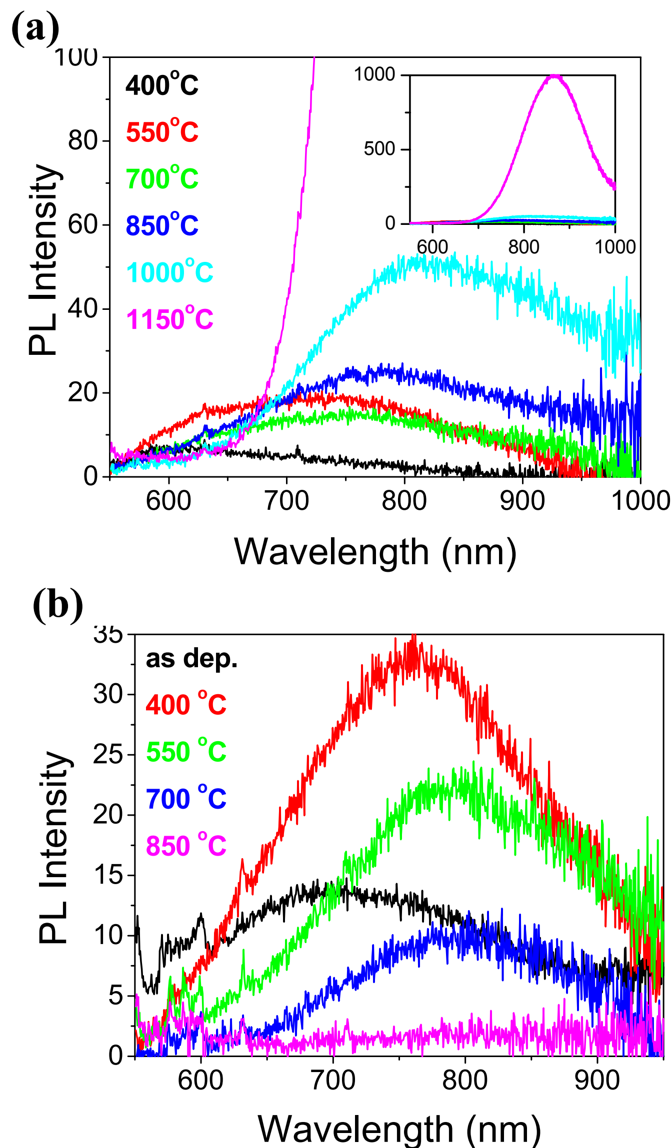

Figure 4.10 PL spectra of (a) a 255 nm 40% SiO_x layer and (b) a 95 nm silicon nitride layer annealed for 1 hour at various temperatures.

ii) Silicon Nitride

The silicon nitride layers show a different trend. These samples show weak PL as-deposited which increases after annealing at 400°C. However annealing beyond 400°C causes a decrease in PL. No measurable PL has been detected for samples annealed at or above 850°C. A similar trend has also been observed by Aydmh et al.[56] who attributed the PL to emission from amorphous silicon clusters in silicon nitride. They correlated the reduction in PL to a reduction in the number of Si-H and N-H bonds and speculated that the reduction in nano-cluster luminescence resulted from an increase in non-radiative dangling bonds as hydrogen was released from the sample.

4.4.d Effect of passivation

i) Passivation of SiO_x

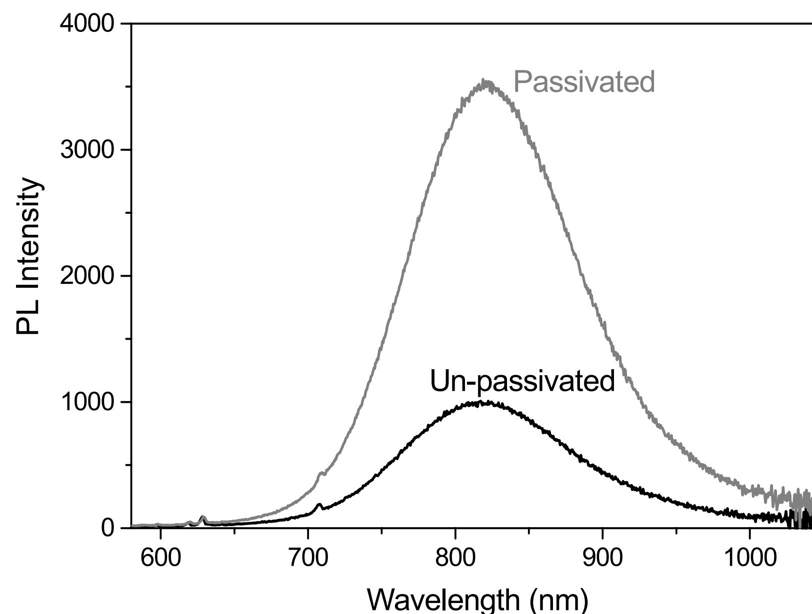

Figure 4.11 The effect of passivation on the PL spectrum of a 40% SiO_x layer annealed at 1100°C for one hour in N_2. The black curve represents the spectrum after the anneal and the grey curve is that of the sample after a one hour passivation anneal at 500 °C in forming gas (5% H_2 in N_2).

Hydrogen increases the luminescence of silicon nanocrystals by passivating defects at the Si/SiO_2 interface. Figure 4.11 shows the typical effect of hydrogen passivation on PECVD SiO_x. In this example, a 40% SiO_x layer on silicon has been annealed at 1100ºC in N_2 for one hour. The sample was then cut into two pieces, one of which was then annealed in forming gas at 500ºC for one hour. The PL of these two samples was then measured and compared. The PL of the hydrogen passivated samples is 3.1 ± 0.2 times that of the unpassivated sample. Experiments performed by others[57, 58] investigating the passivation of silicon nanocrystals formed by ion implantation in SiO_2, show similar results.

The effect of passivation on the silicon-rich oxides as a function of anneal time is presented in Figure 4.12. This shows that the effect of passivation is more pronounced for the films containing a higher silicon concentration. The enhancement factor observed can be as high as 10 for the 52% SiO_x after a one hour anneal. In general, the samples with the higher silicon content benefited more from the passivation. The enhancement of the 52% sample annealed for one hour was a factor of ten. This is not unexpected as the samples with the highest silicon content have larger nanocrystals which are more likely to contain defects.

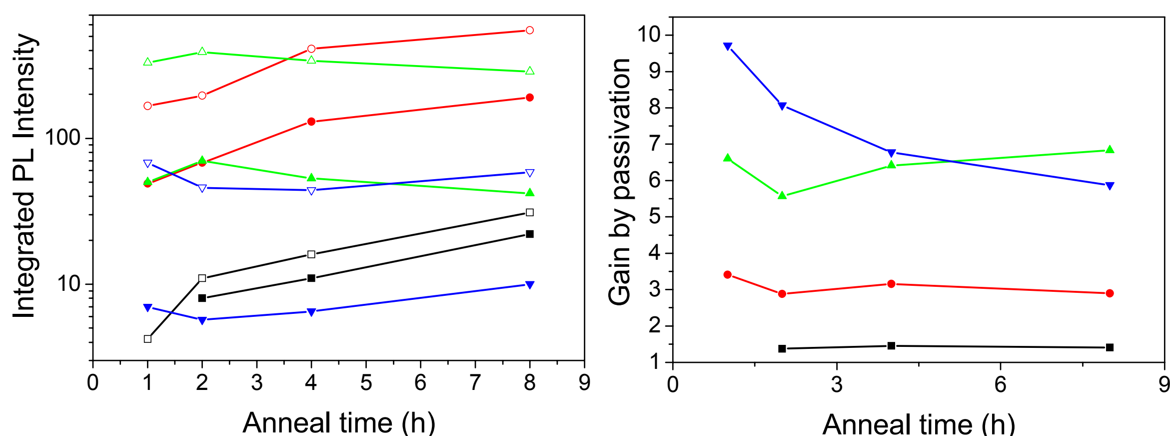

Figure 4.12 (a) Effect of passivation on the integrated PL intensity and (b) the gain achieved by passivation for (■) the 36% SiO_x, (●) 40% SiO_x, (▲) 47% SiO_x and (▼) 52% SiO_x. In (a), the solid symbols represent the unpassivated samples and the open symbols represent the passivated samples.

ii) Passivation of silicon nitride

Hydrogen can also have a profound effect on the PL from nitride layers[56, 59]. Silicon nitride layers were deposited and then annealed at 400°C for 1 hour in either N_2 or forming gas. Figure 4.13 compares the PL from these two samples. The sample annealed in forming gas shows stronger PL.

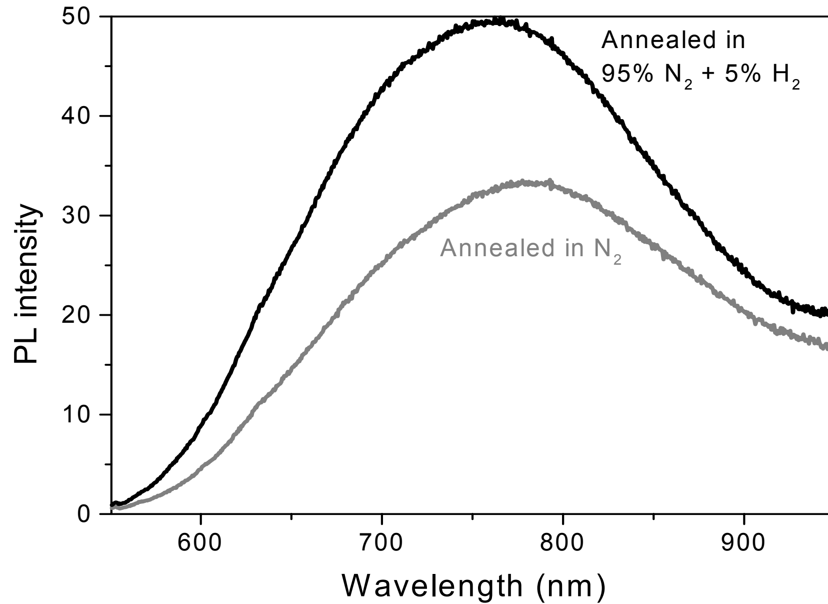

Figure 4.13 PL spectra of silicon nitride annealed at 400 °C for 1h in either N_2 or forming gas (N_2 + 5% H_2).

iii) Nitride passivation of SiO_x

A fortuitous consequence of the high hydrogen content of the nitride films is that this hydrogen can be used to passivate silicon nanocrystals. This passivation scheme which is illustrated in Figure 4.14, is similar to that used by researchers to passivate the Si/SiO_2 interface of solar cells[29, 30], where a thermal oxide is grown on the silicon surface followed by a nitride layer and a 30s anneal at 730°C. The anneal releases hydrogen which diffuses to the interface. The diffusion constant of hydrogen in Si_3N_4[60] is much lower than in SiO_2[61],

therefore the nitride layer prevents the release of hydrogen. This technique has been modified to apply to the passivation of silicon nanocrystals in SiO_2.

To form the nanocrystals, a nitride layer then a SiO_x layer were deposited on a silicon substrate and annealed for 1 hour at 1100°C. Unfortunately, the anneal required to form the nanocrystal also releases all the hydrogen from the sample. A second nitride layer was then deposited onto the nanocrystal layer as a source of hydrogen. The sample was cleaved into two pieces, one of which was annealed at 1000°C for 15s to release the hydrogen into the SiO_x layer and passivate the nanocrystals. The PL of the sample before and after this passivation anneal is shown in Figure 4.15(a). The enhancement in PL due to this passivation is a factor of 4.3.

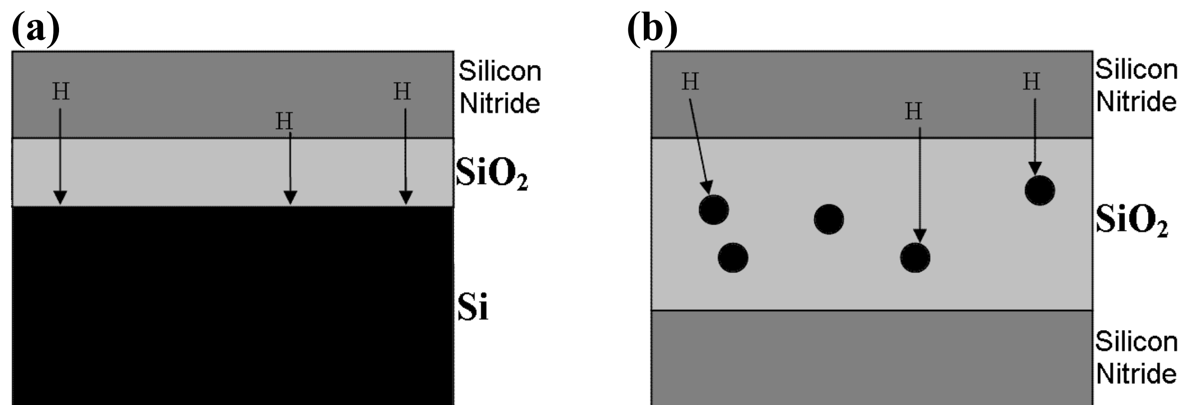

Figure 4.14 Schematic of nitride passivation of (a) a Si/SiO_2 interface and (b) of silicon nanocrystals in SiO_2.

It is interesting to note that a nitride-SiO_x-nitride stack deposited on silicon, and then annealed for 15s at 1000°C, has much stronger PL than that of its individual component layers annealed under the same conditions, as shown in Figure 4.15(b). The PL spectrum from the stack is remarkably similar to that of the SiO_x layer but 24 times more intense. To get this strong enhancement it is necessary to anneal the SiO_x between two nitride layers.

Therefore even after a 15s anneal the SiO_x layer, can produce some PL which can be enhanced by hydrogen passivation. Due to the short anneal time, it is not clear if silicon nanocrystals will form, however amorphous silicon nanoclusters are also photoluminescent[62]. If this PL is due to silicon nanocrystals or nanoclusters, the shorter peak emission wavelength indicates that the crystals/clusters are smaller than after a one hour anneal.

Using only one nitride layer in the stack either before or after the SiO_x layer, results in PL that is comparable to the PL from the SiO_x layer alone. This indicates that hydrogen can readily be lost from the sample at high temperatures unless it is contained by the nitride layers.

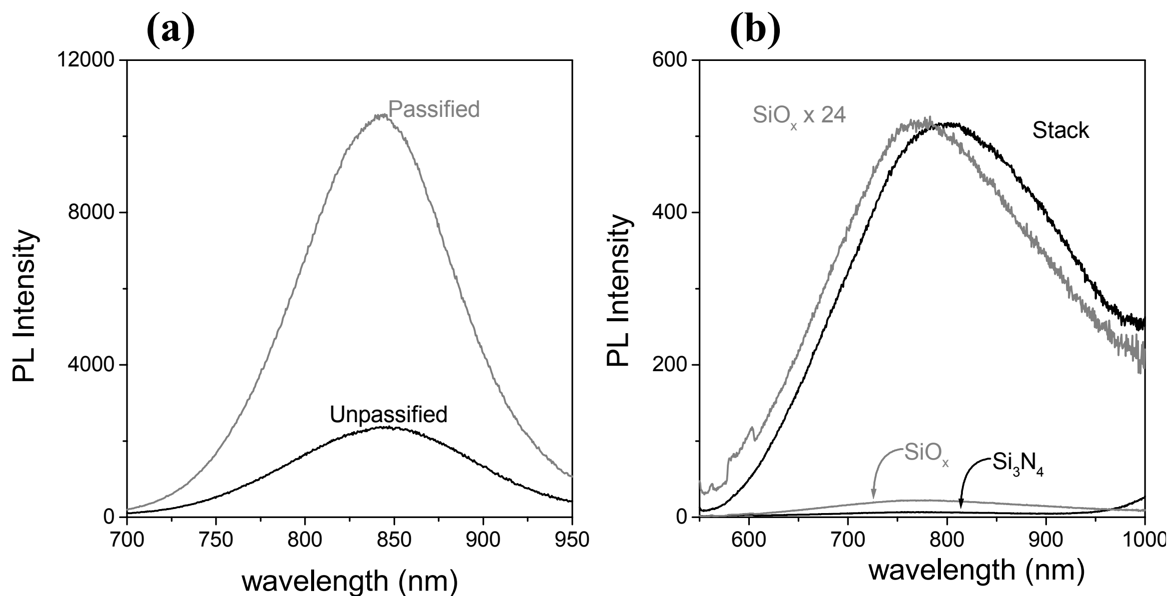

Figure 4.15 (a) PL spectra of stack containing Si nanocrystals annealed for 1 hour at 1100°C in N_2 before and after a nitride passivation anneal. (b) PL spectra of the SiO_x layer, the silicon nitride and the nitride-SiOx-nitride stack annealed for 15s at 1000 °C.

4.4.e Effect of impurities

The effect of small amounts of metal impurities on the PL of silicon nanocrystals has been investigated. Cu, Fe and Au are known to cause a considerable reduction in the carrier recombination lifetime in bulk silicon[63, 64]. These metals are common impurities that may deteriorate the performance of electronic devices. Less is known about their effect on carriers in nanocrystalline silicon. The band structure, which plays an important role in determining the lifetime of the carriers, is different for the nanocrystals than for bulk silicon. Additionally, it is not known if the implanted metals will be incorporated into the nanocrystals or diffuse into the oxide. To determine the effect of metal impurities, silicon-rich oxides where implanted with impurity ions of iron, copper or gold

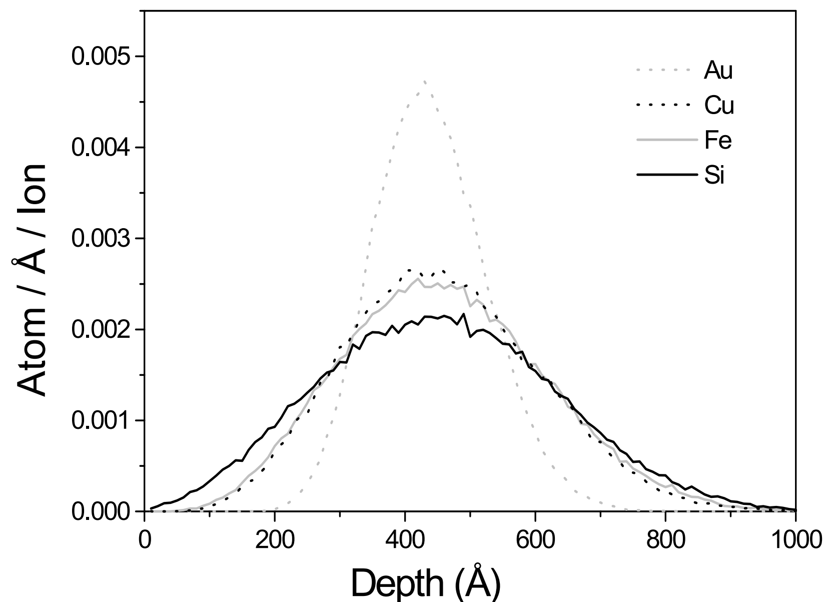

Figure 4.16 TRIM predictions of the ion implantation profiles of 100keV gold, 55keV iron, 60 keV copper and 30keV silicon ions into SiO_2.

Silicon nanocrystals were produced by ion implantation of 30keV Si ions to a fluence of 3.4×10^{16} Si/cm^2 into a 1μm thick thermally grown SiO_2 layer on a silicon substrate. This was then followed by implantation of 0, 10^{13}, 5×10^{13} or 10^{14} ions/cm^2 of either 100keV Au,

55keV Fe or 60keV Cu. A dose of 10^{14} ions/cm^2 corresponds to about 6 impurity ions per nanocrystal (based on the number of implanted silicon ions and a nanocrystal diameter of 4.3nm). All implants were simulated using TRIM[65] and the energies were chosen so that the implantation range was approximately the same for all ions species. The predicted implantation profiles are shown in Figure 4.16. Annealing the samples in N_2 at 1100°C for one hour then formed the nanocrystals.

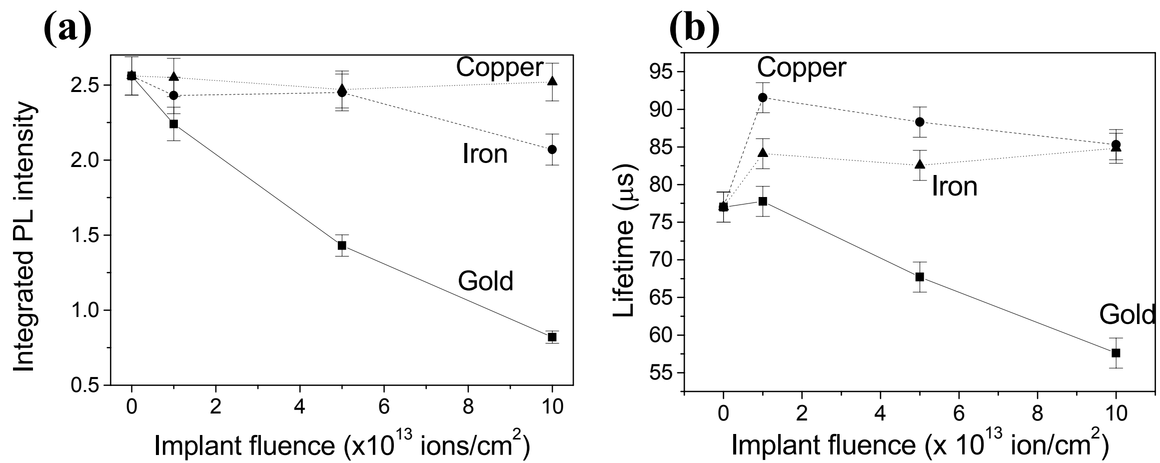

Figure 4.17 (a) Integrated PL intensity and (b) Lifetime of PL as a function of implant fluence of gold(■), iron(●) and copper(▲).

Figure 4.17(a) shows the integrated PL intensity of the samples as a function of the impurity dose. The integrated PL intensity from the sample implanted with gold is reduced with increasing impurity concentration. The implantation of 10^{14} Au ions/cm^2 reduces the PL by 70%. Iron implanted to a similar fluence caused a small reduction (25%) while copper produced no detectable change in intensity. The reduction in PL intensity is likely due to the formation of impurity-based recombination centres, reducing the number of luminescing nanocrystals.

The lifetime of the PL follows a similar trend to that of the PL intensity. Figure 4.17(b) shows the variation of the lifetime as a function of the impurity concentration. The sample without impurities has a lifetime of about 77μs. For Au and Fe, any further increase in

impurity dose caused a decrease in the lifetime reducing it to as little as 58μs for the sample with the highest level of gold. In the low-pump regime, as is the case in this study, the variation in the PL intensity and lifetime can be used to determine the number of luminescing nanocrystals[66] according to Equation 4.1, where I_{PL} is the PL intensity, σ is the excitation cross section of a nanocrystal, ϕ is the photon flux, N is the number of luminescing nanocrystals and τ and τ_R are the measured lifetime and the radiative lifetime of the nanocrystals. The samples implanted with 10^{14} Au ions/cm^2 has approximately 42% the number of luminescing nanocrystals than the unimplanted sample, while the presence of iron reduced the number of luminescing nanocrystals to ~68%.

$$I_{PL} \propto \sigma \phi N\tau/\tau_R \qquad \textbf{Equation 4.1}$$

The distribution of the impurity ions was measured after the initial deposition and after the 1100°C anneal. RBS measurements using 2MeV He ions, showed that the impurity distributions before annealing were consistent with TRIM predictions. After annealing, there was no significant change in the distribution of the Au and Fe atoms. However, the concentration of Cu atoms dropped below detectable levels as shown in Figure 4.18. The lack of any significant effect from the copper implant is therefore likely due to the fact that it has diffused out of the nanocrystal layer.

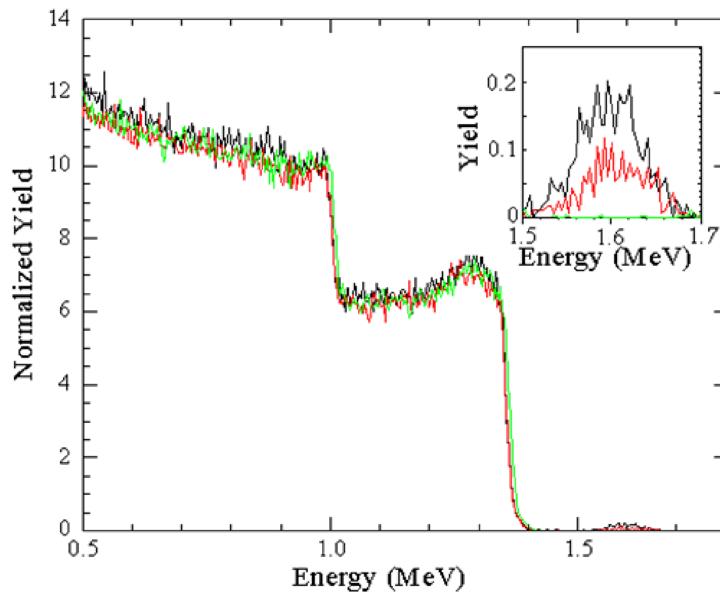

Figure 4.18 RBS spectra of thermal SiO_2 implanted with silicon and copper. The black and red curves represent the data for samples with 10^{15} and $5x10^{14}$ Cu ions/cm^2 as-implanted. The green curve represents the sample implanted with 10^{15} Cu ions/cm^2 after a one hour anneal at 1100°C. The insert shows the contribution of the copper ions to the RBS spectra.

4.5 Summary & Conclusions

PECVD deposited SiO_2 layers show no PL under the present measurement conditions. In contrast, SiO_x layers show increasing PL intensity with increasing annealing temperature. As-deposited silicon nitride layers show PL emission which increases with increasing temperature up to ~400°C. The emission then decreases during annealing at higher temperatures. These trends play an important role in understanding the behaviour of microcavity structures that contain such layers.

- PECVD deposited silicon-rich oxide layers can be used to produce luminescent Si nanocrystals with a mean diameter of around 4-5nm.
- Optimal emission was achieved for silicon-rich oxide layers having a silicon concentration of ~40%.

- Passivation of non-radiative defects with hydrogen can be achieved by annealing in forming gas or by exploiting the hydrogen trapped in associated silicon nitride layers. This has important implications for microcavity structures and can increase the nanocrystal luminescence intensity by as much as 20-25 times.
- Both the thickness and the index of refraction of the SiO_x and silicon nitride films change considerably during annealing and such effects must be taken into account when modelling such structures.
- PECVD deposited silicon-rich oxides and nitrides contain about 25% hydrogen when deposited. This is released during subsequent annealing at temperatures above about 400^oC.
- The presence of low levels of Fe and Au impurities during the formation of silicon nanocrystals reduces the PL emission from silicon nanocrystals.

Chapter 5 Microcavities

The aim of this chapter is to explore the effect of microcavity structures on the PL of silicon nanocrystals. The microcavity effect will be used to enhance the emission for a narrow band of wavelengths, transforming the broad-band emission of the nanocrystals into delta-function-like spectra. The light emitted by the nanocrystals can be significantly modified by placing them between two partially reflecting mirrors. The light emitted goes through multiple internal reflections and at each reflection, some light is emitted. The wavelength corresponding to constructive (or destructive) interference will depend on the distance between the mirrors.

5.1 Single layers

5.1.a Single layers of PECVD SiO_x

Single layers can act as a microcavity, with the film/substrate and film/air interfaces acting as partially reflecting mirrors. The resulting modification of the emission spectrum can be unintentional making it difficult to compare the spectra from different samples. The shape of PL spectra can be used to deduce parameters such as the average nanocrystal size[67]. However, for this analysis to be accurate, the modification of the spectrum needs to be taken into account.

The effect of the thickness of the PECVD SiO_x layers on its PL was studied up to a thickness of 1.1μm. The samples were deposited by PECVD then annealed at 1100°C in N_2 for one hour. Figure 5.1 shows the measured PL spectra of these samples. If the PL

depended only on the emission from the nanocrystals, then all spectra in Figure 5.1 would have the same shape with their height proportional to the sample thickness (because the thicker samples contain more nanocrystals). However, we see significant differences between samples. These differences are due to variations in the extraction efficiency with wavelength and film thickness.

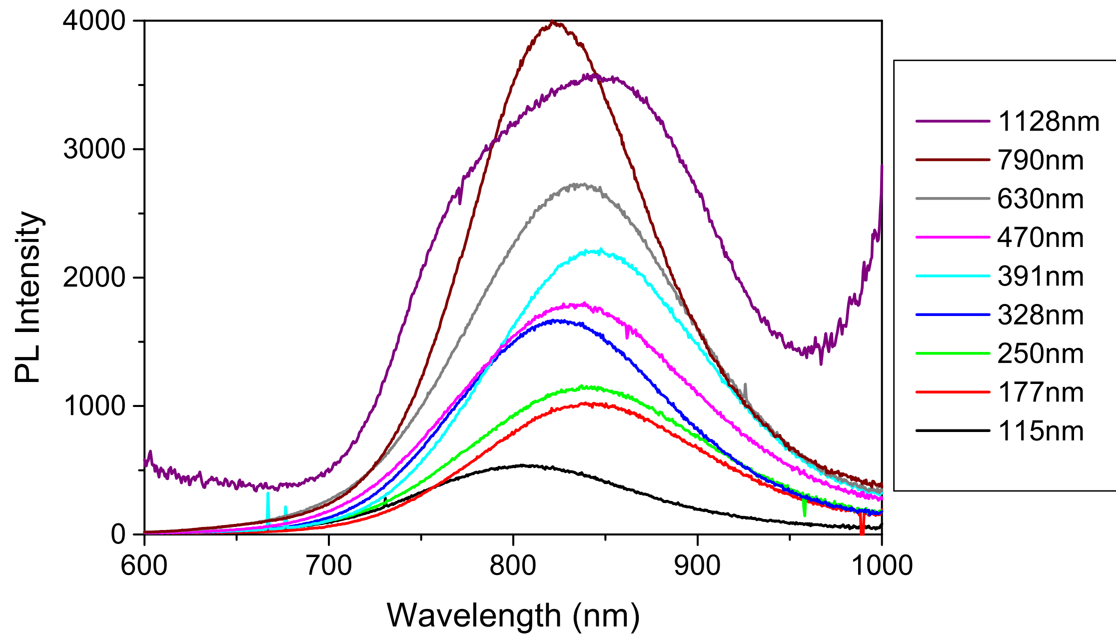

Figure 5.1 PL spectra of samples with various SiO_x thicknesses after a one hour anneal at 1100°C.

As described in chapter 2, to simulate the effect of a microcavity on the PL spectra it is necessary to calculate the reflection coefficient of the two mirrors and electric field distribution in the structure. The reflectivity of the mirrors and their spacing determines the extraction efficiency, whilst the amount of light produced at a given position is proportional to the square of the electric field strength at that point. Taking these factors into account it is possible to predict the effect of the sample structure on the PL.

The results of such simulations are shown in Figure 5.2. The model can accurately predict the shape and position of the peaks but does not accurately reproduce the peak intensity, which depends on many factors including absorption. The predicted spectra were normalised to have the same peak height as the measured data. With the exception of the thinnest sample (115nm), the model adequately reproduces the measured PL spectra, including the 1128nm sample which produces a highly distorted spectrum.

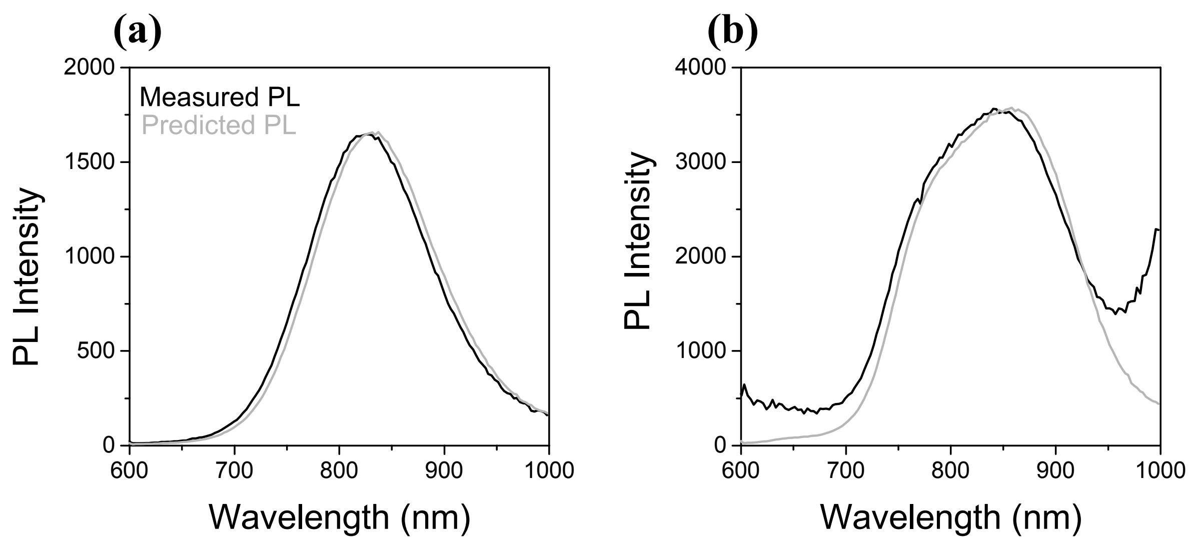

Figure 5.2 Measured and predicted shape of the PL spectra for SiO_x layers of different thickness. The thicknesses of the layer are (a) 328nm and (b) 1128nm.

5.1.b Ion implanted samples

The effect of the sample thickness was studied for thicker samples using silicon implanted into thermally grown SiO_2 layers. In all cases, a dose of 2.5×10^{16} ions/cm^2 30keV silicon ions was implanted into the thermal oxide. The only difference between these samples is the thickness of the SiO_2 layer, which varied from 100nm to 10μm. If there were no effect of the sample structure on the emission, one would expect similar spectra from all samples. However, Figure 5.3 shows that there is a significant difference in the measured spectra.

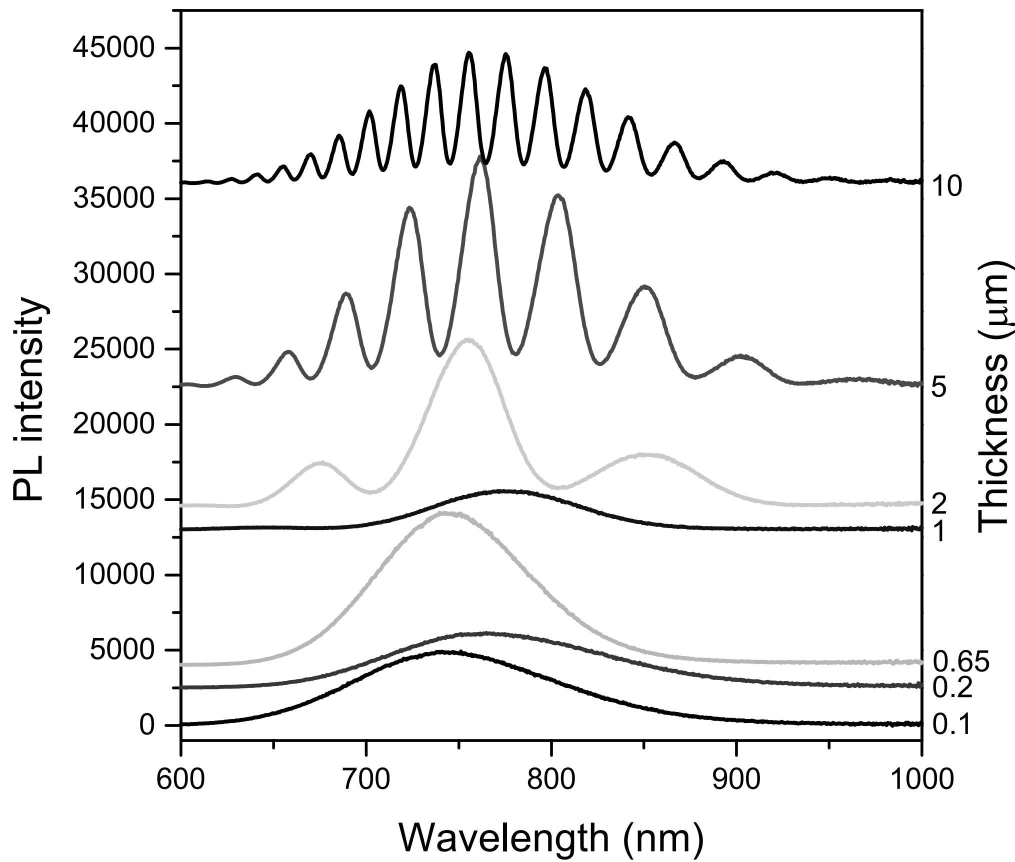

Figure 5.3 PL spectra from Si nanocrystals in SiO_2 layers of various thicknesses. The spectra have been offset vertically for clarity. The thickness of the film is indicated on the right axis.

To measure the PL without the structural effect modifying the measurement, the extraction factor and reflectivity of the sample must not vary significantly over the emission wavelengths. Samples should either be less than one quarter of the emission wavelength or greater than 100 times the emission wavelength. In contrast to the PECVD samples, where the change in shape consisted of variations in peak position and FWHM of the peak, these samples have multiple peaks. In the case of the 10µm samples, the broad spectrum is transformed into a series of over 15 peaks.

There is a strong correlation between the reflectivity of the samples and the PL. At wavelengths emitted by the nanocrystals, when the reflectivity of the sample is a minimum, the PL is at its maximum.

The same model used to simulate the PL from the PECVD samples was also applied to these structures. The main difference between the models is that in this case, the light source was not evenly distributed throughout the SiO_x layer but was assumed to originate from the centre of the implanted region. This was estimated to be at a depth of 55nm by SRIM[65] simulations. The shape of the PL spectrum of the nanocrystals before modification by the structure was estimated to be the same shape as that of an ion implanted fused silica sample of 1 mm thickness.

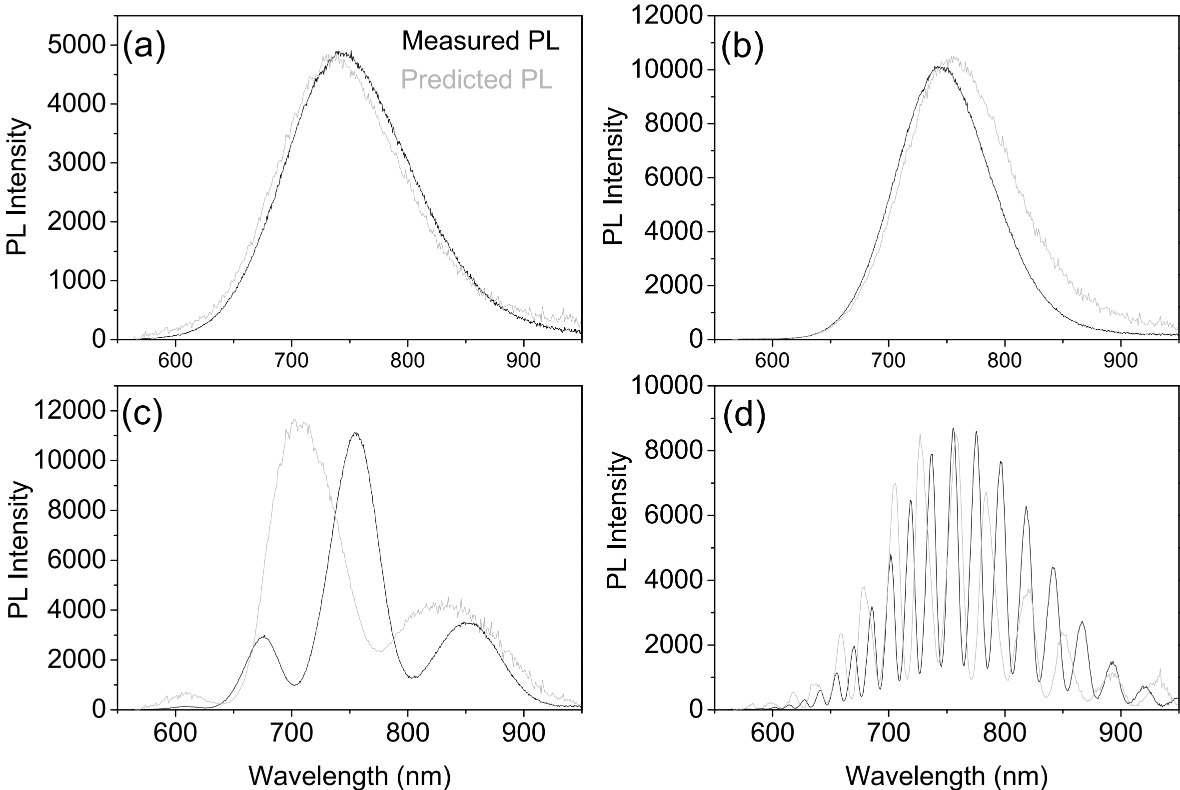

Figure 5.4 Measured and simulated PL spectra of silicon nanocrystals in thermal oxide on a silicon substrate. The thickness of the thermal oxide was (a) 110nm, (b) 660nm, (c) 2μm and (d) 10μm.

Figure 5.4 shows that this model can correctly predict the resulting structure. It also correctly predicts the relative intensity of the maxima and minima. However, in this case the model does not accurately reproduce the peak positions or, in some cases, the peak widths. The main reason for this is that the variation of the index of refraction of the implanted region was not included in the model.

5.2 Silicon Dioxide / Silicon Nitride cavities

5.2.a PL from cavity

The structural effects are more pronounced when the reflectivity of the two mirrors is increased. This can be achieved by increasing the contrast in the index of refraction or by using distributed Bragg reflectors. In this case, a microcavity was produced with a bottom DBR made from 8 alternating layers of SiO_2 and silicon nitride, an active region of SiO_x and a 5 layer top mirror. A SEM image of the structure is shown in Figure 5.5. Although the structure would have better optical properties if a nitride layer was the first layer deposited, the layers are mechanically more stable if a SiO_2 layer is deposited first[68]. The samples were annealed at 1100 °C to form the nanocrystals in the SiO_x region.

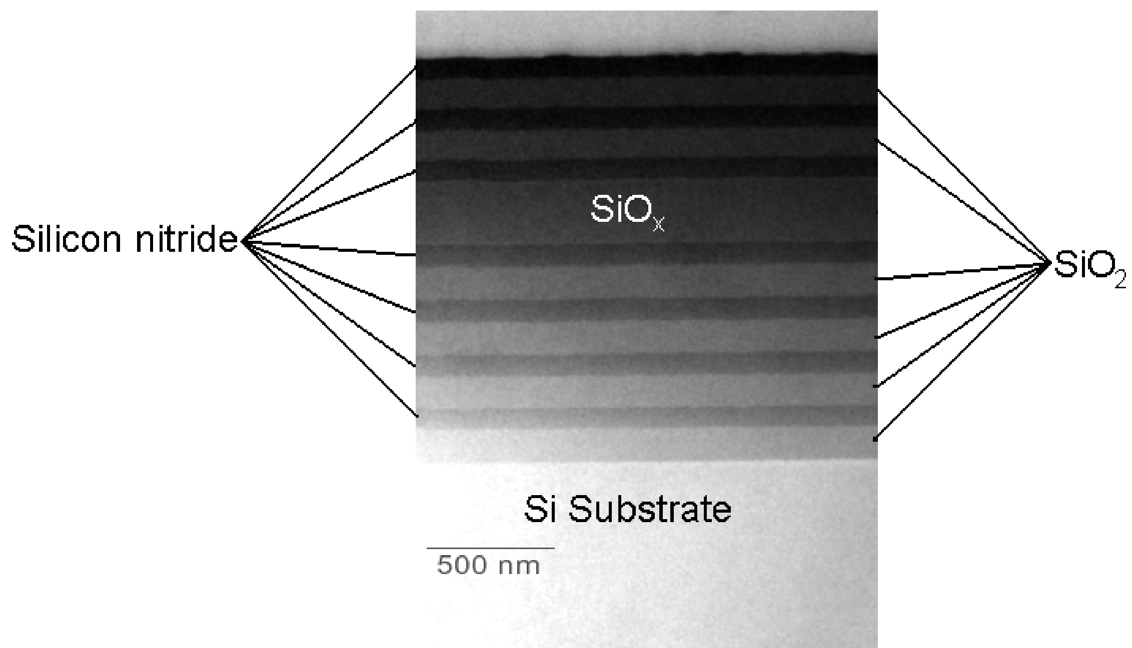

Figure 5.5 SEM image of the SiO_2/nitride microcavity.

The reflectivity of the microcavity structure is shown in Figure 5.6. For SiO_2/nitride based distributed Bragg reflectors, it is possible to have high reflectivities for wavelengths corresponding to the entire nanocrystal emission spectrum (from 650nm to 950 nm). The dip in the reflectivity spectrum caused by the $\lambda/2$ SiO_x layer corresponds to the cavity's resonant wavelength. For this particular cavity, the resonant wavelength is 777nm. The FWHM of this dip is 17nm, giving the cavity Q-factor of ~47.

The PL of the microcavity structure is compared to that of a SiO_x layer that was annealed under identical conditions in Figure 5.7. The PL spectrum is much narrower than that of the silicon-rich layer, about 20 times more intense at its peak emission wavelength (778nm), and with 2.7 times stronger integrated PL intensity than the nanocrystal layer.

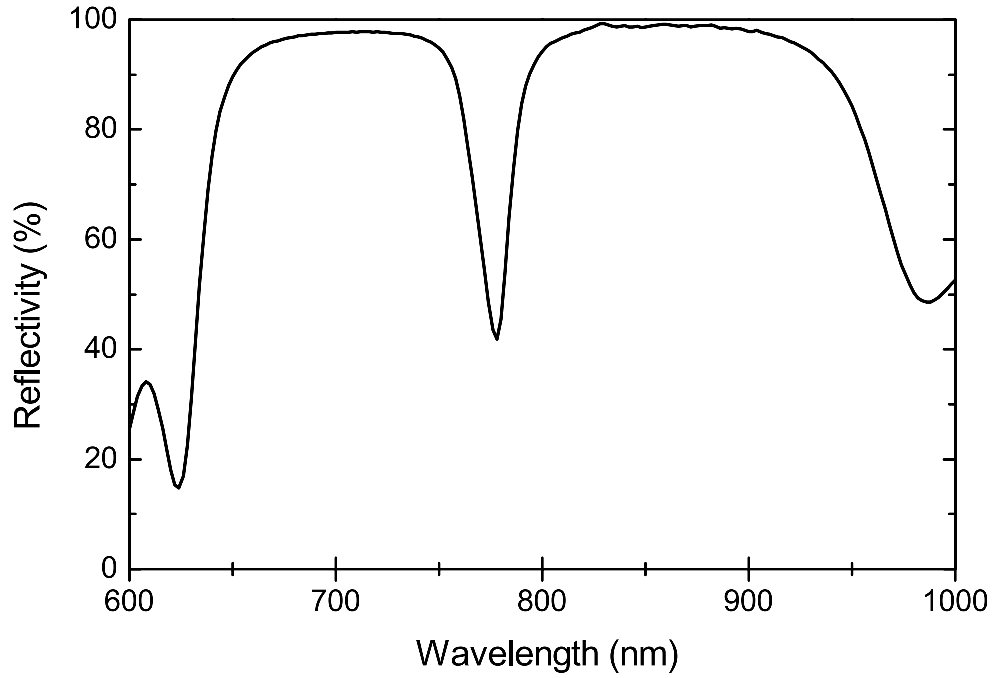

Figure 5.6 Reflectivity spectrum of the SiO_2/nitride microcavity.

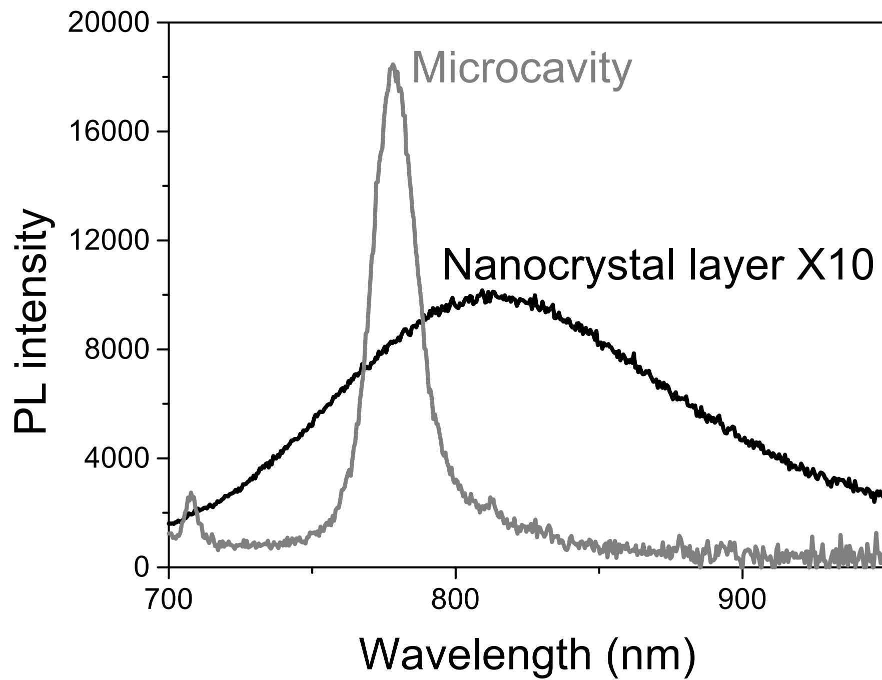

Figure 5.7 PL spectra of a microcavity structure compared to the active layer. Both samples were annealed for 1h in N_2 at 1100°C.

5.2.b Angular dependence of emission

The reflectivity of distributed Bragg reflectors varies considerably according to angle. In addition to this, the resonant wavelength of the cavity also varies with angle. This effect was measured and Figures 5.8 and 5.9 show the angular dependence of the PL from the microcavity structure.

As the angle increases, the peak emission wavelength decreases. The shift in the peak emission wavelength is consistent with the expected shift in the resonant wavelength of the cavity with varying angles[5].

$$\lambda = \lambda_o \cos\left(\arcsin\left(\frac{1}{n_{eff}}\sin\theta\right)\right) \qquad \textbf{Equation 5.1}$$

where λ_o is the resonant wavelength for normal emission. An effective index of refraction (n_{eff}) is used because the mirrors are DBRs instead of planar mirrors. The effective index of refraction was used as a fitting parameter and was found to be 1.9. For the spectra taken at large angles, the reflectivity of the mirrors also varies depending on the polarisation of the light. Each polarisation has a slightly different resonant wavelength and this is responsible for the double peaks in the spectra of Figure 5.9 for emission angles greater than 45°. It was confirmed that each peak has a different polarisation by using a polariser. The emission from the microcavity is predominantly in the forward direction and as the angle increases, the intensity of the PL is reduced. This can be seen more clearly in Figure 5.10 which shows the integrated PL intensity of the microcavity sample with emission angle. The PL was integrated over the measured wavelength range and then divided by $\cos(\theta)$ to correct for the change in area seen as the sample is tilted.

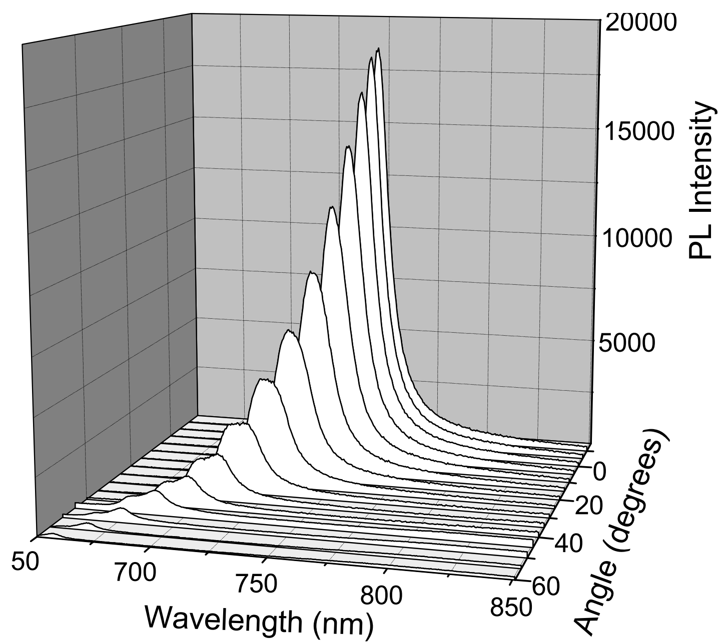

Figure 5.8 The emitted PL spectra at various angles. The spectrum with the highest intensity was taken at normal emission. The angle between subsequent spectra is 5°.

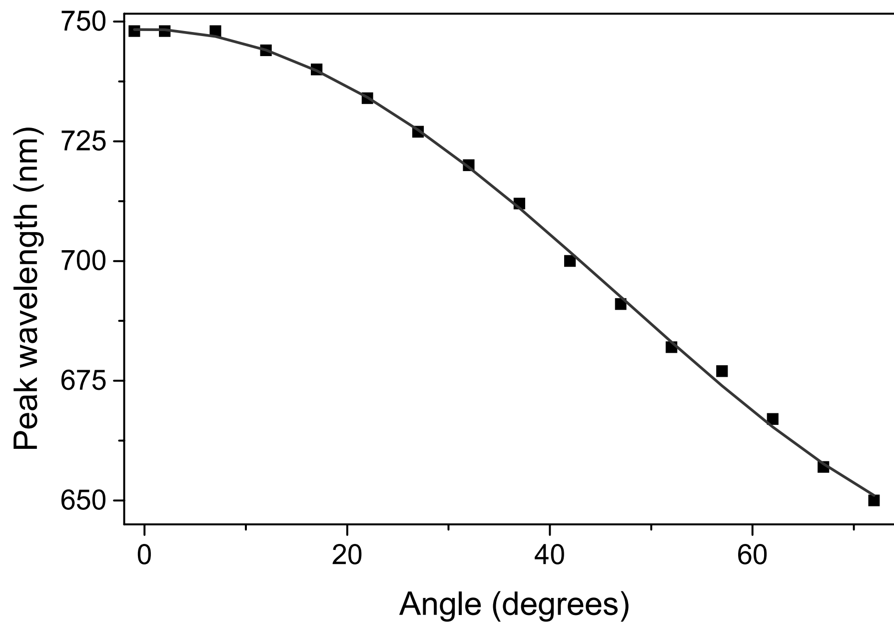

Figure 5.9 The peak emission wavelength as a function of angle with respect to the sample normal. The line represents a fit to the data using Equation 5.1.

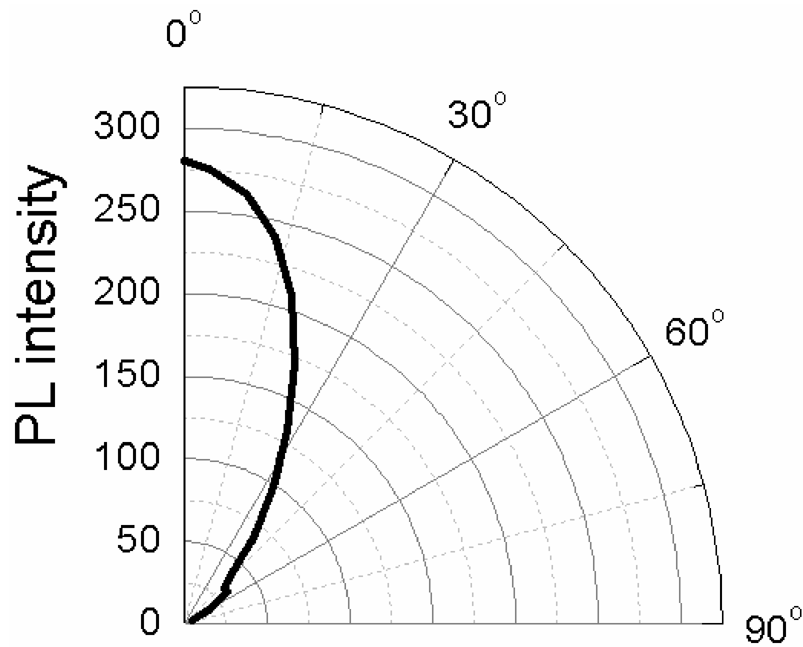

Figure 5.10 Polar plot of the integrated PL intensity of a microcavity as a function of angle.

5.2.c Effect of layer thickness

To determine the wavelength range in which a microcavity is capable of enhancing the emission from the silicon nanocrystals, a series of microcavities was formed by systematically varying the thickness of all layers. The resonant wavelength of the cavity is proportional to the thickness of the layers. The resulting PL spectra from these structures are shown in Figure 5.11. These measurements show that it is possible to design a cavity to obtain a single resonant wavelength from 730 to 920 nm. It is interesting to note that the microcavity with the strongest PL is that which has a resonant wavelength at 830 nm. This corresponds, as expected, to the peak-emission wavelength of the nanocrystal spectrum.

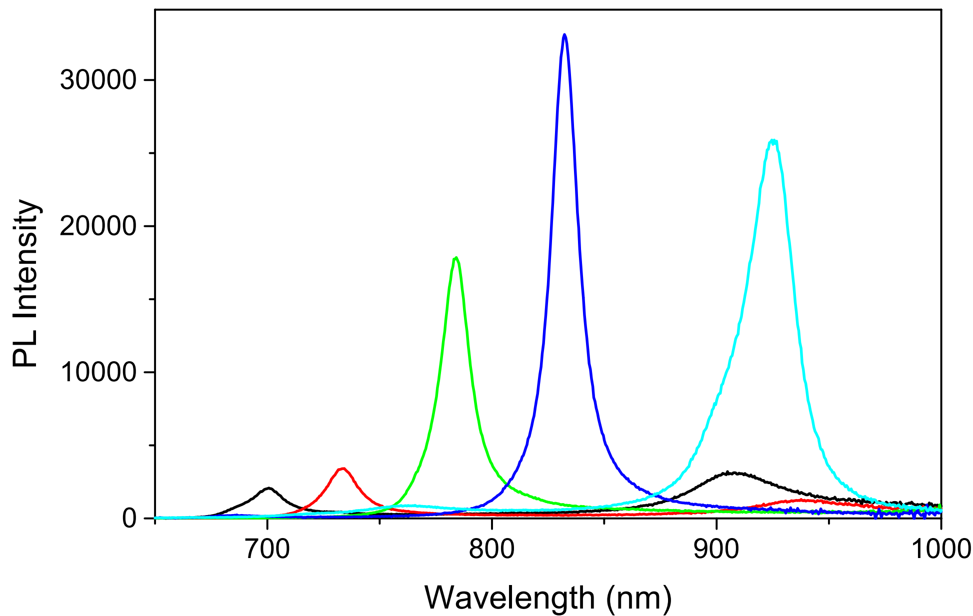

Figure 5.11 PL spectra of five microcavities with different resonant wavelengths.

5.2.d Effect of number of layers

In general, the emission for a microcavity becomes narrower (higher Q-factor) the higher the reflectivity of the mirrors or the more layers in its distributed Bragg mirrors. Theoretically, an arbitrarily sharp spectrum can be produced, provided that enough layers are deposited. However, this may come at the expense of the absolute intensity, because the increased reflectivity of the top mirror limits transmission. This section explores the limit to which the spectrum of silicon nanocrystal can be narrowed by the microcavities.

The simulations described in chapter 2 predict that for a given number of layers, a symmetric cavity with the same number of layers in both top and bottom mirrors will emit with the narrowest spectral distribution. Microcavity structures with 6, 8, 10 and 12 layers of silicon dioxide and silicon nitride in each of the DBR were produced. Then mesa structures were produced from these samples by lithography and reactive ion etching.

The results of PL measurements on these samples are shown in Figure 5.12 and summarised in Table 5.1. As the number of layers increases, the line width of the peak is reduced. The measured line width is about 2nm larger than expected from simulations, an effect that is largely attributed to surface roughness of the films. The luminescence intensity decreases with the number of layers. This may be due to stress induced defects in the microcavity. The microcavity with more layers had a larger density of cracks. In the case of the microcavity with 12 layers per mirror, only a very small region of the sample was defect free. PL was only taken from the defect free region, and the PL intensity is lower because it was taken over a smaller area.

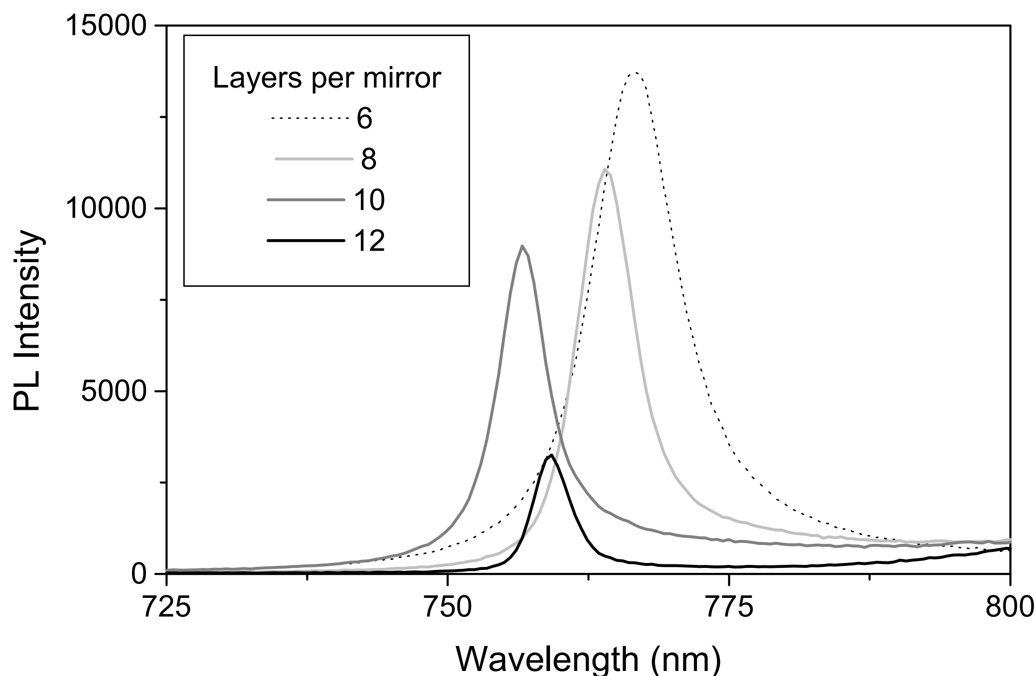

Figure 5.12 PL spectra of microcavities with 6, 8, 10 and 12 layers in each of the distributed Bragg mirrors.

Number of layers in each mirror	Q-Factor	FWHM (nm)	simulated FWHM (nm)
6	80	9.5	7
8	121	6.3	3
10	143	5.3	2
12	205	3.7	2

Table 5.1 Comparison of the experimental and simulated FWHM of the microcavity structures with various number of layers in their distributed Bragg mirrors.

5.3 Effect of annealing microcavities

In order to determine the optimal anneal time required to get maximum PL intensity, a series of isothermal and isochronal anneals were performed on the microcavity structures. To determine the origin of the PL, the anneals were also performed on a 255nm thick SiO_x layer and a 90nm nitride layer and on a microcavity structure where the SiO_x layer was replaced by a SiO_2 layer (as shown in Figure 5.13). For the isothermal anneals, an anneal temperature of 1000°C was chosen so that anneal times from 10s to 15h could be compared (see Figure 5.14).

The PL of the SiO_x layer increased slowly with time. However the PL of the microcavity with the SiO_x layer increased very quickly reaching its maximum value after less than 30s. The large increase in PL is attributed to excellent passivation of the nanoclusters/nanocrystals in the SiO_x layer as described in (section 4.4.d). The reduction in PL for longer anneal times may be due to loss of hydrogen (and in the quality of passivation).

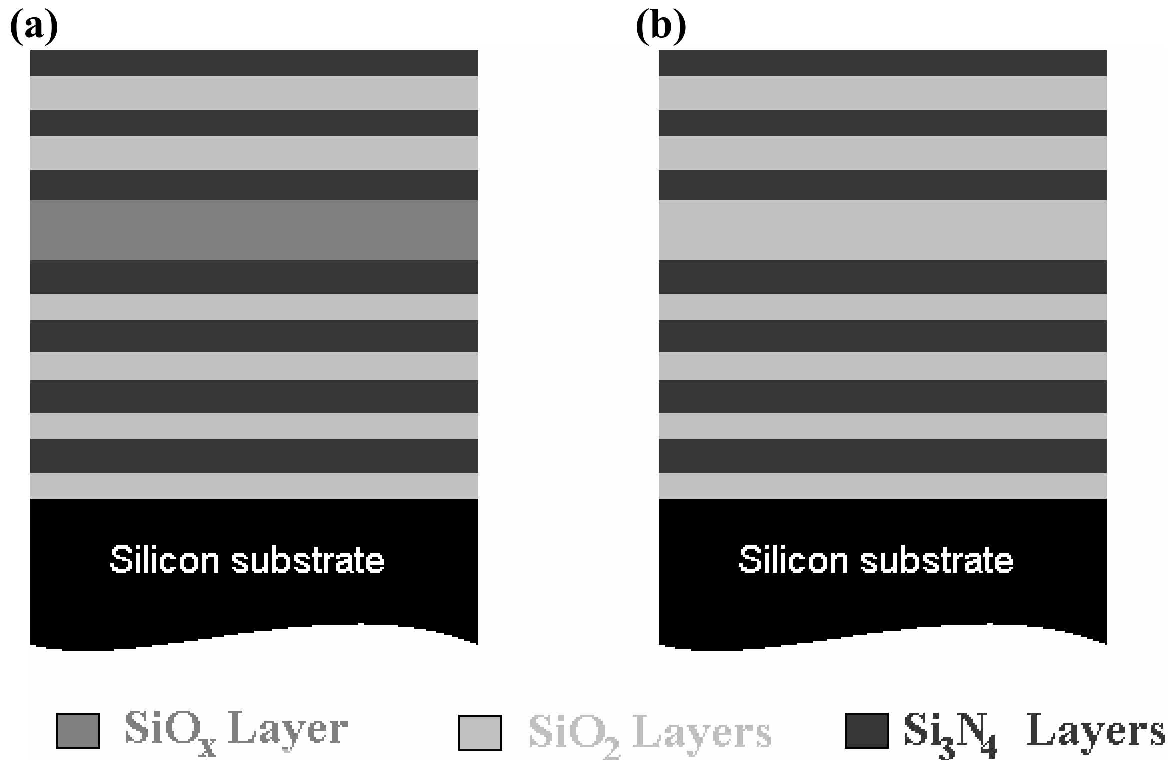

Figure 5.13 Schematic of (a) the typical SiO_2/Si_3N_4 microcavity structure with a SiO_x cavity layer and (b) the microcavity structure with SiO_2 in the cavity layer.

The PL from the microcavity without any SiO_x, only shows a reduction in PL as it was annealed. This reduction is very similar to that of the PL from the microcavity structure with the SiO_x layer. It is known that defects in nanocrystals in silicon nitride are also passivated by hydrogen. Therefore the loss of hydrogen would cause a reduction in the quality of passivation for both microcavity structures and lead to lower PL as the samples are annealed.

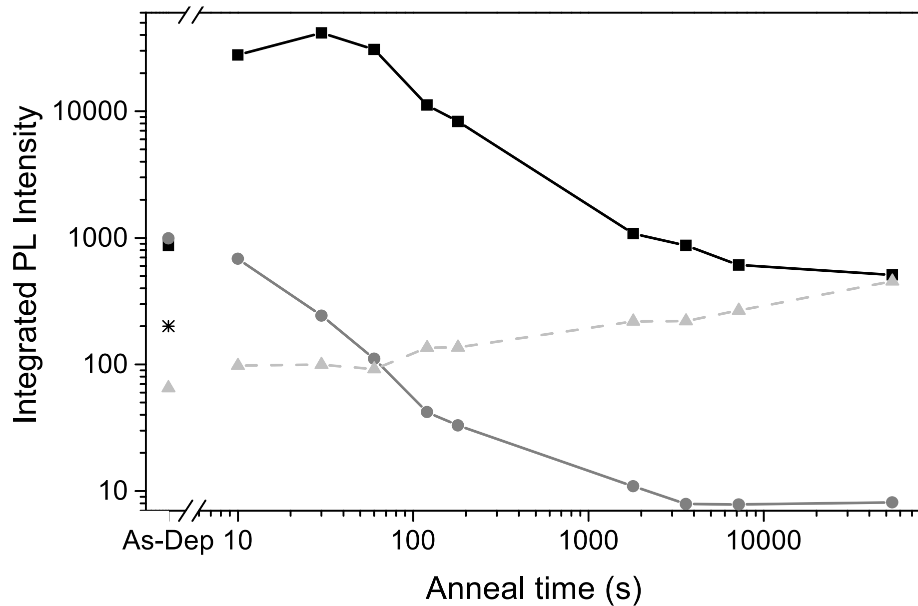

Figure 5.14 Integrated PL intensity as a function of anneal time for a 255nm SiO_x layer (▲), a 90nm nitride layer multiplied by seven to account for the multiple nitride layers(*) a microcavity structure with (■) and without (●) excess silicon in the microcavity. The anneals were performed at 1000°C in N_2 in either a rapid thermal annealer (for anneal times of three minutes or less), or a tube furnace (for anneal times of 30 minutes or more).

Figure 5.15 shows the evolution of the PL of the structures and layers as the anneal temperature is increased. With an anneal at 400°C, the PL of the structures increases because of the increased PL from the silicon nitride layers.

As the nitride layers are annealed at temperatures greater than 400°C, there is a reduction in the PL intensity. This reduction is attributed to the loss of hydrogen in the nitride layers[56]. The PL of the cavity without SiO_x continues to increase until about 550°C. The increased temperature required to cause a reduction in PL from the microcavity, is likely due to the greater thickness of nitride reducing the loss of hydrogen, as observed by McCann et al.[69]. For anneal temperatures greater than 900°C, the emission from the SiO_x layer becomes significant, dominating the emission from the microcavity structure.

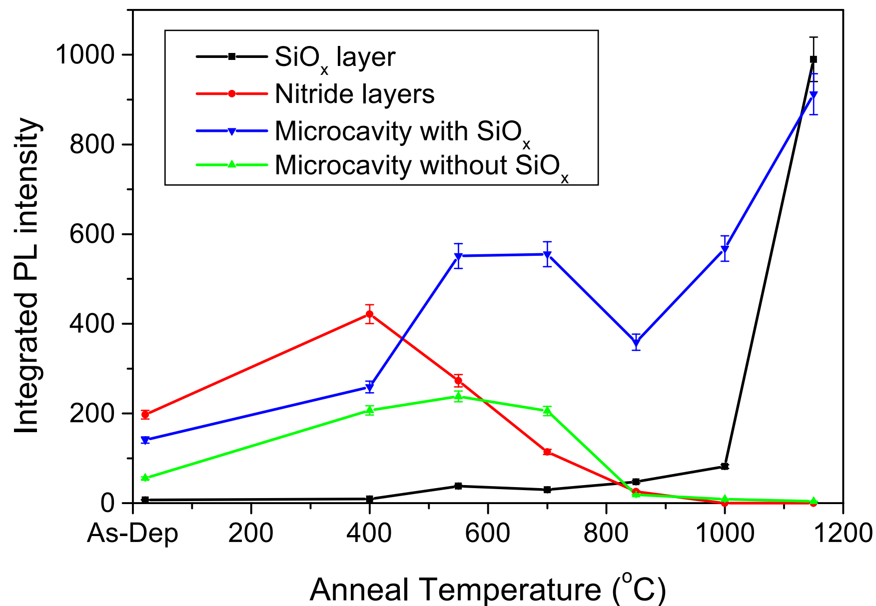

Figure 5.15 Integrated PL intensity of the microcavities, SiO_x layers and a microcavity without nanocrystals after isothermal anneals at 400°C to 1100°C for 1 hour in N_2. The nitride plot was multiplied by seven to account for the multiple nitride layers.

5.3.b Anomalously strong PL

Figure 5.16 shows the enhancement of the PL intensity that is achievable when a nanocrystal layer is embedded in a SiO_2/nitride microcavity. Remarkably, the strongest luminescence was found to occur after annealing for only 15 s at 1000°C. The PL from this structure is more than 15000 times more intense than the emission from a silicon rich layer under the same annealing conditions. This is inconsistent with the trends observed for light emission from the silicon nanocrystals, which increases with increasing anneal times (see section 4.4.b), and strongly suggests that there is another mechanism enhancing the PL in these microcavity structures.

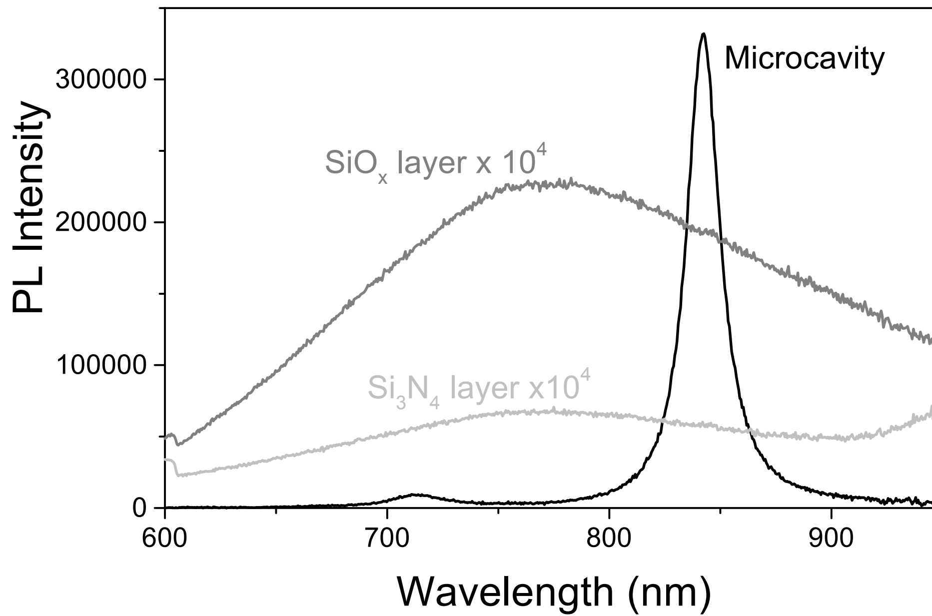

Figure 5.16 PL spectra from a microcavity structure, a 230nm SiO_x layer and a 100nm nitride layer annealed for 15s at 1000 °C.

The PL from the nitride layers is weak but after a 15s anneal is comparable to that of the SiO_x as shown in Figure 5.16. If we add the contribution of the seven Si_3N_4 layers to that of the SiO_x layer, the total is only 1/6000th of the intensity of the microcavity structure. The expected enhancement due to the microcavity structure is only a factor of 20 to 50.

The very strong PL from the microcavity cannot be explained by the PL emitted by either the SiO_x layer or the nitride layers. This suggests that there is something else responsible for the enhancement of the PL from the microcavity. Indeed, the reason that the emission is so strong after short anneal times is that the silicon nanocrystals in the SiO_x layer are passivated very efficiently by hydrogen when there are nitride layers on either side of it. The nitride layers provide hydrogen and act as a diffusion barrier preventing its release (see section 4.4.d). In the case of a SiO_x layer with a nitride layer on each side, there is a 25 times enhancement in the PL emission of the layers due to the excellent passivation of the nanocrystals this provides. In the case of the microcavity, the enhancement may be greater

due to the additional nitride layers which provided a larger amount of hydrogen and also prevented the released of the hydrogen

5.4 Passivation of microcavities

Passivation of silicon nanocrystals embedded within microcavity structures is difficult because of the low hydrogen diffusion coefficient in silicon nitride[60]. The optimal passivation anneal for SiO_x layers of 1h at 500°C in 5% H_2 in N_2, does not produce any measurable change in the PL of microcavities. However, there is a large amount of hydrogen present in the as-deposited nitride layers, which can be used to passivate the nanocrystals.

5.4.a Hydrogenated silicon nitride passivation

To use hydrogenated silicon nitride to pacify the nanocrystals within the microcavity, it is necessary to deposit the microcavity in two steps. This is because the thermal treatment required to form silicon nanocrystals (typically 1100°C for 1 hr) is sufficient to drive out all the hydrogen from the entire structure. The bottom mirror as well as the silicon-rich layer must be deposited before the 1 hour anneal required to form the nanocrystals. After this anneal, the top mirror is deposited, then the whole structure can be annealed at 1000°C for 15s to release the hydrogen from the top mirror and passivate the nanocrystals. Figure 5.17 shows that after the top mirror is deposited onto the annealed bottom mirror and active layer, the PL of the structure is comparable to that of a microcavity deposited in one step, followed by a one hour anneal. This is as expected because these two structures contain the same amount of silicon-rich oxide annealed under identical conditions (1h at 1100°C in N_2).

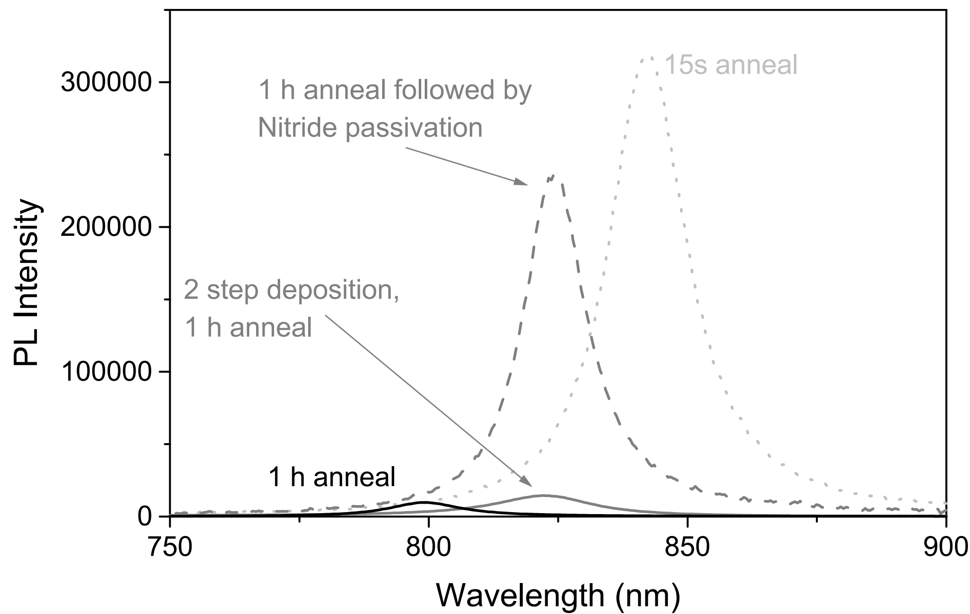

Figure 5.17 PL from microcavity after various thermal treatments. The anneals were done for either 1h at 1100°C or 15s at 1000°C or both.

The effect of the nitride passivation on the microcavity structure is to enhance the PL intensity by a factor of 16. The resonant wavelength of the microcavity does not change despite the different anneal condition employed for the top mirror.

It was expected that once passivated, the emission from the microcavity deposited in two steps would surpass that of the microcavity annealed for only 15s. However the PL intensity of this structure was only 65% of that for the microcavity annealed for 15s. This may be due to the fact that less hydrogen is available for the passivation of defects in the structure deposited in two steps. i.e. the hydrogen was only present in the top mirror before the passivation anneal, while for the cavity annealed for only 15s a high concentration of hydrogen was in both mirrors as well as the silicon-rich oxide.

5.5 SiO_2/SiO_x structures

SiO_x layers also have a high refractive index (~1.8) and can be used with SiO_2 to form Distributed Bragg Reflectors, with the added advantage of increasing the volume of active, light emitting, material. To test this concept, microcavities were fabricated from SiO_2 and SiO_x. With enough layers, it should be possible to make microcavities with mirrors of comparable reflectivity to that of the silicon dioxide/nitride microcavities. Having the multiple SiO_x layers may increase the total light output by having multiple light emitting regions.

The microcavity structure illustrated in Figure 5.18(a) was built by first depositing a distributed Bragg mirror, consisting of a series of 11 layers of alternating SiO_2 and SiO_x layers, each with a nominal optical thickness of 200 nm, onto a silicon substrate An active layer with a nominal optical thickness of 400nm was then deposited followed by a second mirror consisted of another 10 alternating SiO_2 and SiO_x layers.

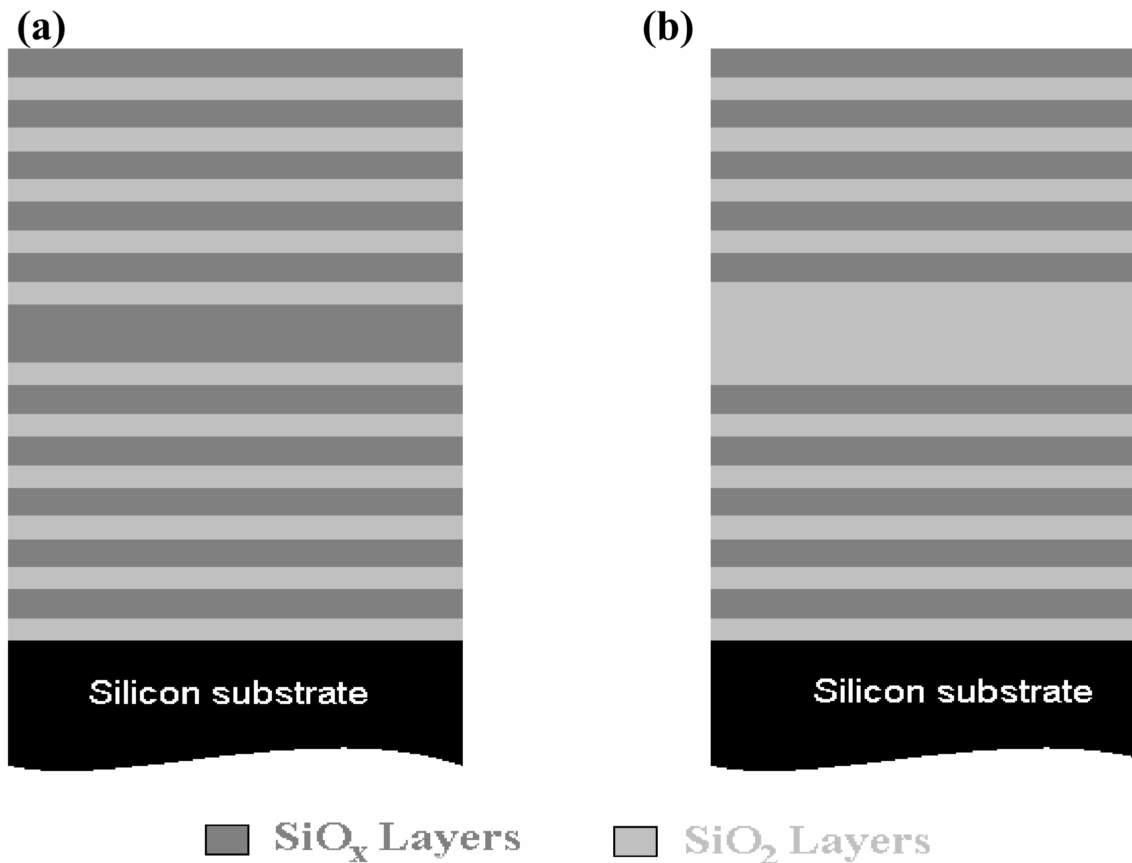

Figure 5.18 Schematic of (a) the SiO_2/SiO_x microcavity structures and (b) the microcavity structure with SiO_2 in the central layer.

The PL of the structure was measured and is compared to its reflectivity in Figure 5.19(a). Compared to the broad emission of the nanocrystal layer seen in chapter 3, the emission from the microcavity shows enhancement and inhibition of PL as a function of wavelength. The maxima and minima of the PL spectra correlate well with the measured reflectivity indicating that it is the sample structure that is responsible for the enhancement at the resonant wavelength.

To determine the role of the cavity layer on the PL, the PL of this structure was compared to a similar microcavity structure where the SiO_x layer was replaced by a SiO_2 layer (see

Figure 5.18 (b)). Replacing the central SiO_x layer with SiO_2, the PL intensity is reduced by 40% (see Figure 5.19). This suggests that the SiO_x in the central layer of the microcavity contributes approximately 40% of the luminescence in this structure.

The light emitted was comparable in intensity to that of a single layer containing the same amount of SiO_x, although the microcavity structure had a lower integrated intensity. Therefore, there is no significant enhancement of the cavity's emission in these SiO_x/SiO_2 structures.

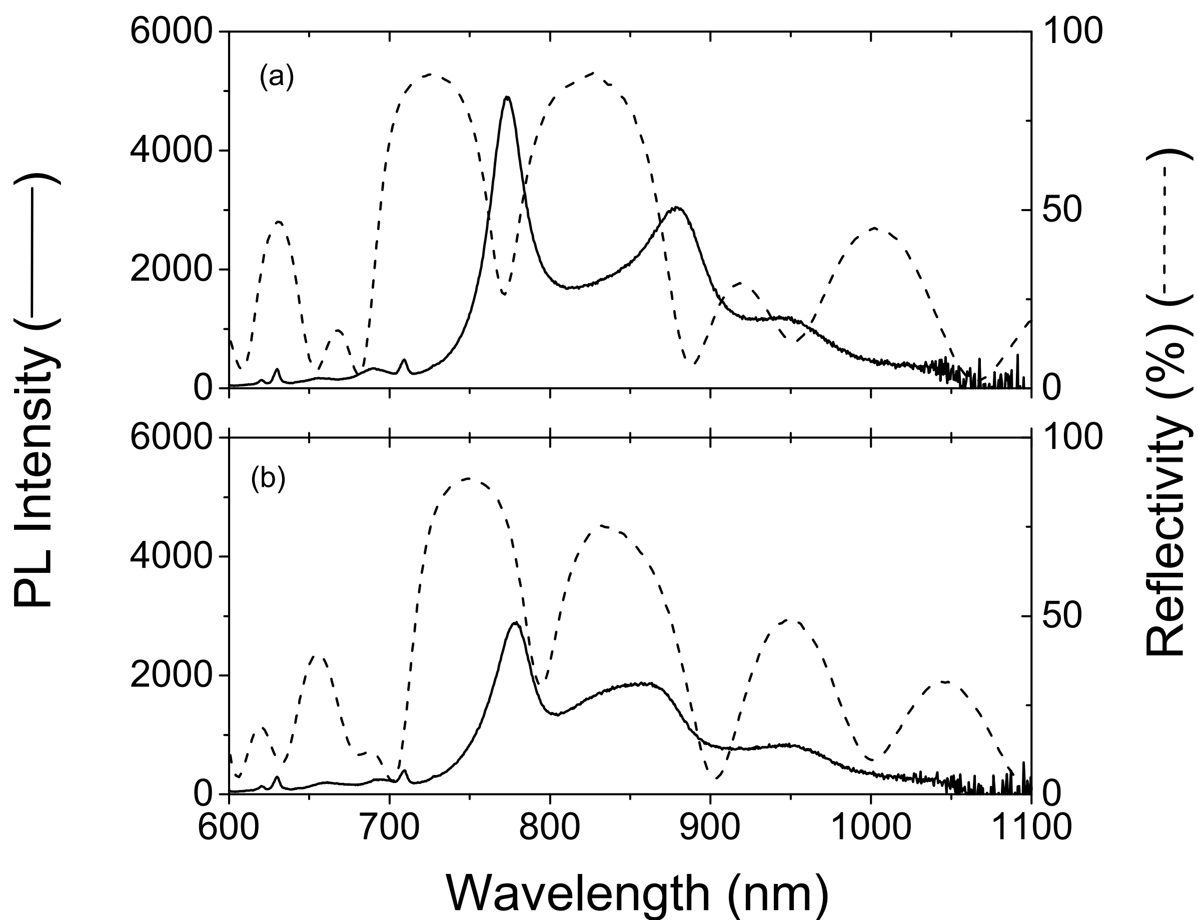

Figure 5.19 PL spectra and reflectivity of a) the microcavity structure, b) the microcavity structure with SiO_2 in the central layer.

Although the PL is considerably enhanced at certain wavelengths, the spectra have multiple peaks with full-width-half-maximum of about 26nm. The reason for the multiple peaks is

that the reflectivity peak of the 2 mirrors is not wide enough to prevent emission of the other supported modes.[70] The width of the peaks is caused by the nanocrystals near the surface which do not have significant optical confinement.

5.6 Summary & Conclusions

- Material structures have a significant effect on measured PL spectra, even for the case of simple single layer structures.
- PECVD deposited SiO_2/silicon nitride layers can be used to form effective microcavity structures for silicon nanocrystals, with effective Q-factors of 50 being achieved.
- Cavities can be designed to emit at any wavelength from 730 to 930 nm and with Q-factors of 30-200.
- The optimal anneal time for the SiO_2/nitride cavities is very short (about 15s at 1000°C) due to the excellent passivation of silicon nanocrystals due to hydrogen release from the silicon nitride layers.
- Alternative structures based on SiO_2/SiO_x mirrors provide a small enhancement in total emission but exhibit poorer optical confinement. .

Chapter 6 Mechanical Properties

Early in this study it was found that some of the films and structures deposited by PECVD failed to survive the various annealing steps required to produce nanocrystals. There were diverse modes of failure depending on the stoichiometry, thickness and thermal history of the film. This chapter starts by describing the types of crack observed in the films (section 6.1) followed by an explanation for their formation (section 6.2). The effect of these cracks on the PL is then discussed in section 6.3. A second type of failure observed was film delamination, is described in section 6.4. Then section 6.5 deals with strategies used to minimise the formation of such defects.

6.1 Nature of cracks

Silicon rich oxide layers deposited onto silicon substrates fail mainly by the development of cracks. It was observed that the crack patterns depend on the crystallographic orientation of the silicon substrate employed for film deposition. To ascertain this dependence, SiO_x films were deposited onto silicon substrates of various orientations ((100), (110) and (111)) and the resulting crack patterns examined. Plan view images of the cracks were taken using optical microscopy and cross sectional images of the cracks were exposed by either mechanical polishing or focused ion beam milling, followed by imaging with scanning electron microscopy.

6.1.a SiO_x films on (100) silicon

Crack patterns in films deposited onto (100) substrates exhibit particularly interesting structure, consisting of straight cracks, and under certain conditions, wavy cracks. This is illustrated in Figure 6.1, which shows the crack pattern in a 1200nm SiOx film deposited on

(100) Si. It can be seen from this figure that for (100) Si substrates, the straight cracks are oriented along the [010] and [001] directions of the substrate. They are perpendicular to each other and at a 45° angle to the cleaved [110] sample edges.

The wavy cracks, on the other hand, propagate along <110> directions, exhibiting two orthogonal sets of cracks parallel to the cleaved <110> sample edges. These cracks have a wavelength of about 100μm and exhibit remarkably regular behaviour, with the wavelength varying less than 5% over distances of several millimetres. Although wavy cracks have been observed in other materials such as rubber[71], glass[72] silicon[73] and in metal layers on silicon[74], they have not been observed in deposited thin films and do not exhibit the same regularity as the wavy cracks observed here.

The formation of the wavy cracks occurs after that of the straight cracks. This is evident from Figure 6.1, which shows numerous examples of wavy cracks beginning/ending at straight cracks but no examples of straight cracks nucleating at a wavy crack. This observation is typical of the many samples studied, where straight cracks are very rarely observed to terminate at wavy ones, while the reverse is common.

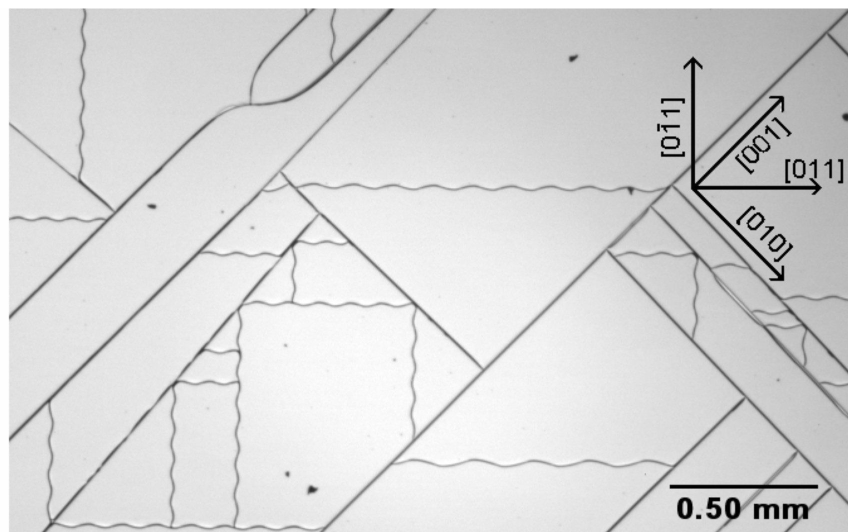

Figure 6.1 An image of the crack pattern on a 1.2 μm SiO_x layer on (100) silicon.

A 'phase' diagram of the failure modes occurring as a function of the anneal temperature and SiO_x thickness is shown in Figure 6.2. This clearly shows that there is a critical thickness and anneal temperature for the creation of cracks in SiO_x films. Straight cracks formed for 1 hour anneals in N_2 at temperatures above 440 ± 20 ºC and for SiO_x (40% Si) thicknesses greater than 600 ± 50 nm, while wavy cracks only occur for anneal temperatures above 525 ± 25 ºC and for films with thicknesses greater than 1100 ± 50 nm.

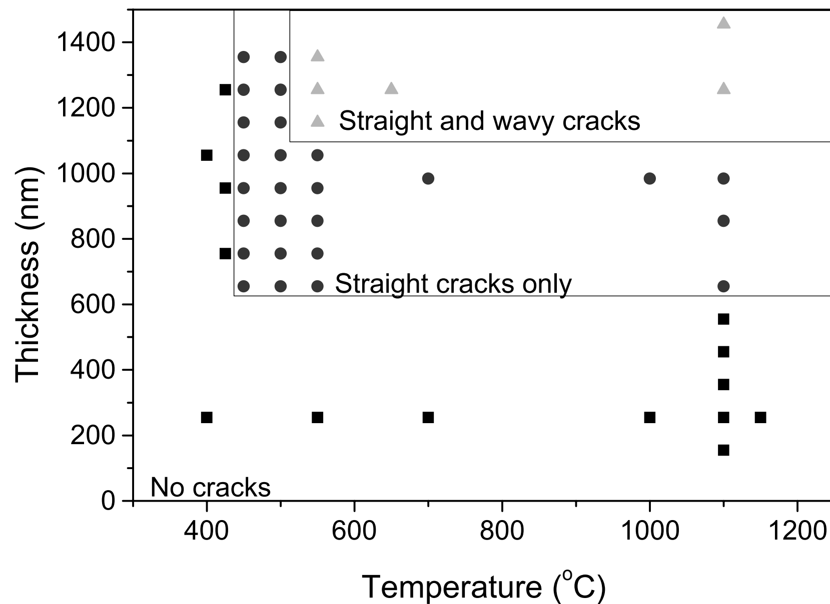

Figure 6.2 A phase diagram of various failures modes for SiO_x as a function of film thickness and anneal temperature for films annealed for 1 hour in N_2.

Cross sectional views of the straight cracks were prepared using either mechanical polishing or focused ion beam milling. Figure 6.3 shows that for thin layers (700nm or less), the cracks stop at the SiO_x/Si interface but for thicker layers they extend into the silicon substrate. The angle between the crack and the surface varied from 18 to 70°. The distribution of crack directions is shown in Figure 6.4 and indicates that fracture usually occurs along various low- index planes.

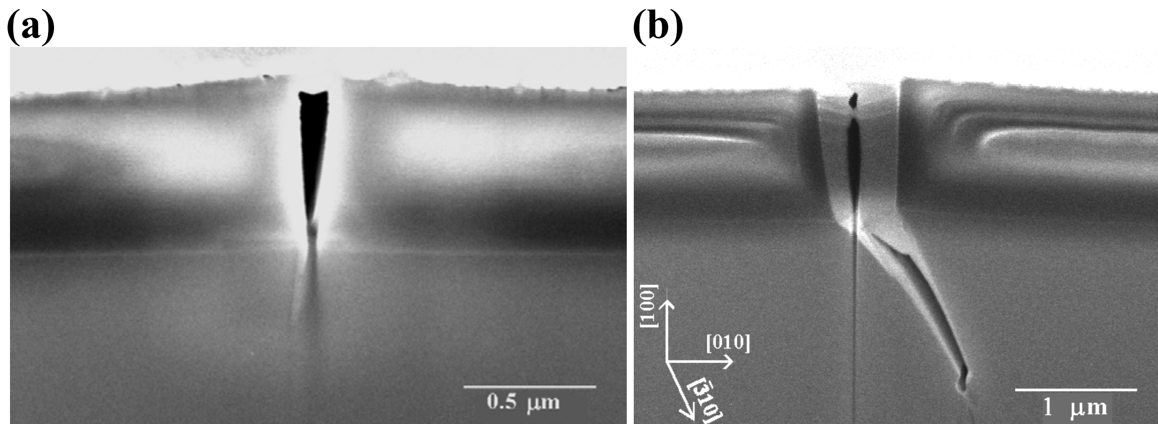

Figure 6.3 Cross sectional SEM images of a straight crack from a 655 nm thick SiO_x layer and (b) from a 1255nm SiO_x layer. The cross sections were prepared by focused ion beam milling.

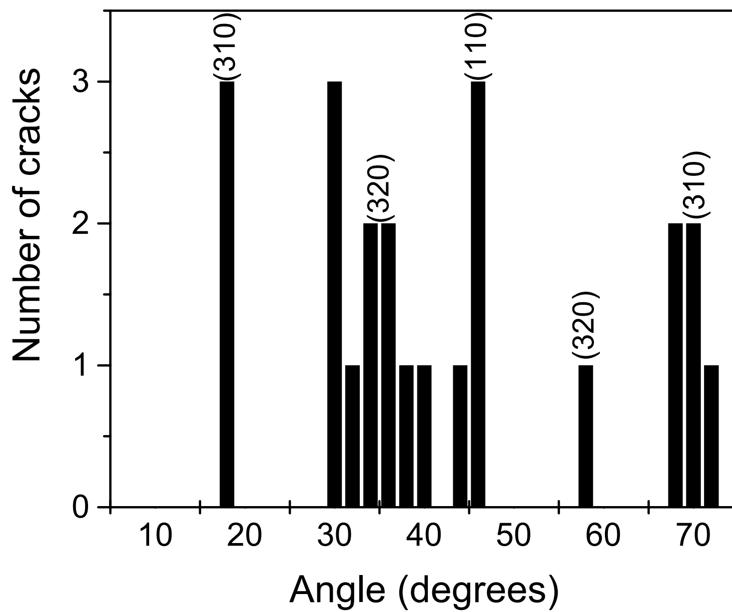

Figure 6.4 The distribution of angles between the crack direction in the substrate and the surface for samples with SiO_x films or microcavity structures deposited onto (100) silicon. The peaks corresponding to low-index cracking planes were identified on the graph.

The orientations of the wavy cracks were also examined using SEM sample cross sections, prepared by focused ion beam milling. A series of 70 images was taken over one half oscillation of a wavy crack. Similarly to straight cracks, wavy cracks also extend into the substrate, however, the angle they make with the surface depends on the position, or phase along the oscillation, as shown in Figure 6.5. It is interesting to note that where the crack runs in the [011] directions as in Figure 6.5(a), the crack makes a 55° angle with the surface corresponding to the $(11\bar{1})$ plane, a typical cleavage plane. As we mill further along the crack, the angle of the crack increases gradually until about 70° near the inflection point (Figure 6.5(b)). At this point a kink appears at the base of the crack which now has one part at about 70º and another at about -70º to the sample surface. This coincides with the point where the curvature of the crack changes direction. Between this inflection point (b) and the extreme right (c), the angle that the crack makes with the surface gradually changes from -70º to -55º approaching the $(11\bar{1})$ plane.

The curvature of the crack between points (a) and (b) can be explained by the effect of the tensile stress on the direction of crack propagation. At point (a), there is an asymmetry in the strain in the silicon substrate due to the crack geometry. The material on one side of the crack is more easily deformed than on the other as a consequence of the crack penetrating beneath it. For example in Figure 6.5 (a), there is more deformation on the right side of the crack because of the angle of the crack. This causes the crack to be deflected, in a similar way that a tensile stress field on one side of a crack can cause a crack to bend[75]. However, in this case, the more the crack is deflected away from the [110] direction the more the cracking plane deviates from the low energy $(11\bar{1})$ plane.

At point (b), the kink develops. It is not clear why the kink develops but presumably it is because it is now energetically favourable for the crack to fracture along a $(1\bar{1}1)$-like plane instead of continuing to fracture near the $(11\bar{1})$ plane. Once the kink does occur, it facilitates the reorientation of the crack towards the $(1\bar{1}1)$ cleavage plane thereby setting up conditions for repeated cycling. This is a particularly novel mode of crack propagation.

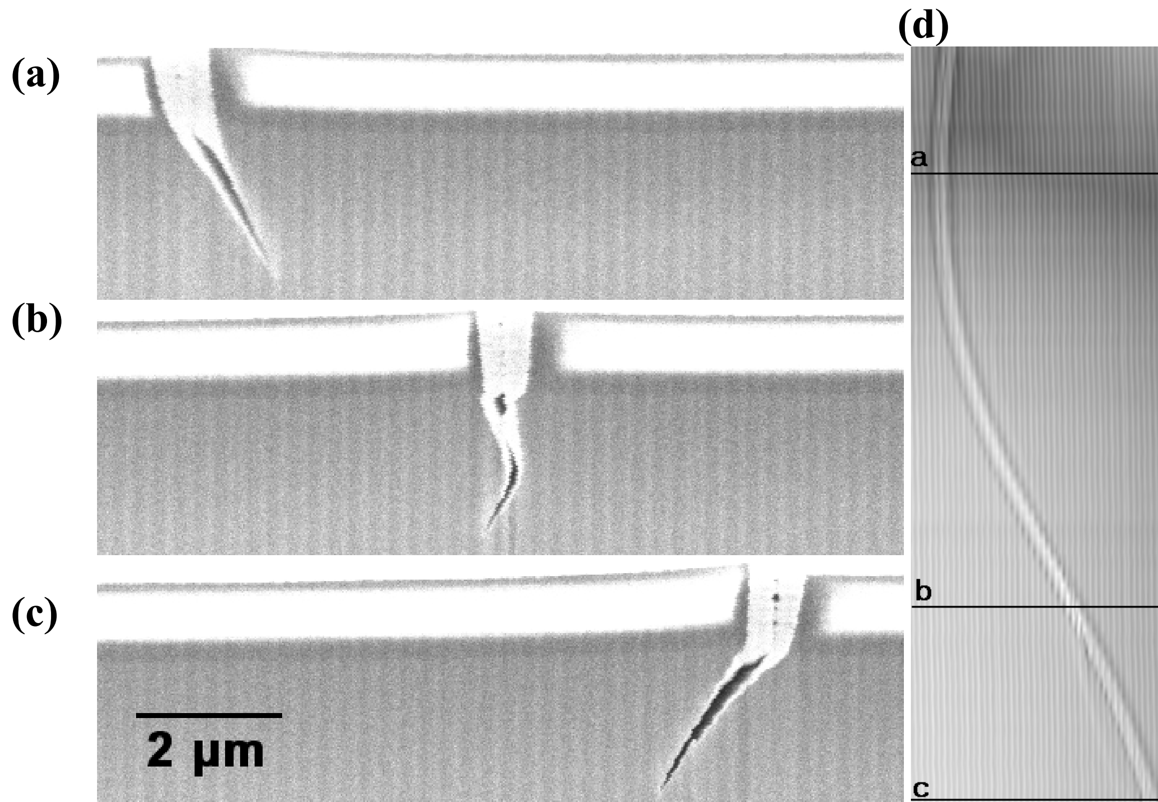

Figure 6.5 (a), (b), (c) Successive SEM images of the cross sections of a wavy crack as the sample is milled by a focused ion beam. (d) Image of the crack compiled from the sequence of images showing the position where the images on the left were taken.

6.1.b SiO_x films on (110) silicon

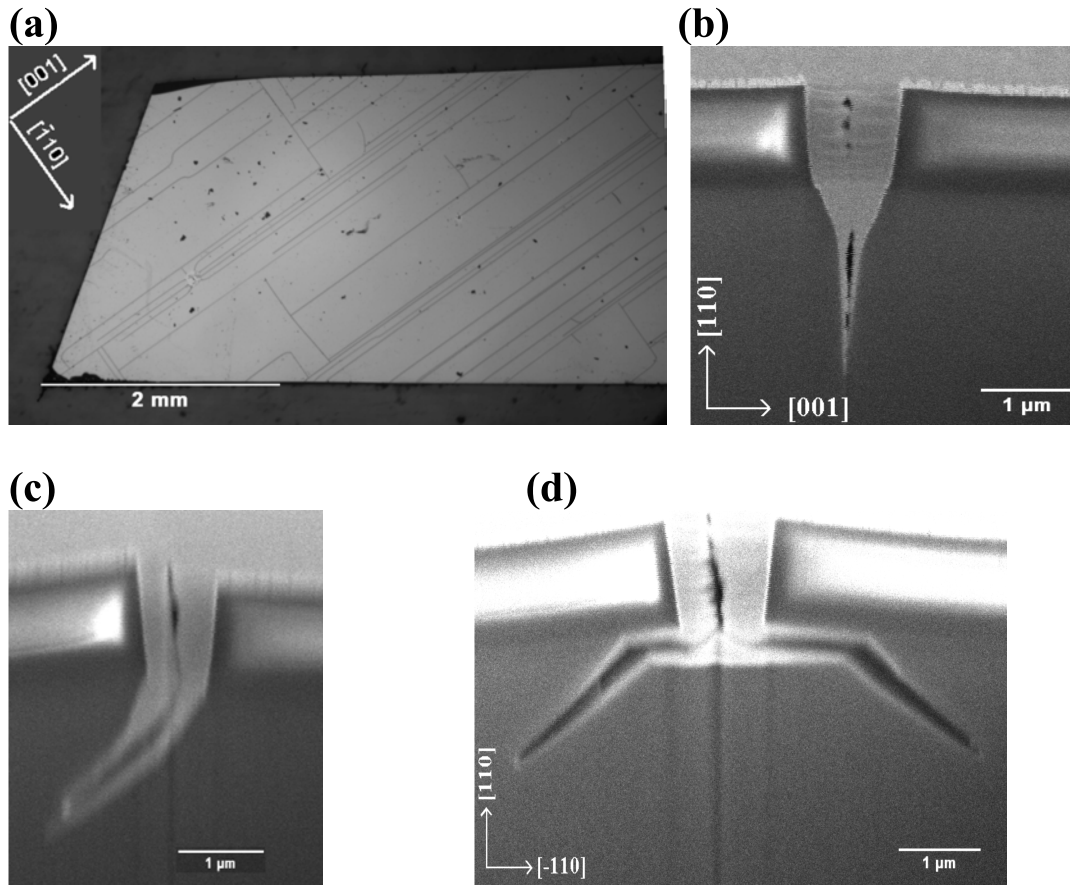

Figure 6.6 (a) An optical micrograph of cracks on (110) Si, (b) a cross sectional SEM micrograph of one of the cracks running in the [$\bar{1}$ 10] direction, (c) and (d) cross sectional SEM micrographs of cracks running in the [001] direction.

For SiO_x films deposited onto (110)-oriented Si, only straight cracks are observed. The majority of these cracks run in the [001] direction and a few run in the [$\bar{1}$10] direction as shown in Figure 6.6(a). Cross sectional SEM images of these cracks are shown in Figures 6.6(b), (c) and (d). These images show that the cracks again extend into the underlying Si substrate with the two sets of cracks having well defined angles below the surface. In cross section, the cracks that run in the [001] direction are perpendicular to the sample surface, indicating that the crack plane in the substrate is a ($\bar{1}$10) plane.

Below the surface, the cracks that run in the $[\bar{1}10]$ direction lie at a 35° angle to the surface in either direction (as in Figure 6.6(c)), or sometimes in both directions (as in Figure 6.6(d)). These cracking planes correspond to {111} planes.

6.1.c SiO_x films on (111) silicon

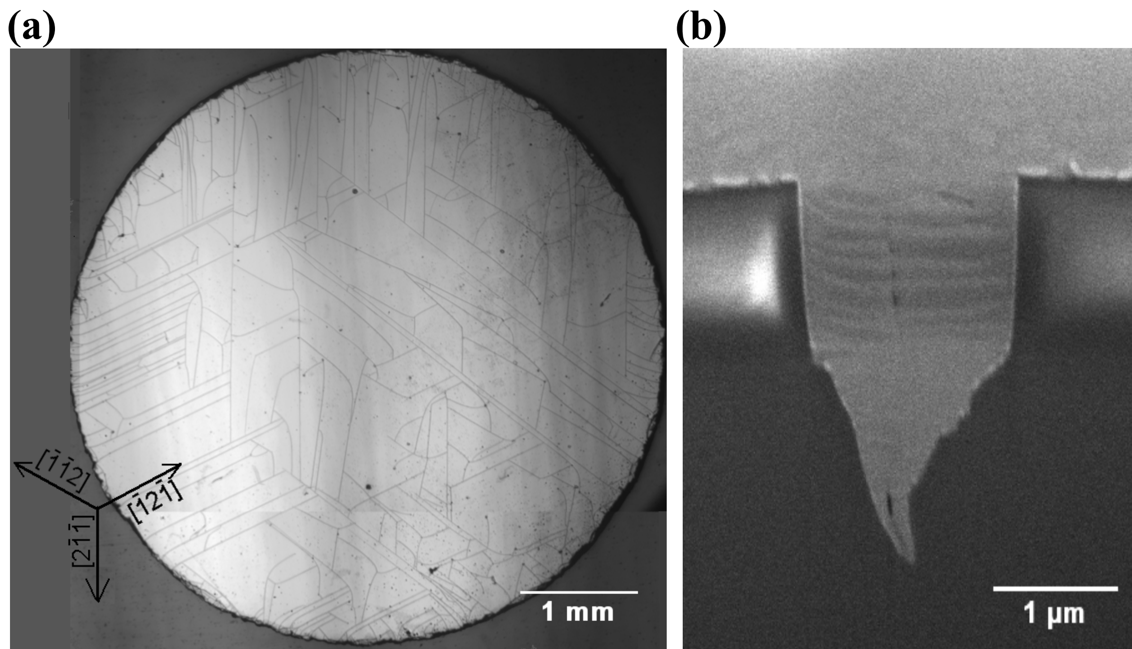

Figure 6.7 (a) Optical image of cracks on a 755nm SiO_x layer on a (111) Si substrate and (b) SEM image of the cross section of a crack on the same sample.

A 755nm layer of SiO_x (40% Si) was deposited on (111) silicon sample and was cut into a circular sample with a diameter of 5mm with an ultrasonic cutter then annealed for one hour at 1100°C. The cracks in films on (111) silicon show threefold symmetry (see Figure 6.7), with the cracks running along <211> directions. This indicated that the cracks have a preferred direction of propagation otherwise the pattern of cracks should have a six-fold symmetry. For example, assuming that the crack originate at the rough sample edges, there are many cracks originating from the lower left side of the sample propagating in the $[\bar{1}2\bar{1}]$

direction but no cracks originating from the upper right going in the $[1\bar{2}1]$ direction. The cross-sectional views of the cracks show that they are jagged and therefore do not lie on well defined cracking planes.

6.2 Cause of cracks

6.2.a Stress

Detailed analysis of crack formation and its correlation with film stress, compositional changes and annealing temperature has shown that the films crack because they shrink during high temperature annealing while the substrate does not. This causes a tensile stress in the film as well as a compressive stress in the substrate. In addition to this, the coefficient of thermal expansion of the film and the substrate are different, causing thermal stresses which are reversible upon cooling.

The stress in the film was measured as a function of temperature from room temperature to 650°C by measuring the radius of curvature of the sample. The temperature was increased in 50°C increments, and allowed to stabilise over 15 minutes before the stress measurement was performed. After the stress at the maximum temperature of 650°C was measured, the sample was kept at 650°C for two hours before cooling down. The sample was then cooled in 100°C steps over 30 minutes.

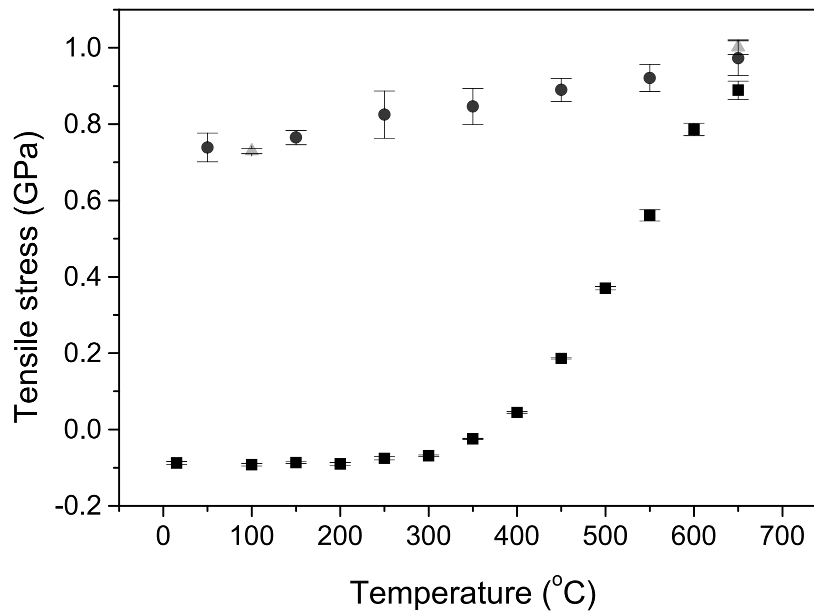

Figure 6.8 Tensile stress as a function of temperature for a 1.2μm layer of 40% silicon SiO_x. The squares represent measurements taken during the first heating cycle, the circles represent the first cooling cycle and the triangles are for subsequent cycles

The stress as a function of temperature was measured for four silicon-rich oxide compositions from 36% to 52% silicon, and the SiO_2 layer. Figure 6.8 shows a stress measurement for a 1.2μm layer of 40% SiO_x. After deposition, the sample is in slight compression, which does not change much upon heating from room temperature up to the film's deposition temperature of 300 °C. Between 350 and 650°C there is a large increase in tensile stress. Most of the accumulated stress is due to irreversible changes such as hydrogen release and the subsequent bonding rearrangement[76], which is particularly significant for silicon-rich oxide layers employed in the present study as discussed in section 4.2.b. In addition, some of the stress is due to the differential thermal expansion of the film and substrate. This thermal stress is reversible as shown in Figure 5.7, and can be reduced by lowering the temperature. The total change in stress in the sample after a full

heating cycle was 0.81 ± 0.07 GPa. Within experimental uncertainty, this stress did not depend on film thickness.

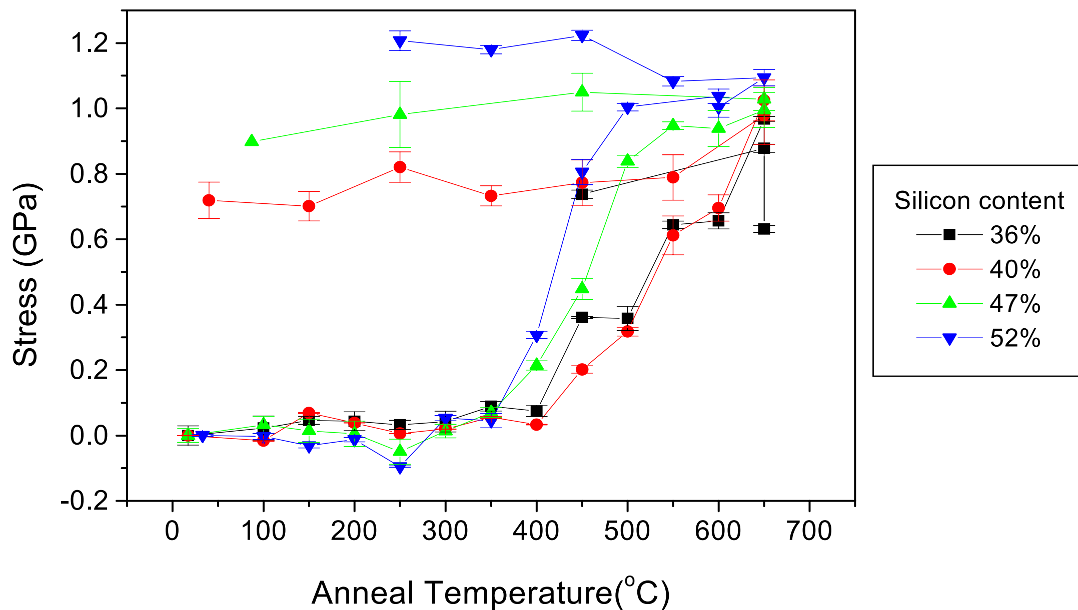

Figure 6.9 Tensile stress as a function of anneal temperature for 250nm layers of different SiO_x compositions.

Figure 6.9 shows the change in stress as a function of temperature for the 4 silicon-rich oxide compositions. In this graph, the stresses were offset to the same initial stress, in order better compare the accumulation of tensile stress. The samples with the higher hydrogen concentration (and higher Si concentration) tend to develop higher stress at lower temperatures than those with lower hydrogen content. At 650°C, the difference in stress is reduced possibly because of stress relief due to sample cracking.

By way of comparison, stress measurements on stoichiometric SiO_2 layers show similarly that the initial stress is compressive and becomes less compressive at higher temperature. However, in the case of a 250nm SiO_2 film deposited onto a 500 μm thick silicon substrate, the compressive stress only varied from 0.42 ± 0.04 GPa to 0.16 ± 0.01 GPa when the

sample was heated from room temperature to 650°C. This stress returned to 0.37 ± 0.02 as the sample was cooled back to room temperature.

6.2.b The Elastic Modulus

Chow[77] has observed similar oriented cracks in xerogel silica films on silicon and argues that the cracks should propagate perpendicular to the direction of minimum plane strain elastic modulus. The mechanical properties of silicon can be calculated for any arbitrary direction using well developed theories[78,79]. These theories predict that on (100) silicon the cracks should propagate in the <110> directions, on (110) silicon, the cracks should run in the [001] and $[\bar{1}10]$ directions, and on (111) silicon that there should be no preferred crack orientation. Figure 6.10 shows that the prediction holds true for the straight cracks on (100) and (110) silicon. However, there is clearly preferred cracking along the <112> directions for the film deposited on (111) silicon, which is not predicted.

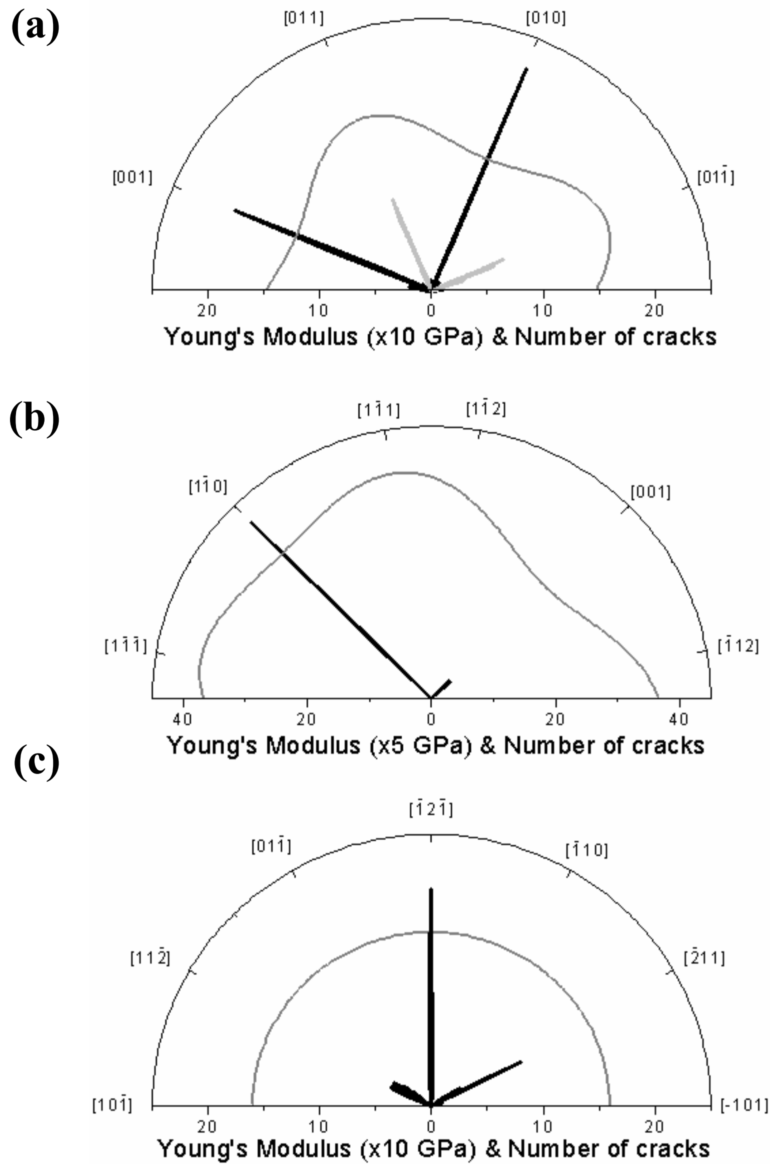

Figure 6.10 Polar plot of Young's modulus and the number of cracks observed in 15 mm^2 area vs. direction for (a) a 1250nm SiOx layer on (100) Si, (b) a 755nm SiO_x layer on (110) Si, and (c) a 755nm SiO_x layer on (111) Si. The grey curve represents the Young's modulus while the black and light grey curves represent the number of straight and wavy cracks respectively.

6.2.c Lomer dislocations

Since the macroscopic mechanical properties in the surface plane of (111) silicon are isotropic[78], the explanation for <112> oriented cracks must be due to microstructure.

Indentation experiments also show preferential crack propagation in the $[\bar{1}\,\bar{1}\,2]$, $[\bar{1}2\bar{1}]$ and $[2\,\bar{1}\,\bar{1}]$ directions[80, 81] but not in the opposite directions. The cracks formed by indentation are attributed to the accumulation of gliding dislocations which can combine to form Lomer dislocations[81]. As these grows they produce an increase in shear stress until it is sufficient to cleave the sample along {110} planes. It is believed that a similar process is responsible for the cracks in (111) substrates observed here.

6.3 Effect of cracks on the microcavities

The cracks observed in microcavity structures are similar to the straight cracks produced in thick SiO_x layers. When these cracks occur in the microcavity structure, as shown in Figure 6.11, they can alter the optical properties of the stack by introducing an air gap, modifying the orientation of the stack, or relieving the stress near the crack. This in turn can influence the PL emission from the structure. Figure 6.12 compares the typical PL spectrum of a microcavity near a crack to that away from the crack. The effect of the cracks is small because they only influence the PL over a small fraction of the total sample area. The main difference is that the PL at the crack is slightly more intense and that there is a shoulder at the long wavelength side of the main emission peak.

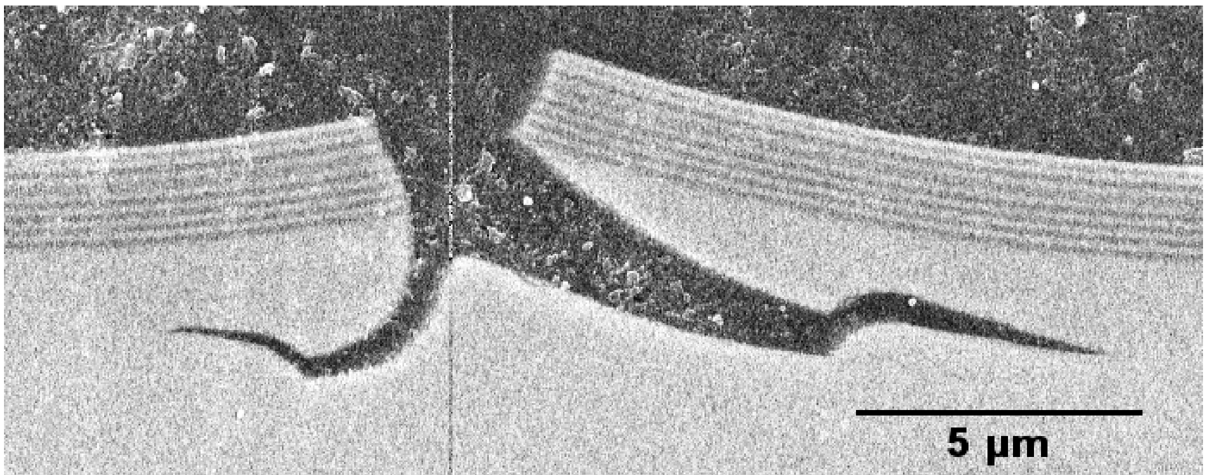

Figure 6.11 SEM micrograph of a cross section of a crack in a microcavity

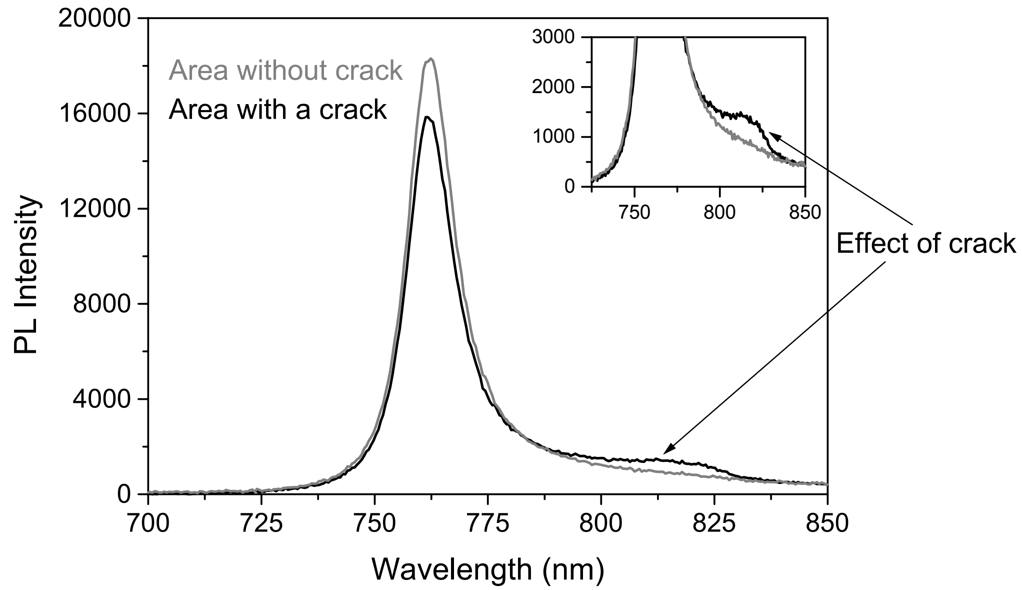

Figure 6.12 PL spectrum of a microcavity with and without a crack in the field of view.

In order to determine the origin of these spectral features, a PL map of the sample was taken at a magnification of 30X and is shown in Figure 6.13 (top panel). This figure shows that the cracks emit more light than the surrounding material. The thin red line at y = 35μm, indicates the location where PL profiling was performed on the sample. The resulting plot of the PL intensity versus wavelength and position is shown in Figure 6.13 (bottom panel). At both extremes of the x-axis, the crack has little influence on the PL and the peak emission wavelength is about 760nm. However as the position approaches the crack from both sides, the peak emission wavelength is shifted to longer wavelengths, about 820nm, at the crack.

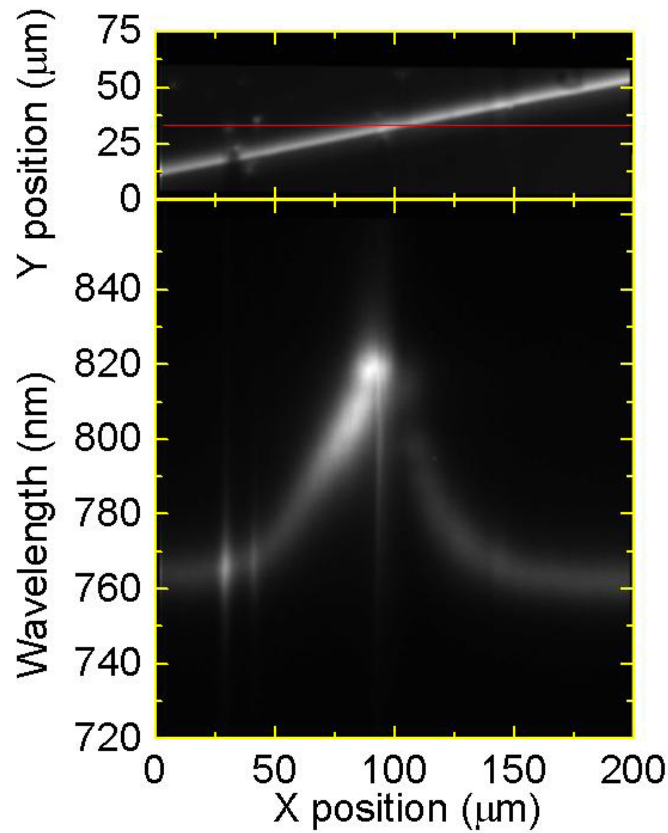

Figure 6.13 Top: PL map of a microcavity showing a crack and Bottom: the PL intensity vs. position and wavelength of the same area.

The shift to longer wavelengths can be understood from the influence of the crack on the microcavity structure. Near the crack, the tensile stress perpendicular to the crack is relieved. This reduction in stress is accompanied by a contraction perpendicular to the crack and an expansion in thickness due to the Poisson effect. This expansion of the microcavity increases its resonant wavelength. SEM images of the microcavity shows that within several μm from the crack, the microcavity is about 10% thicker than in regions away from the crack, consistent with the increase in the peak emission wavelength observed.

6.4 Delamination

Another observed stress-induced defect consists of small circular regions of delamination as well as some much larger areas of delamination as shown in figures 6.14(a) and (b). This delamination is seen predominantly on silicon nitride films or microcavity structures that have the nitride layer deposited first. These defects occur infrequently in some silicon-rich-oxides as well. The film starts by bulging out at certain locations, which is believed to be the result of compressive stress in the film[82].

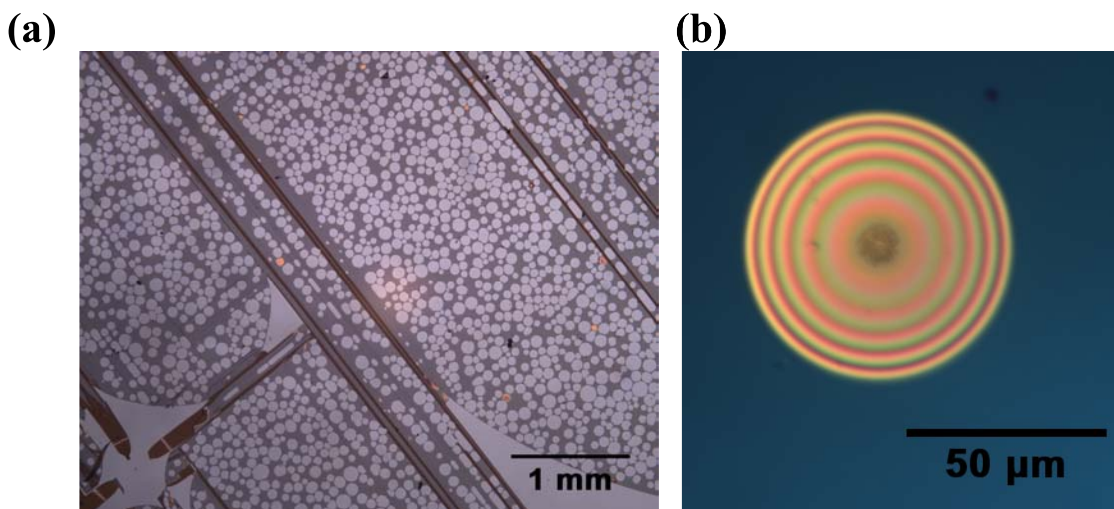

Figure 6.14 Micrographs showing delamination of silicon nitride after annealing. (a) A microcavity structure with the nitride layer deposited first in the nitride/oxide mirror stack and (b) an intact delaminated bubble in a 100nm nitride films showing Newton's rings.

If the overlying film is in compression, the film will start to bulge outwards where there is weak adhesion of the film. The compressive stress around this delamination causes the film to bulge out and increase the radius of the delaminated area. The film usually fails leaving behind a circular hole in the film. Sometimes the bulge remains intact as in the example in Figure 6.14(b) where a series of Newton's rings associated with changes in the thickness of the underlying 'air' pocket can be seen.

6.5 Methods to minimise defects

6.5.a Thermal treatment

Bulla et al.[83] have also deposited silicon oxide films using PECVD, which subsequently cracked during thermal annealing. They have shown that it is possible to produce thicker SiO_2 layers without cracks if their deposition is interrupted and the stress is relieved by a two minute rapid thermal anneal at 900°C before continuing. This procedure was applied to the SiO_2/SiO_x stacks. Thicker structures were produced without cracking if a stress relieving RTA was performed. Without this stress reduction scheme, the maximum number of layers in a sample of alternating layers of 143nm SiO_2 and 130 nm SiO_x, is between 8 and 12 layers before cracking occurred. However, if the deposition is interrupted after every forth layer, and the stress is relieved by annealing the sample at 1000°C for one minute then crack-free stacks of at least 22 layers can be obtained.

6.5.b Patterning

Photolithographic patterning of the layers can also reduce the crack density by relieving the stress in the majority of the sample. To study this effect a photo-resist mask was deposited onto the sample to protect a series of circular areas. The unprotected areas were removed by Reactive Ion Etching (RIE), leaving a series of circular mesa structures. In the patterned structures, if a cracks forms it is confined to the mesa structure where it originated, thus the propagation of cracks is limited.

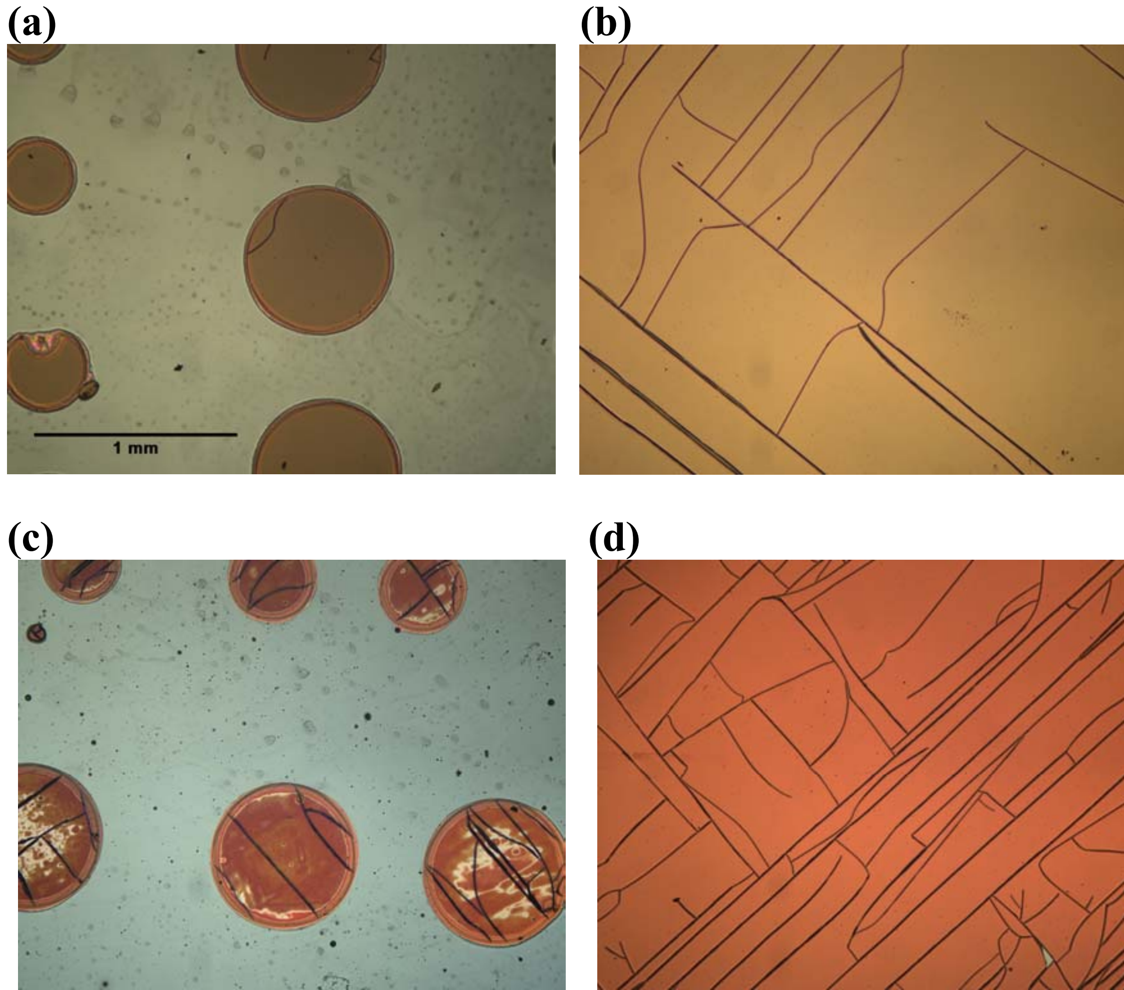

Figure 6.15 Optical image of (a) a mesa structure with 6 layers per mirror, (b) a planar microcavity with 6 layers/mirror, (c) a mesa structure with 10 layers/mirror and (d) a planar microcavity with 10 layers/mirror. Each of theses images were taken with the same magnification.

Circular mesa structures with diameters of 0.75mm and 0.4mm were produced then annealed for 1 hour at 1100°C. Figure 6.15 shows images of the mesa structured microcavities as well as the planar microcavity samples after annealing. The mesa structures show significantly less cracking than the equivalent planar structure. In fact, for microcavities with 6 layers in each of its DBR, 70% of the 0.44mm^2 mesa structures were

crack free. However, as the number of layers is increased, the average distance between the cracks is smaller than in the planar structures.

6.5.c Layer order

To avoid the delamination described in section 6.4, it was necessary to deposit the SiO_2 layer first when depositing the microcavity structure. Clearly the SiO_2 has better adhesion to silicon than silicon nitride.

It was also observed that the average distance between the cracks depended on the composition of the final layer of the stack. A series of samples were produced, each sample consisted of a different number of layers. The layers consisted of alternating layers of silicon dioxide and nitride except for the 9th layer which consisted of a layer of SiO_x. Therefore after the 14th layer the sample consisted of the microcavity studied in chapter 4. Figure 6.16 shows the average number of cracks in the sample vs. the number of layers in the microcavity. Cracks did not appear until the 9th layer was deposited (the SiO_x layer). This sample had 19 cracks/cm. Samples terminated with SiO_2 (samples with 11 and 13 layers) had a similar density of cracks while the samples terminated by nitride (samples with 10, 12 and 14 layers) had a higher density (~40 cracks/cm).

Although these results indicate that there will be fewer defects in a microcavity terminated with an oxide layer instead of a nitride layer, the PL intensity was higher in the nitride terminated microcavities[84] because the number of layers also affects the reflectivity of the distributed Bragg reflectors.

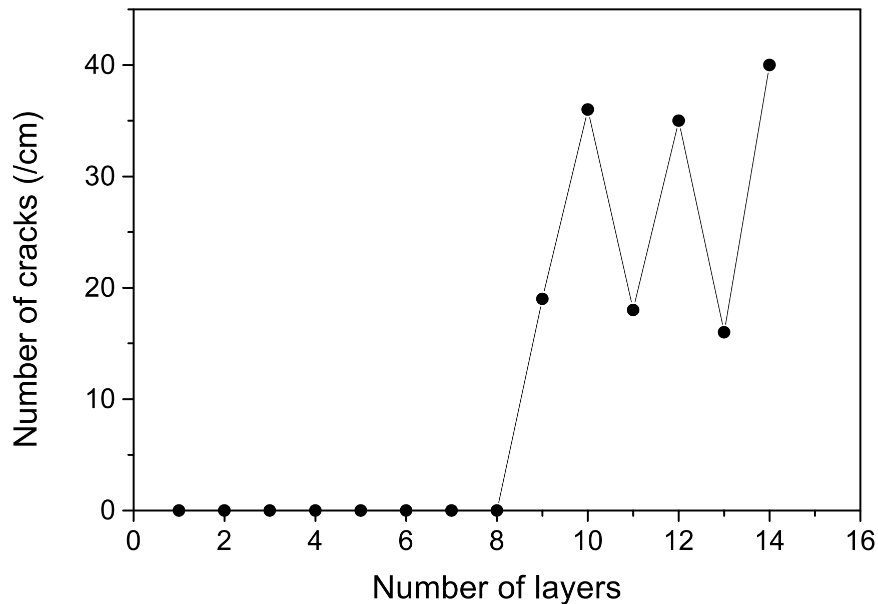

Figure 6.16 Number of cracks vs. the number of layers in a stack of layers used to produce the microcavity structure.

6.6 Summary and Conclusions

- The application of PECVD thin-films is limited by stress-induced failure that can result in cracking and delamination of the films.
- Cracking of SiO_x thin films is the result of tensile stress that develops in the films during annealing as a direct consequence of hydrogen desorption.
    - There is a direct correlation between the Si excess and the H content
    - Tensile stresses as high as 1 GPa result from hydrogen loss
- Delamination is the result of compressive stresses and is most commonly observed for films with poor adhesion.

- The crack patterns that develop in PECVD deposited SiO_x layers after thermal annealing depend on the composition and thickness of the layers, the annealing temperature and time, and the substrate orientation.

- For (100) substrates, straight cracks form along <100> directions and wavy cracks form along <110> directions
- For (110) substrate, straight cracks form predominantly along <110> directions and less frequently along <100> directions
- For (111) substrates, cracks form along <211> directions, despite isotropic mechanical properties of the substrate.

- Cross-sectional imaging of these cracks reveals that the cracks extend through the deposited film into the underlying substrate, and that the substrate crack lies on specific low index planes.
- Oscillating cracks represent a particularly novel form of crack propagation and appear to be the result of interactions between stress relief and the dependence of surface energy on crack direction.
- Cracks were also observed in microcavity structures but have only a small effect on the PL.
  - The cavity thickness increases due to the stress relief at the crack, which increases the cavity's resonant wavelength by about 10%.
  - Delamination is minimised by depositing a SiO_2 layer first. Silicon nitride layers show poor adhesion and lead to delamination.
  - Crack concentrations can be reduced by patterning the sample into mesa structures.
  - Thicker defect-free structures can be grown if rapid thermal annealing is employed to relieve the stress of intermediate structures.[54]

Chapter 7 Conclusions

This thesis has investigated light emission from Si nanocrystals and the influence of optical microcavities and associated structures on the spectral emission of such nanocrystals. The study has concentrated on structures grown by plasma-enhanced chemical deposition (PECVD), specifically on structures fabricated from silicon-rich oxides (SiO_x), silicon dioxide (SiO_2) and silicon nitride.

Silicon nanocrystals were produced in silicon-rich oxides using PECVD and high temperature annealing. These samples were shown to produce strong room temperature PL, the intensity of which depended on the excess silicon concentration. The strongest emission was observed for samples with silicon concentrations around 40% silicon. At lower concentrations (<37 atomic %) no significant nanocrystal emission was observed, whilst at higher concentrations, the total PL intensity decreased with increasing Si concentration. Films with a silicon content of more than 37 atomic % are required to produce PL because the nitrogen present in the films reduces the effective excess Si concentration by reacting with it to form silicon nitride/oxynitride. For films with a silicon content greater than 40 atomic %, the nanocrystal size and density are such that nanocrystals interact and the excitons are more likely to encounter non-radiative recombination centres.

It was shown that the nanocrystal luminescence can be increased by hydrogen passivation using two different methods. In one method the hydrogen was provided by the annealing ambient, while in the second it was provided by the silicon nitride layers. The forming gas anneal provided an enhancement in PL intensity by a factor of 2-7, depending on the excess

Si content and the passivation using the nitride layers provided an enhancement of 5-24. In contrast, small concentrations of metal impurities were shown to reduce the PL intensity. Metal impurities such as Cu, Fe and Au are known to reduce the carrier lifetimes in bulk silicon and were implanted into silicon-rich oxides to assess their impact on the luminescence. Au and Fe reduced the number of luminescent nanocrystals, consistent with an increase in non-radiative recombination. (Cu was lost from the sample during annealing and had no significant effect on the luminescence).

Microcavity structures containing silicon nanocrystals were produced by PECVD with mirrors consisted of distributed Bragg reflectors made from alternating SiO_2 and silicon nitride layers. The use of SiO_2/Si_3N_4 microcavities provided sufficient refractive index contrast to produce a stop-band over the nanocrystal spectral range and resulted in microcavities with Q-factors as high as 200, although values of 50 were typical. Cavities were designed with resonant wavelengths ranging from 730 to 930nm. In principle, much larger Q values are possible, but in practice the stress in the structure increases as more layers are added. The structure with the highest PL intensity was a microcavity which was annealed for only 15s at 1000°C. In this case, the silicon nitride acted as source of hydrogen ensuring excellent passivation of the nanocluster/nanocrystal formed. This provides a method of producing very strong PL using a process with a low thermal budget.

In the SiO_x film as well as the microcavity structures, a large tensile stress develops as the samples are annealed. This is due to the incorporation of hydrogen in the films during deposition. As the samples are annealed, the hydrogen is released and the film densifies leading to tensile stress and film cracking. These cracks often extend through the film and into the underlying substrate and consequently the substrate orientation (100), (110) and

(111) was found to have a strong influence on the direction of the cracks. For the films and structures deposited onto (100) silicon, straight cracks were observed to propagate along <100> directions and novel wavy cracks were observed to propagate along <110> directions. In the case of films deposited on (110) silicon, straight cracks propagated predominantly along <110> directions with a smaller number propagating along <100> directions. This was shown to be consistent with the orientational dependence of mechanical properties in silicon. For film deposited on (111) silicon, cracks were observed to propagate along <211> directions, consistent plastic deformation of the substrate.

The oscillating cracks observed in thick SiO_x films on (100) silicon are particularly intriguing, exhibiting a period of 100μm and lengths of up to ~1cm. These crack were shown to be oriented along the <110> directions and SEM imaging of cross sectional samples prepared with a focused ion beam showed that the cracking plane oscillated between two {111} planes.

Several methods were shown to be useful in minimising the cracks, including sample patterning, layer ordering and intermediate annealing. However the problem of cracking was shown to limit the number of layer in the microcavities, thereby limiting their application.

7.1 Future work

One of the more interesting silicon-based light sources investigated during the course of this study consisted of a SiO_2/Si_3N_4 based microcavity annealed for only 15s at 1000°C. This structure produced strong PL intensity with a low thermal budget, making it easier to

integrate with other devices/structures. It should also be possible to provide excellent nanocrystal passivation at lower temperatures(~700°C)[29] but this may come at the expense of nanocluster/nanocrystal growth. Further work is required to assess the viability of such processing schemes.

An electrically operated light source would increase the usefulness of any silicon-based light source. Developing a practical method for exploiting electroluminescence from silicon nanocrystals would be beneficial. For example, one or both distributed Bragg reflectors could be replaced by a metal mirror. These metal mirrors could then be used as electrical contacts allowing electro-luminescence.

Different microcavity structures are also of considerable interest. For example, instead of the planar microcavity used in this study, in-plane microcavities could be incorporated into one dimensional waveguides. This would make it possible to use nanocrystal-based light sources in planar integrated optical circuits. SiO_x layers could be deposited and then patterned into waveguides using lithography. Microcavities could then be defined by periodically modifying the index of refraction along this waveguide by using a focused ion beam. Alternatively, the waveguides could be made photosensitive with the addition of germanium impurities[85], then the microcavities formed using UV light[86].

Finally, in relation to thin film failure and crack propagation, it would be useful to undertake a comprehensive finite element model of the stress and strain distributions during processing. This would enable a better understanding of the failure mechanisms in films with applications to the study of nanocrystal films, optical thin films, and MEMS (Micro-Electro-Mechanical Systems) technology and any other fields utilising thin films.

References

1. L. Canham, *Gaining light from silicon,* Nature, **408**, 411 (2000).

2. H. Takagi, H. Ogawa, Y. Yamazaki, A.Ishizaki, and T. Nakagiri, *Quantum size effects on photoluminescence in ultrafine Si particles.,* Applied Physics Letters, **56**, 2379 (1990).

3. L.T. Canham, *Silicon quantum wire array fabrication by electrochemical and chemical dissolution of wafers,* Applied Physics Letters, **57**, 1046 (1990).

4. *Silicon Photonics*, ed. L. Pavesi and D.J. Lockwood. 2004: Springer.

5. E. Schubert, A. Vredenberg, N. Hunt, Y. Wong, P. Becker, J. Poate, D. Jacobson, L. Feldman, and G. Zydzik, *Giant enhancement of luminescence intensity in Er-doped Si/SiO_2 resonant cavities,* Applied Physics Letters, **61**, 1381 (1992).

6. M. Lannoo, C. Delerue, and G. Allan, *Theory of radiative and nonradiative transitions for semiconductor nanocrystals,* Journal of Luminescence, **70**, 170 (1996).

7. J.R. Chelikowsky and M.L. Cohen, *Nonlocal pseudopotential calculations for the electronic structure of eleven diamond structure and zinc-blende semiconductors,* Physical Review B, **14**, 556 (1976).

8. M.V. Wolkin, J. Jorne, P.M. Fauchet, G. Allan, and C. Delerue, *Electronic states and luminescence in porous silicon quantum dots: the role of oxygen,* Physical Review Letters, **82**, 197 (1999).

9. G. Ledoux, O. Guillois, D. Porterat, C. Reynaud, F. Huisken, B. Kohn, and V. Paillard, *Photoluminescence properties of silicon nanocrystals as a function of their size,* Physical Review B, **62**, 15942 (2000).

10. H. Tamura, M. Rtickschloss, T. Wirschem, and S. Vepiek, *Origin of the green/blue luminescence from nanocrystalline silicon,* Applied Physics Letters, **65**, 1537 (1994).

11. T. Shimizu-Iwayama, M. Ohshima, T. Niimi, S. Nakao, K. Saitoh, T. Fujita, and N. Itoh, *Visible photoluminescence related to Si precipitates in Si^+ -implanted SiO_2.,* Journal of Physics: Condensed Matter, **5**, L375 (1993).

12. M.L. Brongersma, A. Polman, K.S. Min, and H.A. Atwater, *Depth distribution of luminescent Si nanocrystals in Si implanted SiO_2 films on Si,* Journal of Applied Physics, **86**, 759 (1999).

13. S. Guha, S.B. Qadri, R.G. Musket, M.A. Wall, and T. Shimizu-Iwayama, *Characterization of Si nanocrystals grown by annealing SiO_2 films with uniform concentrations of implanted Si,* Journal of Applied Physics, **88**, 3954 (2000).

14. B. Garrido, M. López, C. Garcia, A. Pérez-Rodriguez, J.R. Morante, C. Bonafos, M. Carrada, and A. Claverie, *Influence of average size and interface passivation on the spectral emission of Si nanocrystals embedded in SiO_2,* Journal of Applied Physics, **91**, 798 (2002).

15. S. Cheylan, N.B. Manson, and R.G. Elliman, *Dose dependence of room temperature photoluminescence form Si implanted SiO_2,* Journal of Luminescence, **80**, 213 (1999).

16. T. Shimizu-Iwayama, D.E. Hole, and P.D. Townsend, *Excess Si concentration dependence of the photoluminescence of Si nanoclusters in SiO2 fabricated by ion implantation,* Journal of Luminescence, **80**, 235 (1999).

17. F. Iacona, G. Franzo, and C. Spinella, *Correlation between luminescence and structural properties of Si nanocrystals,* Journal of Applied Physics, **87**, 1295 (2000).

18. Chi-Fa, W.-T. Tseng, and M.S. Feng, *Formation and characteristics of silicon nanocrystals in plasma-enhanced chemical-vapor-deposited silicon-rich oxide,* Journal of Applied Physics, **87**, 2808 (2000).

19. Y.Q. Wang, G.L. Kong, W.D. Chen, H.W. Diao, C.Y. Chen, S.B. Zhang, and X.B. Liao, *Getting high-efficiency photoluminescence from Si nanocrystals in* SiO_2 *matrix.,* Applied Physics Letters, **81**, 4174 (2002).

20. K.E. Mattsson, *Plasma-enhanced growth, composition, and refractive index of silicon oxy-nitride films,* Journal of Applied Physics, **77**, 6616 (1995).

21. T.D.M. Weijers, R.G. Elliman, and H. Timmers, *Heavy ion elastic recoil detection analysis of silicon-rich silica films,* Nuclear Instruments and Methods B, **219**, 680 (2004).

22. Y.C. Cheng, *Electronic states at the silicon-silicon dioxide interface,* Progress in Surface Science, **8**, 181 (1977).

23. E.H. Poindexter and P.J. Caplan, *Characterization of Si/*SiO_2 *interface defects by electron spin resonance,* Progress in Surface Science, **14**, 1 (1983).

24. E. Neufeld, S. Wang, R. Apetz, C. Buchal, R. Carius, C.W. White, and K.K. Thomas, *Effect of annealing and* H_2 *passivation on the photoluminescence of Si nanocrystals in* SiO_2*,* Thin Solid Films, **294**, 238 (1997).

25. S.P. Withrow, C.W. White, A. Meldruim, J.D. Budhai, D.M. Hembree, and J.C. Barbour, *Effects of hydrogen in the annealing environment on photoluminescence form Si nanoparticles in* SiO_2*,* Journal of Applied Physics, **86**, 396 (1999).

26. S. Cheylan and R.G. Elliman, *Effect of particle size on the photoluminescence from hydrogen passivated Si nanocrystals in* SiO_2*,* Applied Physics Letters, **78**, 1912 (2001).

27. S. Cheylan and R.G. Elliman, *Photoluminescence from Si nanocrystals in silica: The effect of hydrogen,* Nuclear Instruments and Methods in Physical Research B, **175**, 422 (2001).

28. A.R. Wilkinson and R.G. Elliman, *Kinetics of H_2 passivation of Si nanocrystals in SiO_2,* Physical Review B, **68**, 155302 (2003).

29. S. Narasimha and A. Rohatgi, *Effective passivation of the low resistivity silicon surface by rapid thermal oxide/plasma silicon nitride stack,* Applied Physics Letters, **72**, 1872 (1998).

30. J. Schmidt, M. Kerr, and A. Cuevas, *Surface passivation of silicon solar cells using plasma-enhanced chemical-vapour-deposited SiN films and thin thermal SiO2/plama SiN stacks,* Semiconductor Science and Technology, **16**, 164 (2001).

31. H. Benisty, H. DeNeve, and C. Weisbuch, *Impact of Planar Microcavity Effects on Light Extraction—Part I: Basic Concepts and Analytical Trends,* IEEE Journal of Quantum Electronics, **34**, 1612 (1998).

32. L. Pavesi, *Porous silicon dielectric multilayers and microcavities,* La Rivista del Nuovo Cimento, **20**, 1 (1997).

33. L. Pavesi, C. Mazzoleni, A. Tredicucci, and V. Pellegrini, *Controlled photon emission in porous silicon microcavities,* Applied Physics Letters, **67**, 3280 (1995).

34. S. Setzu, P. Ferrand, and R. Romestain, *Optical properties of multilayered porous silicon,* Materials Science and Engineering B, **69**, 34 (2000).

35. M. Ghulinyan, C.J. Oton, G. Bonetti, Z. Gaburro, and L. Pavesi, *Free-standing porous silicon single and multiple optical cavities,* Journal of Applied Physics, **93**, 9724 (2003).

36. P.A. Snow, E.K. Squire, P. Russell, and L.T. Canham, *Vapour sensing using the optical properties of porous silicon Bragg mirrors,* Journal of Applied Physics, **86**, 1781 (1999).

37. A. Serpengüzel, *Amorphous silicon nitride microcavities,* Journal of the Optical Society of America, **18**, 989 (2001).

38. A. Serpengüzel and S. Tanriseven, *Controlled photoluminescence in amorphous-silicon-nitride microcavities,* Applied Physics Letters, **78**, 1388 (2001).

39. F. Giorgis, *Optical microcavities based on amorphous silicon-nitride Fabry-Perot structures,* Applied Physics Letters, **77**, 522 (2000).

40. V. Ballarini, G. Barucca, E. Bennici, C.F. Piri, C. Ricciardi, E. Tresso, and F. Giorgis, *New insight on amorphous silicon-nitride microcavities,* Physica E, **16**, 591 (2003).

41. M. Bayindir, S. Tanriseven, A. Aydinli, and E. Ozbay, *Strong Enhancement of Spontaneous emission in amorphous-silicon-nitride photonic crystal based coupled-microcavity structures,* Applied Physics A, **73**, 125 (2001).

42. M. Bayindir, C. Kural, and E. Ozbay, *Coupled optical microcavities in one-dimensional photonic bandgap structures,* Journal of Optics A: Pure and Applied Optics, **3**, S184 (2001).

43. Hecht, *Optics*. 2nd ed. 1987: Addison-Wesley Publishing.

44. Knittl, *Optics of thin films (an optical multilayer theory)*. 1976, New York: Wiley.

45. *OXFORD Plasmalab 80 Plus System Manual*. 1996.

46. P.N.K. Deenapanray, H.H. Tan, J. Lengyel, A. Durandet, M. Gal, and C. Jagadish, *Impurity-free interdiffusion in GaAs/*$Al_{0.54}Ga_{0.46}$*As multiple quantum wells capped with PECVD SiOx: effect of nitrous oxide flow,* IEEE Optoelectronics and Microelectronics Materials Devices Proceeding, COMMAD 1998, 361 (1998).

47. P. Benalloul and J. Benoit, *Decay of ZnS:Mn emission in thin films - revisited,* Journal of Crystal Growth, **101**, 989 (1990).

48. R. Ulrich and R. Torge, *Measurement of thin film parameters with a prism coupler,* Applied Optics, **12**, 2901 (1973).

49. *Metricon model 2010 prism coupler, Thin film thickness / refractive index measurement system Operation and maintenance guide*. 2003: Metricon Corporation.

50. W.-K. Chu, J.W. Mayer, and M.-A. Nicollet, *Backscattering Spectrometry*, ed. A. Press. 1978, Orlando.

51. H. Timmers, R.G. Elliman, G.R. Palmer, T.R. Ophel, and D.J. O'Connor, *The development of a facility for heavy-ion elastic recoil detection analysis at the Australian National University,* nuclear Instruments and Methods B, **136**, 611 (1998).

52. H. Timmers, R.G. Elliman, and T.R. Ophel, *New design features of gas ionization detectors used for elastic recoil detection,* Nuclear Instruments and Methods A, **447**, 536 (2000).

53. H. Timmers, T.D.M. Weijers, and R.G. Elliman, *Unique capabilities of heavy ion elastic recoil detection with gas ionization detectors,* Nuclear Instruments and Methods B, **190**, 393 (2002).

54. G.G. Stoney, *The Tension of Metallic Films Deposited by Electrolysis,* Proceedings of the Royal Society of London, **A82**, 172 (1909).

55. M.W. Grindel, *Testing Collimation Using Shearing Interferometry*. 2004, Ocean Optics: http://Oceanoptics.com/Products/Collimation.asp.

56. A. Aydinli, A. Serpengüzel, and D. Vardar, *Visible photoluminescence from low temperature deposited hydrogenated amorphous silicon nitride,* Solid State Communications, **98**, 273 (1996).

57. M. López, B. Garrido, C. Garcia, P. Pellegrino, and A. Perez-Rodriguez, *Elucidation of the surface passivation role on the photoluminescence yield of silicon nanocrystals embedded in* SiO_2*,* Applied Physics Letters, **80**, 1637 (2002).

58. S. Cheylan and R.G. Elliman, *Effect of hydrogen on the photoluminescence of Si nanocrystals embedded in a* SiO_2 *matrix,* Applied Physics Letters, **78**, 1225 (2001).

59. M. Molinari, H. Rinnert, and M. Vergnat, *Improvement of the photoluminescence properties in a-*SiN_x *films by introduction of hydrogen,* Applied Physics Letters, **79**, 2172 (2001).

60. G.C. Yu and S.K. Yen, *Hydrogen diffusion coefficient of silicon nitride thin films,* Applied Surface Science, **201**, 204 (2002).

61. B. Tuttle, *Energetics and diffusion of hydrogen in* SiO_2*.,* Physical Review B, **61**, 4417 (2000).

62. M. Molinari, H. Rinnert, and M. Vergnat, *Effects of the amorphous-crystalline transition on the luminescence of quantum confined silicon nanoclusters,* Europhysics Letters, **66**, 674 (2004).

63. L. Zhong and F. Shimura, *Dependence of lifetime on surface concentration of copper and iron in silicon wafers,* Applied Physics Letters, **61**, 1078 (1992).

64. S. Coffa, L. Calcagno, S. Campisano, G. Calleri, and G. Ferla, *Control of minority carrier lifetime by gold implementation in semiconductor devices,* Journal of the Electrochemical Society, **136**, 2073 (1989).

65. J.F. Ziegler, J.P. Biersack, and U. Littmark, *The Stopping and Range of Ions in Solids*. 1985, New York: Pergamon.

66. D. Pacifici, E.C. Moreira, G. Franzo, V. Martorino, F. Priolo, and F. Iacona, *Defect production and annealing in ion-irradiated Si nanocrystals,* Physical Review B, **65**, 144109 (2002).

67. D.J. Lockwood, Z.H. Lu, and J.-M. Baribeau, *Quantum Confined Luminescence in Si/SiO_2 Superlattices,* Physical Review Letters, **76**, 539 (1996).

68. T.M. Walsh, *Light Emission from Silicon Nanocrystals and Microcavities*. Honours Thesis. 2001: Australian National University.

69. M. McCann, K. Weber, and A. Blakers. *An early deposited LPCVD silicon nitride: allowing the possibility of novel cell designs*. in *3rd World Conference on Photovoltaic Energy Conversion*. 2003. Japan: IEEE.

70. M.G. Spooner, T.M. Walsh, and R. Elliman, *Effect of microcavity structures on the photoluminescence of silicon nanocrystals,* Materials Research Society Symposium Proceedings, **770**, 51 (2003).

71. R.D. Deegan, P.J. Petersan, M. Marder, and H.L. Swinney, *Oscillating Fracture Paths in Rubber,* Physical Review Letters, **88**, 014304-1 (2002).

72. A. Yuse and M. Sano, *Transition between crack patterns in quenched glass plates,* Nature, **362**, 329 (1993).

73. R.D. Deegan, S. Chheda, L. Patel, M. Marder, H.L. Swinney, J. Kim, and A. DeLozanne, *Wavy and rough cracks in silicon,* Physical Review E, **67**, 066209 (2003).

74. D.C. Meyer, T. Leisegang, A.A. Levin, P. Paufler, and A.A. Volinsky, *Tensile crack patterns in Mo/Si multilayers on Si substrates under high-temperature bending,* Applied Physics A, **78**, 303 (2004).

75. Z. Neda, K.-T. Leung, L. Jozsa, and M. Ravasz, *Spiral cracks in drying precipitates,* Physical Review Letters, **88**, 95502 (2002).

76. M.P. Hughey and R.F. Cook, *Irreversible stress development in PECVD silicon nitride films,* Materials Research Society Symposium Proceedings, **795**, u1.6.1 (2004).

77. L.A. Chow, Y.H. Xu, B. Dunn, and K.N. Tu, *Cracking behaviour of xerogel silica films on silicon substrates,* Applied Physics Letters, **73**, 2944 (1988).

78. J. Turley and G. Sines, *The anisotropy of Young's modulus, shear modulus and Poisson's ratio in cubic materials,* Journal of physics D: Applied physics, **4**, 264 (1970).

79. V. Kaajakari, *Silicon as an anisotropic mechanical material*: http://www.kaajakari.net/~ville/research/tutorials/elasticity_tutorial.pdf.

80. K.E. Puttick and M.M. Hosseini, *Fracture by a pointed indenter on near (111) silicon,* Journal of Physics D: Applied physics, **13**, 875 (1980).

81. T. Iizuka and Y. Okada, *Asymmetry in Indentation-Induced Mechanical Damage on Si (111) Surfaces,* Japanese Journal of Applied Physics, **33**, 1435 (1994).

82. M.P. Hughey and R.F. Cook, *Massive stress changes in plasma-enhanced chemical vapor deposited silicon nitride films on thermal cycling,* Thin Solid Films, **460**, 7 (2004).

83. D.A.P. Bulla and N.I. Morimoto, *Deposition of thick TEOS PECVD silicon oxide layers for integrated optical waveguide applications,* Thin Solid Films, **334**, 60 (1998).

84. S.M. Orbons, *Characterization of Silicon Nanocrystal Systems: The Effect of Material Structure on Nanocrystal Luminescence.* Honours Thesis. 2003: Flinders University.

85. K.O. Hill, Y. Fujii, D.C. Johnson, and B.S. Kawasaki, *Photosensitivity in optical fiber waveguides: Application to reflection filter fabrication,* Applied Physics Letters, **32**, 647 (1978).

86. G. Brambilla, V. Pruneri, L. Reekie, C. Contardi, D. Milanese, and M. Ferraris, *Bragg gratings in ternary SiO_2:SnO_2:Na_2O optical glass fibers,* Optics Letters, **25**, 1153 (2000).